UNIVERSITY OF GENEVA

Certificat Complémentaire en Géomatique

Mémoire de Recherche

Structural analysis of a highly oblique rift zone influenced by a transform fault in southwest Iceland

Supervisors

Giuliani Gregory

Ruch Joel

Author

Chatelain Yohann

May 2024

Abstract

The South-Iceland-Seismic Zone (SISZ) and the Reykjanes Peninsula are part of the plate boundary that separates the North American from the Eurasian plates. The Reykjanes Peninsula is a highly oblique rift zone with well-developed volcanic systems. To the East, the SISZ corresponds to a transform zone with historical large. These two regions are affected by a left-lateral shear oriented N070, accommodated by NS right lateral strike-slip faults forming a bookshelf system suggesting a common tectonic driver. The connection between the two regions remains poorly understood by lack of integrative structural analysis.

Here we used photogrammetry to analyse 20 NS fault systems, which all feature en-echelon structures and compressive push-ups, in both areas, along an E-W sector, to perform a fault population analysis and detailed structural maps. We further complemented our dataset with earthquake catalogues to look for ongoing seismic activity.

We estimate that these data's parameters suggest a structural continuity between the SISZ and the Peninsula, despite an observed continual decrease westward.

We further discuss that the presence of magma in Reykjanes is influenced by the rotation of the plate boundary, which 20° seems to be the minimum angle for its development.

Résumé

La Zone Sismique du Sud de l'Islande (SISZ) et la Péninsule de Reykjanes font partie de la limite qui sépare la plaque nord-américaine de la plaque eurasiatique. La Péninsule est une zone de rift fortement oblique avec des systèmes volcaniques bien développés. À l'est, SISZ correspond à une zone transformante avec des séismes historiques importants. Ces deux régions ont un cisaillement latéral sénestre orientée N070, qui est accommodé par des failles de décrochement dextre orientées NS, formant un système en "bookshelf" suggérant un moteur tectonique commun. La connexion entre ces deux régions reste mal comprise en raison du manque d'analyse structurale commune.

Dans cette étude photogrammétrique, nous avons analysé 20 systèmes de failles principalement orientés NS, qui présentent toutes des structures en-échelon et des push-ups compressifs, dans les deux régions, afin de procéder à une analyse de la population de failles et à la création de cartes structurales détaillées. Nous avons complété notre ensemble de données avec des catalogues sismiques pour y corréler l’activité sismique.

Nous avons observé que les paramètres de ces données suggèrent la présence d’une continuité structurelle entre SISZ et la Péninsule, malgré une diminution continue vers l'ouest. Nous discutons en outre que la présence de magma à Reykjanes est influencée par la rotation de la limite des plaques, où 20° semble être l’angle minimum pour son développement.

Contents

List of Figures

List of Appendixes

GIS mapping

MATLAB diagram

From Literature

Chapter 1

Introduction

Natural risks have been a constant companion to humanity throughout history. Among these risks, earthquakes stand out as one of the most devastating due to their destructive power, unpredictability, and wide potential occurrence. Although our understanding of these events has improved, enabling us to identify and mitigate high-risk areas, earthquakes remain highly lethal, manifesting through direct or indirect impacts.

The exponential growth of the global human population exacerbates potential risks, either through active colonization of known risk areas or by increasing population density in these vulnerable regions. Additionally, the primary mitigation methods, whether through infrastructure improvements or enhanced accessibility for rescue operations in disaster areas, prove to be prohibitively expensive and thus unattainable for numerous less well countries worldwide.

Earthquakes primarily occur in proximity to volcanic activity (Greenfield et al., 2020), or near the boundaries of tectonic plates, such as subduction zones, collision zones, and divergent plate boundaries like rifts or mid-ocean ridge systems (Figure 2.2). The

latter are particularly challenging to study due to their inaccessibility. One of the few locations where they are not situated at ocean's bottoms is in Iceland where the extensional setting spreads apart the North American from the Eurasian tectonic plates (Denk et al., 2011; Einarsson, 2008; Sigmundsson, 2006; Sigmundsson et al., 2020a). To the South-West part of this emerged extensional plate boundary lies Reykjavik, the capital and principal city of Iceland, housing around 135,000 inhabitants.

This study concentrates on the South-West part of Iceland and aims to contribute to better understand the causes and potential extent of highly destructive earthquakes in South Iceland (Einarsson et al., 1981; Karson et al., 2019).The challenges associated with studying mid-ocean ridges are largely rooted in their location. Apart from the Icelandic segment, these ridges are situated at significant ocean depths. According to Woodcock et al. in 1986a, more than 70% of the world's ridge systems exhibit obliqueness to the extension direction (A. E. Clifton & Kattenhorn, 2006a; Höskuldsson et al., 2007a; Woodcock et al., 1986b). Therefore, by investigating the distinct highly oblique spreading regions in South Iceland, this study aims to provide valuable insights into the mechanisms governing the formation and evolution of mid-oceanic ridges.

The research encompasses various scientific aspects, including structural field measurements and drone mapping, complemented by the integration of seismic data analysis. Fieldwork was carried out in the Southwestern part of Iceland, specifically in the Reykjanes Peninsula and the southern plain between the Hengill and Hekla volcanoes, named the South Icelandic Seismic Zone (SISZ; Sigmundsson et al., 2020a). This comprehensive approach seeks to enhance our understanding of mid-ocean ridges and oblique rift zones, shedding light on their intricate geological processes.

Chapter 2

Iceland geological setting

Iceland is located on the plate boundary between the Eurasian Plate to the south and east, and the North American Plate to the northwest (Sigmundsson, 2006; Sigmundsson et al., 2020a). This emerged plate boundary forms a segment of the North Atlantic mid-ocean ridge, positioned between the Reykjanes Ridge and the Kolbeinsey Ridge (Denk et al., 2011; Sigmundsson, 2006; Figure 2.4). The primary geological activity in Iceland is concentrated along this boundary (Sigmundsson et al., 2020a; Thordarson & Larsen, 2007).

The plate boundary in Iceland is typically classified into two distinct types, depending on the nature of the activity in each area. The first type, primarily associated with volcanic activity leading to the creation of new crust and faults, is termed a Volcanic Rift Zone. There are the North, the East, and the West Volcanic Zone and the Reykjanes Peninsula rift. The second type, characterized exclusively by seismic activity without magma production, is referred to as a Seismic Zone (Sigmundsson et

al., 2020a; Figure 2.3). The two main region of this type are South Iceland Seismic Zone and the Tjörnes Seismic Zone. In Iceland, except for the Reykjanes Peninsula rift, the elongations of the rift zones tend to align more parallel to the mid-ocean ridge, whereas the seismic zones exhibit a more perpendicular orientation to it.

Approximately thirty distinct volcanic systems are present along this boundary, also accompanied by significant seismic activity (Einarsson, 2008; Sigmundsson et al., 2020a; Thordarson & Larsen, 2007; Figure 2.1).

Typically, a volcanic system in Iceland consists of a central volcano accompanied by a network of fissures or dyke swarms (A. E. Clifton & Kattenhorn, 2006b; Rut Hjartardóttir et al., 2015; Sigmundsson et al., 2020a; Thordarson & Larsen, 2007; Figure 2.1). Many of these systems feature at least one caldera in their central region, with calderas sometimes reaching considerable sizes, spanning tens of kilometres. Additionally, it is common to find a complex of nested calderas resulting from various eruptive events within a single system (Sigmundsson et al., 2020a). In the peripheral regions of the volcanic system, dykes extend perpendicularly to the direction of minimal stress, which generally aligns along the plate boundary. These dyke intrusions appear to play a pivotal role in the extensional processes occurring along the Icelandic rift (Galindo & Gudmundsson, 2012; Greenfield et al., 2020; Sigmundsson et al., 2020a; Thordarson & Larsen, 2007).

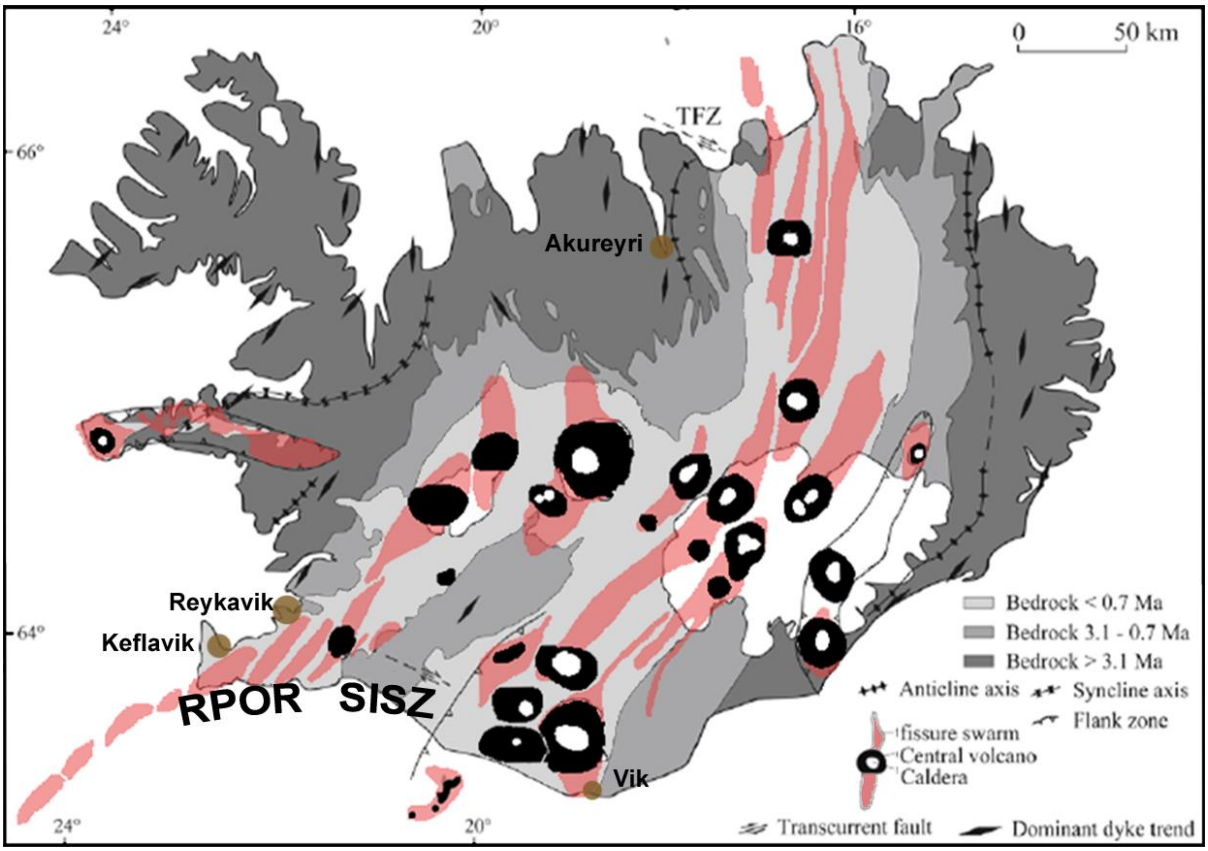

Figure 2.1: Iceland map of volcanic activity. The XX active volcanic systems are enhanced with their calderas and fissure swarms' extensions. Nearly these systems are located along the plates boundary, where there are the younger rocks, in light grey, due the spreading activity occurring at this plate boundary. Modified from Denk et al., 2011 and Thordarson & Larsen, 2007.

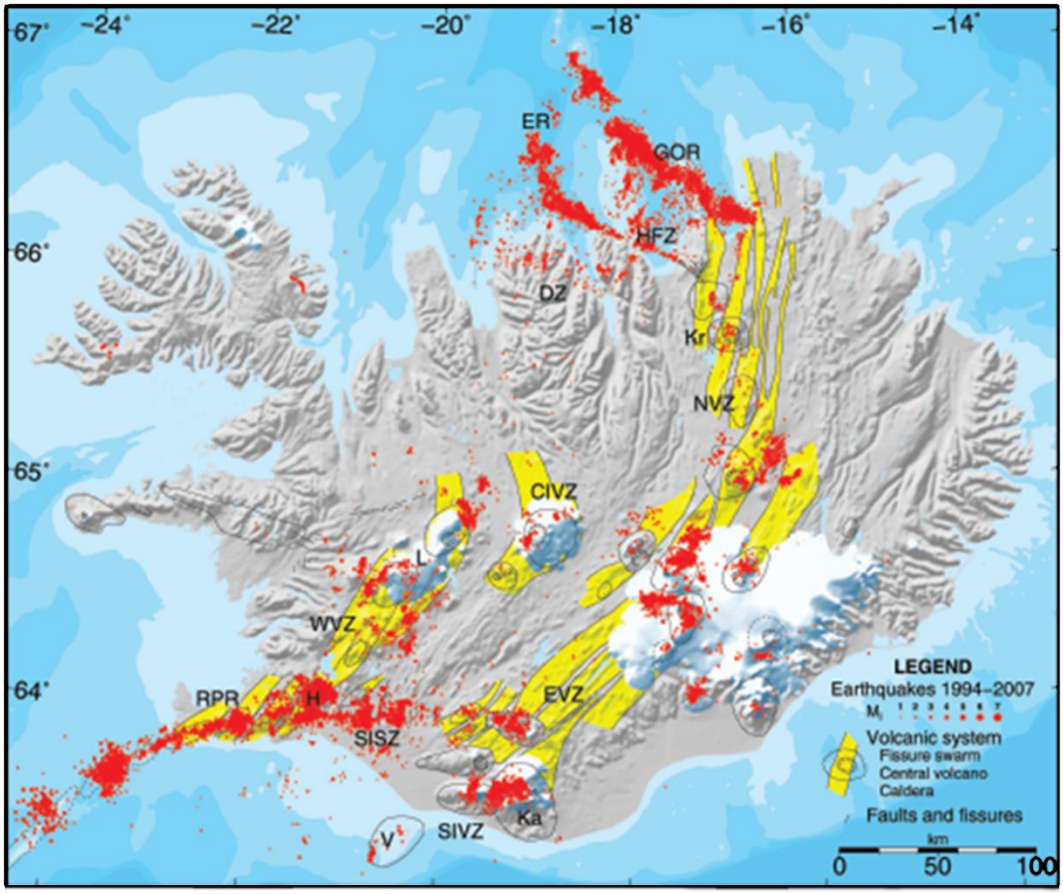

Figure 2.2: Iceland geological activity lookout. Map of the earthquakes' epicentres occurred in Iceland between 1994 and 2007. Nearly all this activity is located on the plate boundary area. The active volcanic systems' fissure swarms along these limits are also shown under the earthquake. From Einarsson, 2008.

The intense volcanic activity, induced by the central rifting in Iceland, has resulted in the predominant composition of nearly all the country's bedrock being basalt (Sigmundsson et al., 2020a). the overall composition of the Icelandic crust aligns with that of the oceanic crust (Flóvenz et al., 2015; Kaban et al., 2002). The basaltic landscape exhibits distinguishable features, with recent subaerial events yielding basalt differing from subglacial events during the last glaciation, evident through hyaloclastite tuffs (Denk et al., 2011; Sigmundsson et al., 2020a).

The ages of the rocks vary, with recent formations near the rift and get progressively older as one move away from the rift. In the eastern and northwestern parts of Iceland,

rock ages can extend up to approximately 15 Ma (Denk et al., 2011; Sigmundsson et al., 2020a; Thordarson & Larsen, 2007; Figure 2.3).

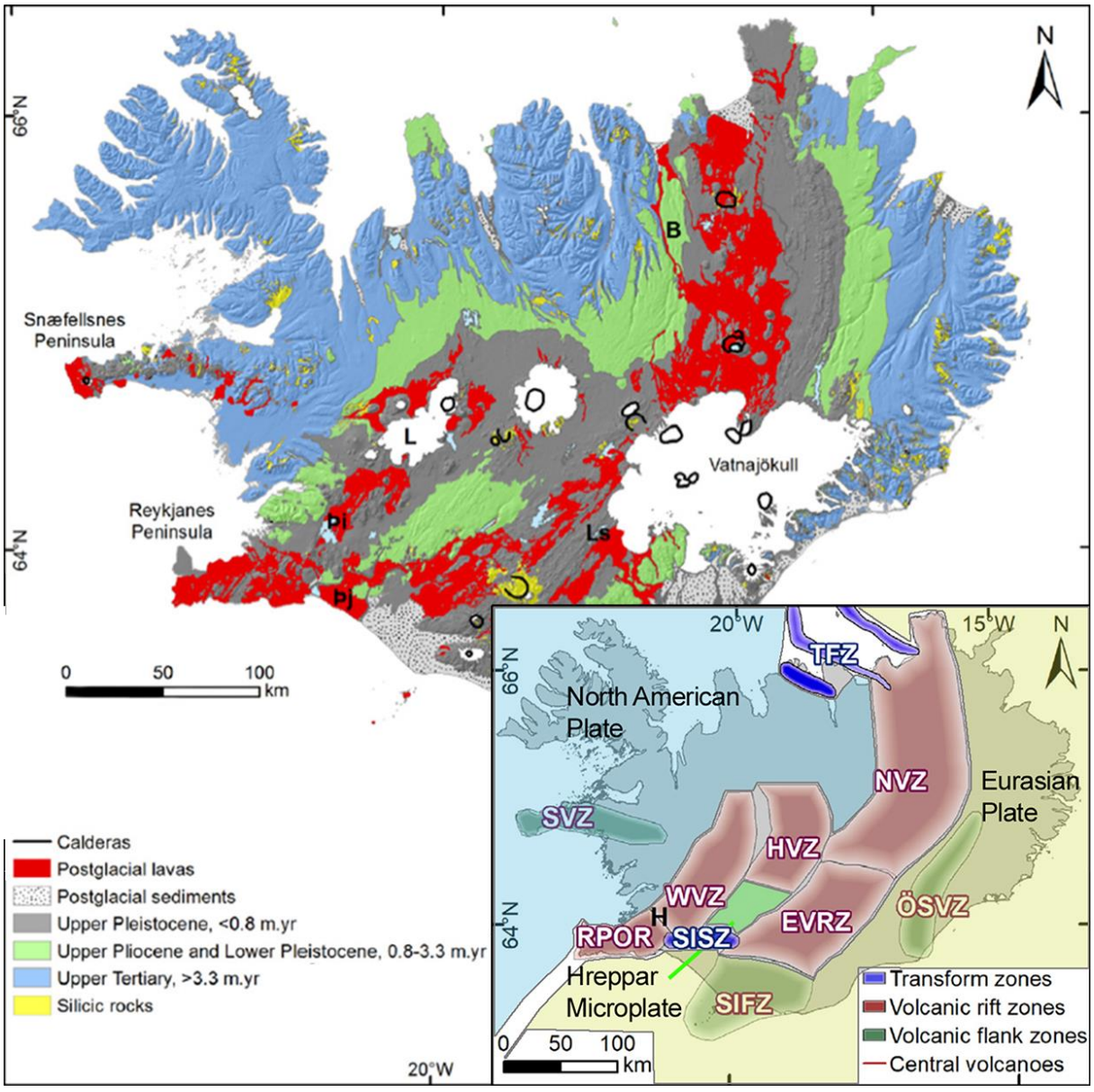

Figure 2.3: A: Simplified geological map. The basaltic rocks are differenced by their age, where the youngers are in central Iceland along the active spreading zone and the older are located at the east and west shore. From YY. **B:** Volcanic and Transform zone map in Iceland. The plate boundary is composed of either volcanic rift zones, with crust creation, and transform zone. In south Iceland, there is Hreppar microplate between the North American plate in the west and the Eurasian plate in the east. Modified from Sigmundsson et al., 2020a.

Like other mid-oceanic ridges, the primary induced stress behind the Iceland plate boundary is extensional (Geirsson, 2003; LaFemina et al., 2005; Sigmundsson, 2006; Sigmundsson et al., 2020a). The average spreading rate between the North American and Eurasian plates is approximately 18.6 millimetres per year, occurring in a direction roughly around N104° according to NUVEL_1A (Geirsson, 2003; LaFemina et al., 2005; Sigmundsson et al., 2020a). However, it's noteworthy that the spreading axis of the plate is not consistently perpendicular to the local strike of the rift (Einarsson, 2008; LaFemina et al., 2005; Sigmundsson et al., 2020a; Woodcock et al., 1986a). This introduces a shear component alongside the primary extensional force. In the most oblique rifting areas relative to the spreading axis in Iceland (e.g., Reykjanes Peninsula, SISZ, Tjörnes …), the shear component could be at least as significant as the extensional force (A. E. Clifton & Kattenhorn, 2006b; Einarsson, 2008; Sigmundsson et al., 2020a).

While the mid-ocean ridge spanning Iceland is a significant contributor to the country's volcanic activity, it is not the sole source. There is an additional mantle upwelling beneath the lithosphere (Allen et al., 2002; Denk et al., 2011; Kaban et al., 2002; Sigmundsson et al., 2020a; Thordarson & Larsen, 2007). The current centre of this plume is estimated to be beneath the Vatnajökull, near the central volcano Grímsvötn (Allen et al., 2002; Kaban et al., 2002; Thordarson & Larsen, 2007). The evidences of this upwelling extends westward, along the Greenland coast (Denk et al., 2011; Thordarson & Larsen, 2007; Figure 2.4). The initial signs of volcanic activity in this region date back approximately 70 Ma, and these lava fields are correlated with the North Atlantic Igneous Province (Denk et al., 2011).

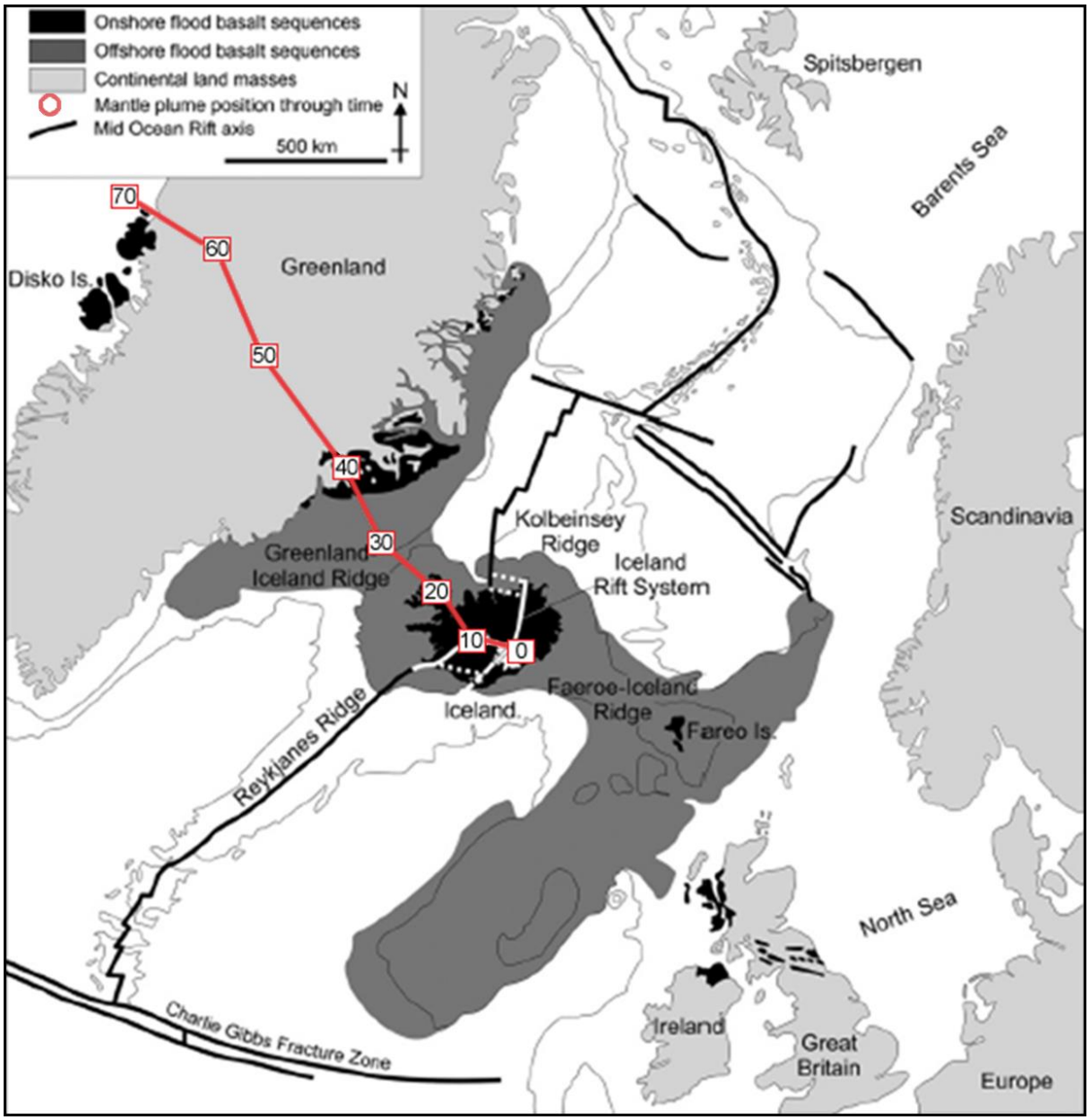

Figure 2.4: Plume location map. Evolution of the location of the mantle plume in million years (Ma), with its related basalt floods that build the Faeroe-Greenland bridge. The complex interaction of the plume with the North Atlantic ridge is also visible. Modified from Thordarson & Larsen, 2007.

The geological history of Iceland is intricately linked to the interaction between the volcanic hotspot and the North Atlantic mid-ocean ridge (Sigmundsson et al., 2020a; Thordarson & Larsen, 2007). The presence of the hotspot significantly influences the overall plate boundary, exerting a force that pulls it toward the East (Einarsson, 2008; LaFemina et al., 2005; Sigmundsson et al., 2020a; Thordarson & Larsen, 2007). This dynamic creates multiple rifts jumps in the eastward direction, resulting in the

separation of a portion of the Eurasian continent that becomes attached to the North American plate (Hardarson et al., 1997; LaFemina et al., 2005; Sigmundsson et al., 2020a). It also accommodates the extension through oblique rifts (A. E. Clifton & Kattenhorn, 2006b; Einarsson, 2008). In west Iceland, there are some old, currently inactive rifts, serving as markers of these historical rift jumps (Hardarson et al., 1997; Figure 2.5).

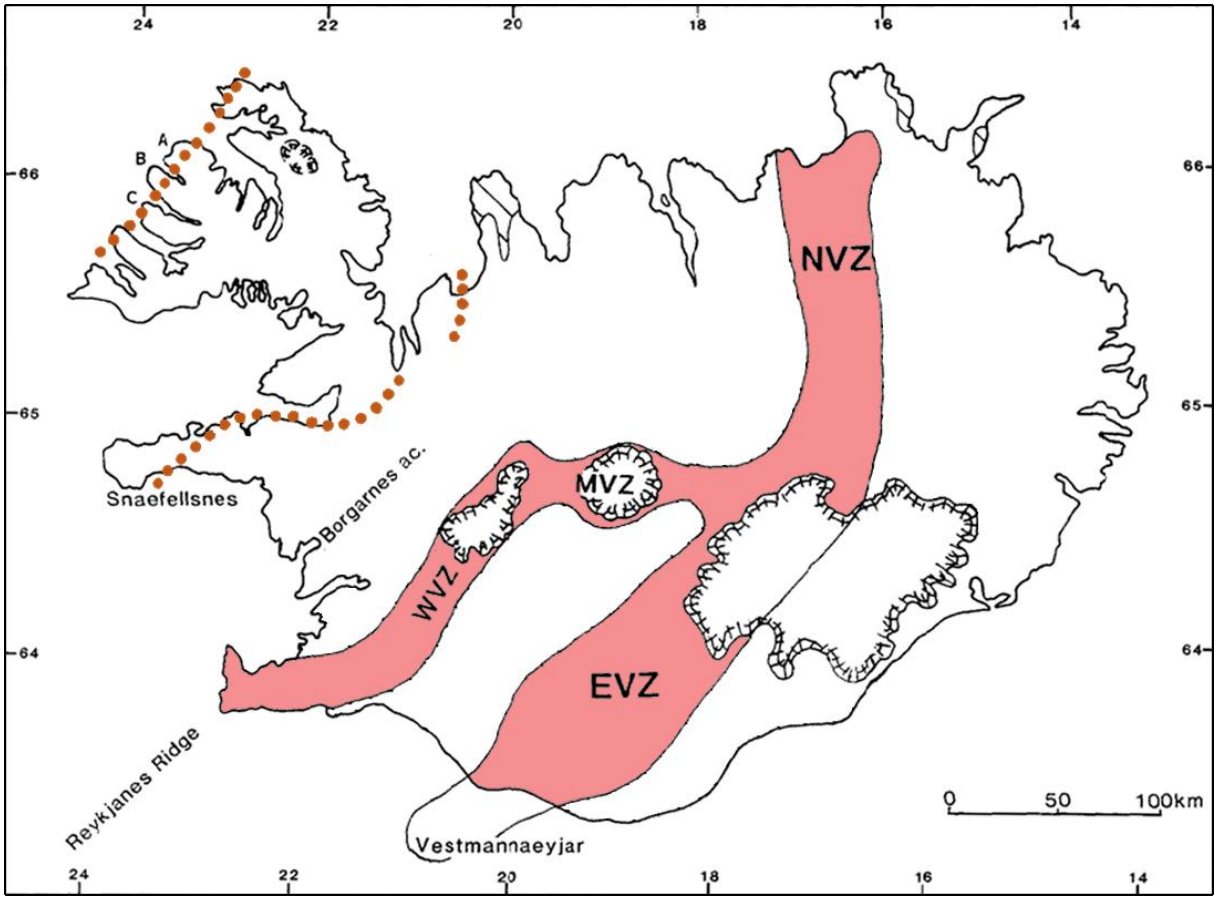

Figure 2.5: Old and Recent rifting activity map in Iceland. The actual active rift is approximately shown as the red surface and the ancient dead rift are the red dotted line. Modified form Hardarson et al., 1997.

The primary explanation for the lithosphere thickness anomaly in Iceland lies in this interaction between the plume and the ridge (Denk et al., 2011; Thordarson & Larsen, 2007). In typical oceanic crust, which is generally around 7 kilometres deep, the Moho depth in Iceland can extend up to 40 kilometres (Allen et al., 2002; Kaban et al., 2002). The minimum depth is slightly greater than 15 kilometres near the onshore rift and

oceanic ridge boundary (Kaban et al., 2002). The Iceland Plateau, an extensive area with a topographic height in the Atlantic covering 350,000 square kilometres, exhibits an average elevation of approximately 3,000 meters compared to the surrounding abyssal plain (Thordarson & Larsen, 2007).

The Iceland Plateau is not an isolated feature, rather, it constitutes the central and most prominent part of the Faeroe-Greenland bridge spanning the North Atlantic (Denk et al., 2011; Kaban et al., 2002; Sigmundsson et al., 2020a; Thordarson & Larsen, 2007). This bathymetric positive anomaly on the oceanic crust serves as a connection point, linking the spreading lava field of the North Atlantic Igneous Province present in Greenland and the Great Britain islands (Denk et al., 2011). The correlation between the Iceland Plateau and the plume activity becomes apparent in this geographical context.

Chapter 3

Project background

3.1 Southwest Iceland

The plate boundary traversing Iceland passes through the southwest region, connecting the Reykjanes Ridge to the East and North Volcanic Zones (EVZ) in the Icelandic highlands. The complexity of rifting in this area arises from the presence of three distinct zones: the Reykjanes Peninsula Oblique Rift (RPOR), the Western Volcanic Zone (WVZ), and the South Iceland Seismic Zone (SISZ) (Sigmundsson et al., 2020b; Figure 2.3). The RPOR is located on the Reykjanes Peninsula, serving as the on-land extension of the Reykjanes Ridge (Weir et al., 2001). Positioned north of the RPOR, the WVZ operates as a purely extensional rift, while the SISZ acts as a shear zone to the east of these two (Einarsson, 2008; Sigmundsson et al., 2020b). All three zones converge at the triple point of Hengill volcano (Einarsson, 2008; Sigmundsson et al., 2020b). The SISZ plays a crucial role in linking the RPOR with the EVZ, thereby extending the plate border northward (Einarsson, 2008; Geirsson, 2003; LaFemina et al., 2005; Sigmundsson et al., 2020b).

The presence of the WVZ to the north of the RPOR, outside the more active plate border in South Iceland, introduces additional complexity to this rifting zone. The WVZ runs parallel to the EVZ, forming a dual rift system that accommodates the total spreading (LaFemina et al., 2005; Sigmundsson et al., 2020b). The Hreppar microplate acts as a distinct block between these two rifts, with well-defined boundaries (LaFemina et al., 2005; Luxey et al., 1997; Figure 3.1). Bounded by the WVZ and EVZ to the west and east, respectively, and by the SISZ to the south and Hofsjoküll to the north, the Hreppar microplate plays a crucial role in the overall dynamics.

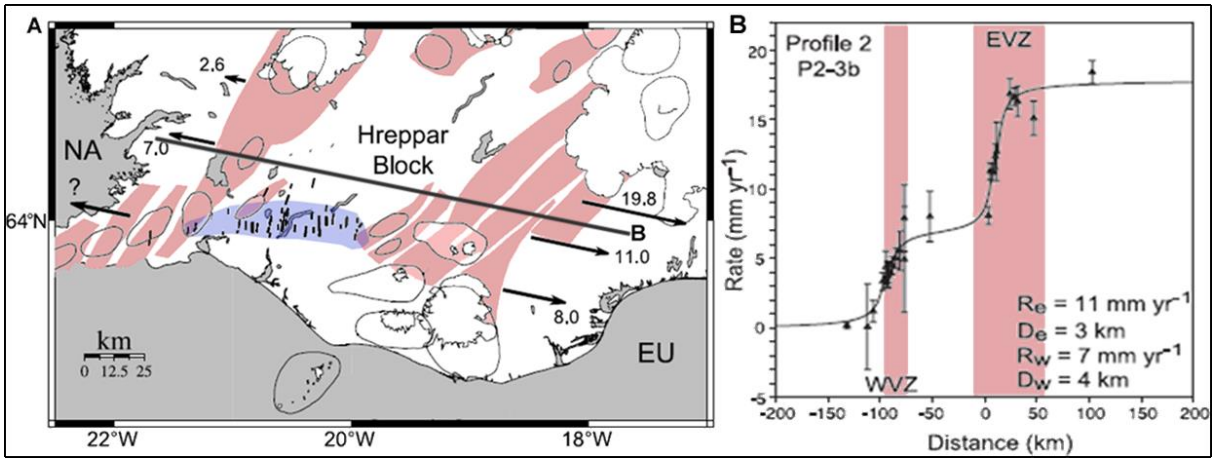

Figure 3.1: Parallel rift and Hreppar Microplate. **A:** Map of the spreading of the North American and Eurasian plates in function of the Hreppar microplate, with in red the active fissure swarms of the rifting zones and in blue a transform zone that delimitate the plates. **B:** Extension rate plot (along B line in **A**) from the North American Plate. The spreading is distributed in the two parallel rifts separate by the uniform Hreppar block. Modified from LaFemina et al., 2005.

While the western rift currently exhibits minimal activity, accounting for at most one-third of the total spreading in South Iceland, the southern part of the WVZ, extending from the RPOR, experiences the maximum spreading of around 8 millimetres (Einarsson, 2008; LaFemina et al., 2005; Figure 3.1). This spreading gradually decreases towards the north, reaching 0 millimetre at the end of the WVZ (LaFemina et al., 2005). The EVZ displays a similar spreading decrease, but in the southern direction (LaFemina et al., 2005; Sigmundsson et al., 2020b). Consequently, the

Hreppar microplate undergoes anticlockwise rotation to accommodate these shearing forces (LaFemina et al., 2005).

A few thousand years ago, the WVZ was considerably more active than its younger eastern counterpart, which is only 2 million years old (Einarsson, 2008; LaFemina et al., 2005). This shift in activity suggests an ongoing rift jump from the WVZ to the EVZ (Einarsson, 2008; Hardarson et al., 1997; LaFemina et al., 2005; Sigmundsson et al., 2020b). As a result, the Hreppar microplate could be considered an ancient segment of the Eurasian plate, poised to be attached to the North American plate in the future (Sigmundsson et al., 2020b).

The rift in South Iceland is highly oblique to the spreading direction, particularly in the RPOR and SISZ (Árnadóttir et al., 2006; Einarsson, 2008). The obliquity in the RPOR is believed to accommodate an older rift jump to the WVZ by establishing a connection with the Reykjanes Ridge. This jump is estimated to have occurred around 7 million years ago, coinciding with the commencement of volcanic activity in that region (Sigmundsson et al., 2020b). In a similar context, the SISZ plays a crucial role in accommodating the most recent rift jump between the RPOR and the EVZ (Bergerat & Angelier, 2008).

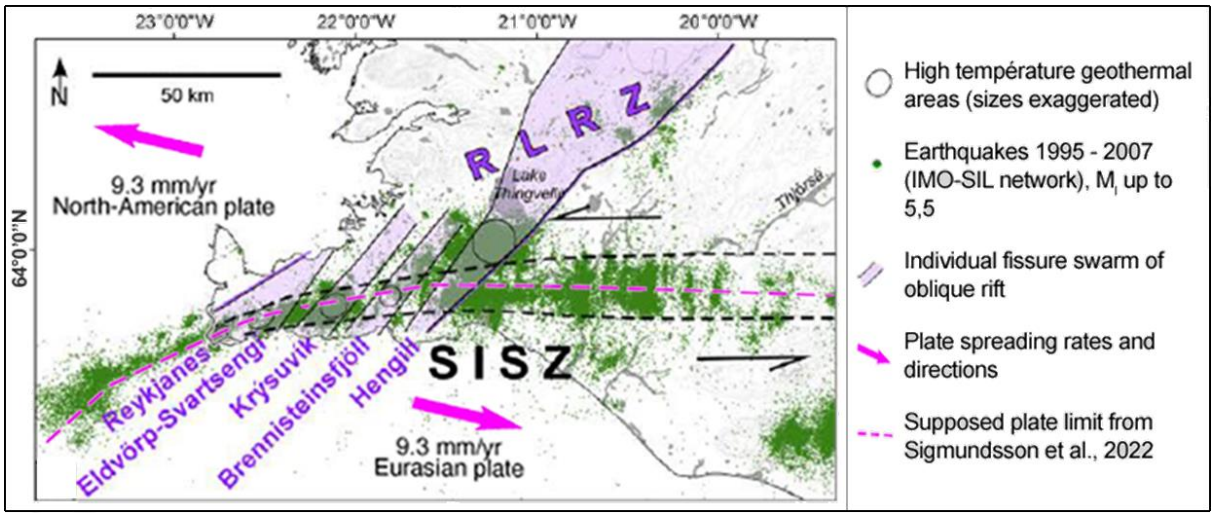

Figure 3.2: Southwest oblique plate boundary. The main plate boundary in southwest Iceland is highly oblique to the plates' spreading direction, which creates a few kilometres width zone of shearing around the boundary. Like in all Iceland, the Earthquakes are concentrated inside this boundary zone. There are volcanic systems and high temperature geothermal areas in Reykjanes Peninsula only. Modified from Khodayar et al., 2018 and Sigmundsson et al., 2022.

To investigate the intricate plate spreading characterized by high obliquity and a dual rift system, numerous GPS studies have been conducted since the 1990s in the region, with a specific focus around the SISZ. These studies have provided clear insights into the sinister shear component and the uniform movement of the Hreppar microplate (Árnadóttir et al., 2006; Geirsson, 2003; LaFemina et al., 2005; Figure 3.2).

This study will specifically focus into the highly oblique plate boundary systems of RPOR and SISZ (Figure 3.2). While various studies have explored the Reykjanes Peninsula, focusing predominantly on structural and fault analyses for hydrothermal industries, these investigations have revealed the presence of distinct fault families that intersect (A. E. Clifton & Kattenhorn, 2006b). However, the scientific understanding of the SISZ area remains limited in comparison, despite being a significant source of high-magnitude earthquakes in the South-West (Einarsson et al., 1981; Kowsari et al., 2020). This relative scarcity of information is largely attributed to the loose soil in the region, which quickly erases traces of tectonic activity within a few decades of fieldwork. The region's low geothermal gradient has likely contributed to its relative neglect in scientific research.

3.2 The South Iceland Seismic Zone (SISZ)

The SISZ is situated in the arable plain around Selfoss in South Iceland, extending as the continuity of the plate boundary after the Hengill volcano. It reaches until the EVZ, near the southern glaciers of Myrdalsjökull and Vatnajökull (Bjarnason & Einarsson, 1991; Einarsson et al., 1981). Despite being the structural continuation of the Reykjanes Peninsula's rift, the SISZ is classified as a Seismic Zone without any volcanic activity (Sigmundsson et al., 2020b).

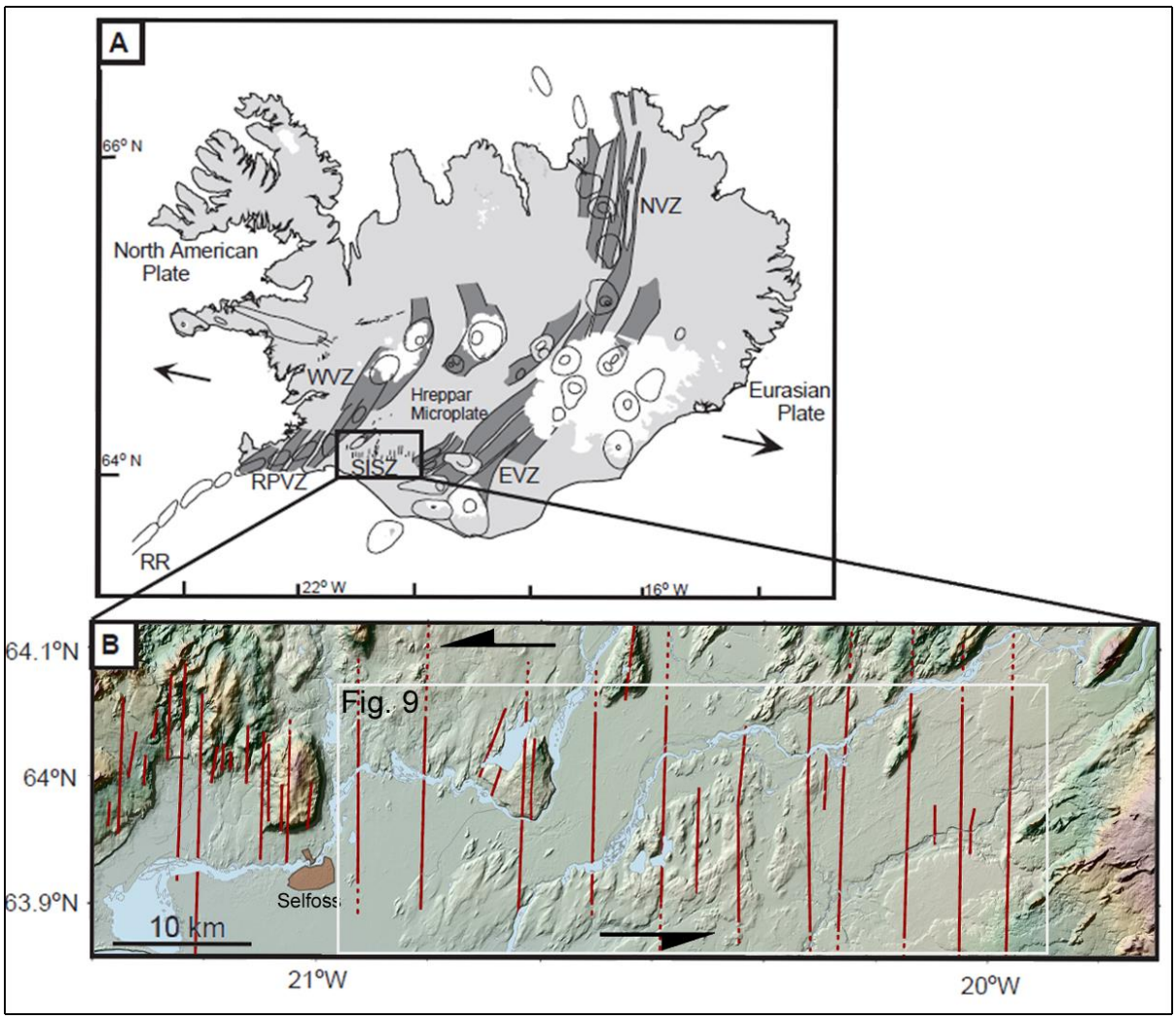

Figure 3.3: Main faults in South Iceland Seismic Zone. The faults, in red, are nearly all north south oriented. They are dextral strike-slip that accommodate the regional left shear. Full line corresponds to faults in the inter-seismic observed activity zone and dotted line corresponds to total fault extension from literature. **A** modified from Clifton & Einarsson, 2005.

Its extension is nearly parallel to the ridge spreading direction, exhibiting a clear east-west elongation of approximately 80 kilometres (Bergerat & Angelier, 2008). The sinister shear stress, estimated at approximately 15 millimetres per year (LaFemina et al., 2005), is accommodated in the SISZ by a series of north-south-oriented faults (Angelier et al., 2008; Einarsson, 2008; Einarsson et al., 1981; Sigmundsson et al., 2020b; Figure 3.3). These structures are present along the entire area, from Hengill to the EVZ, with an average lateral spacing under 4 kilometres (Einarsson, 2010; Karson et al., 2019). The faults themselves are a few kilometres long, ranging between 10 and 25 kilometres, and thus, they traverse the entire width of the SISZ (Bergerat & Angelier, 2008; Einarsson et al., 1981; Sigmundsson et al., 2020b).

The SISZ has a history of hosting destructive earthquakes, with recorded magnitudes reaching up to 7.5 (Einarsson et al., 1981; Karson et al., 2019; Kowsari et al., 2020). Notably, the last significant seismic activity occurred at the beginning of this century (in 2000 and 2008; Bergerat & Angelier, 2003, 2003; Decriem et al., 2010; Decriem & Árnadóttir, 2012) after a quiescent period of a little less than a century. Typically, high-magnitude earthquakes in this area manifest as a sequence of two to five earthquakes within a period ranging from a few seconds to a few years (Einarsson et al., 1981; Karson et al., 2019; Sigmundsson et al., 2020b). In general, the initial event of a seismic sequence occurs in the eastern part of the SISZ, with subsequent events progressing westward (Einarsson et al., 1981). Since the colonization of this area began during the 12th century, historical records indicate an average return time of 45 years for a seismic sequence (Einarsson et al., 1981; Figure 3.9). It's important to note that this mean is calculated with a significant gap in the historical record during the 15th century, potentially leading to an underestimation (Einarsson et al., 1981).

The family of N-S structures in the SISZ was identified and defined relatively late in the research timeline (Bjarnason et al., 1993; Bjarnason & Einarsson, 1991; Einarsson et al., 1981). These N-S faults are predominantly characterized as right-lateral strike-slip faults (Bergerat et al., 2003; Bergerat & Angelier, 2008; Bjarnason & Einarsson, 1991). The delayed categorization of these faults is attributed to their intricate multi-scale en-echelon structures. Specifically, they consist of varying degrees of en-echelon structures, including Fault, Array, and Segment (Bergerat et al., 2003), with metric push-ups occurring between the echelons (Bergerat et al., 2003; Einarsson, 2008). Subsequently, it has been observed that all major seismic events in the history of the SISZ can be linked to the slip of one of these N-S faults (Einarsson et al., 1981; Karson et al., 2019). These faults play a crucial role in accommodating shear stress through a mechanism known as bookshelf faulting (Angelier et al., 2008; Bjarnason et al., 1993; Einarsson, 2008; Karson et al., 2019; Sigmundsson et al., 2020b; Figure 3.4).

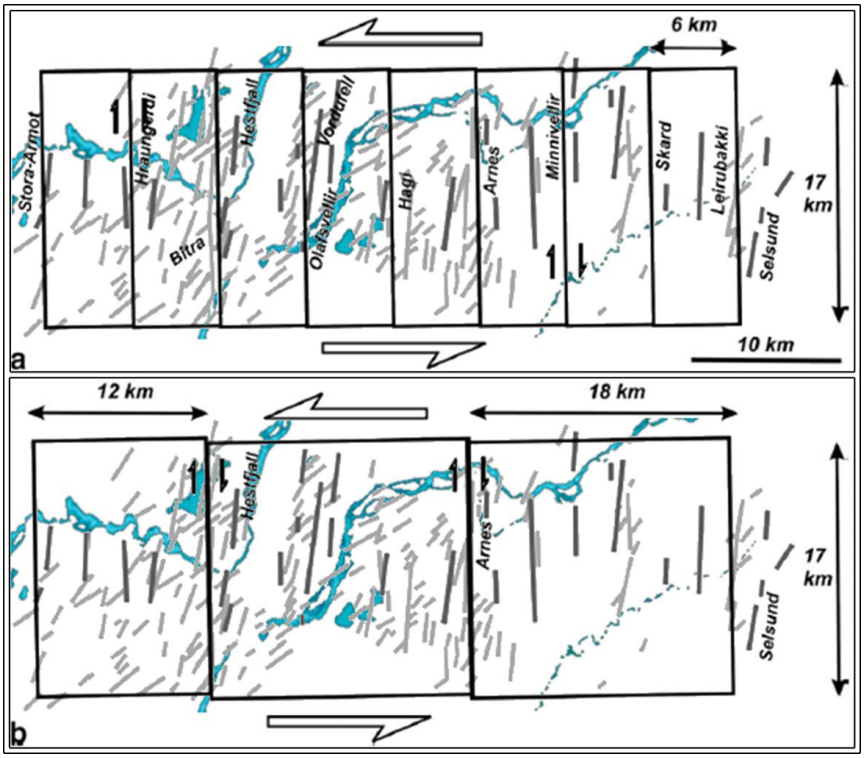

Figure 3.4: Bookshelf model in SISZ. The light grey faults are obtained by earthquakes' alignment and dark grey faults are the major faults by Johanesson and Saemundsson, 1998. These faults define structural blocks of approximately 6 kilometres wide behaving as a bookshelf model. **B:** Only 2000 events activation faults. Modified from Angelier et al., 2008.

Bookshelf faulting is characterized by an array of sub-parallel strike-slip faults that accommodate shear stress perpendicular to them (Einarsson, 2008). The crust blocks positioned between these faults undergo rotation, akin to a series of books slipping down a shelf, to follow the shearing force (Einarsson, 2008; Figure 3.4 and 3.5 D). This structural type bears resemblance to the Riedel Prime (R'), first described by Cloos in 1928 in the context of a strike-slip clay model (Dooley & Schreurs, 2012; Tchalenko, 1970). The R' structures are nearly perpendicular to the primary shear direction and are associated with Riedel (R) structures, which align more parallel to the shear (Ahlgren, 2001; Dooley & Schreurs, 2012; Tchalenko, 1970; Figure 3.5 A and B).

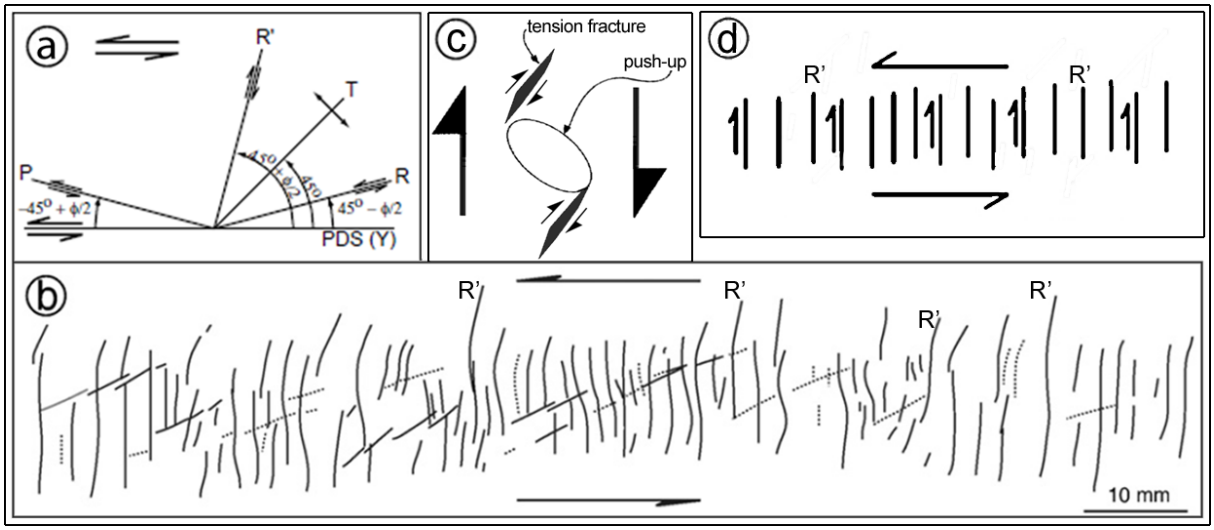

Figure 3.5: Structures models. **A:** Riedel and Riedel Prime structures geometry in function of the shear zone, with Φ as the internal friction of the host rock angle. From Ahlgren, 2001. **B:** Riedel experiment in clay model (kaolin) with water content around 50 percent. The sigmoidal shape is induced by blocks' rotation. From Dooley & Schreurs, 2012. **C:** Push-up and fractures interaction in a en-echelon strike-slip structure showing their optimal orientation. Modified from Bjarnason et al., 1993. **D:** Bookshelf faults organisation model in SISZ. From (Karson et al., 2019).

Analogous clay models of strike-slip faults have shown that the initial major structures developed are the R' structures, slightly preceding the development of the R faults (Ahlgren, 2001; Tchalenko, 1970). In the SISZ, the predominant and active structures are the R' structures, with a limited presence of R structures (A. Clifton & Einarsson, 2005; Einarsson, 2008, 2010). This similarity between the SISZ and the initial stage of

fault development in a clay model, known to be a reliable proxy for basalt in analogue models, suggests the juvenile character of the shear in the region.

3.3 The Reykjanes Peninsula Oblique Rift (RPOR)

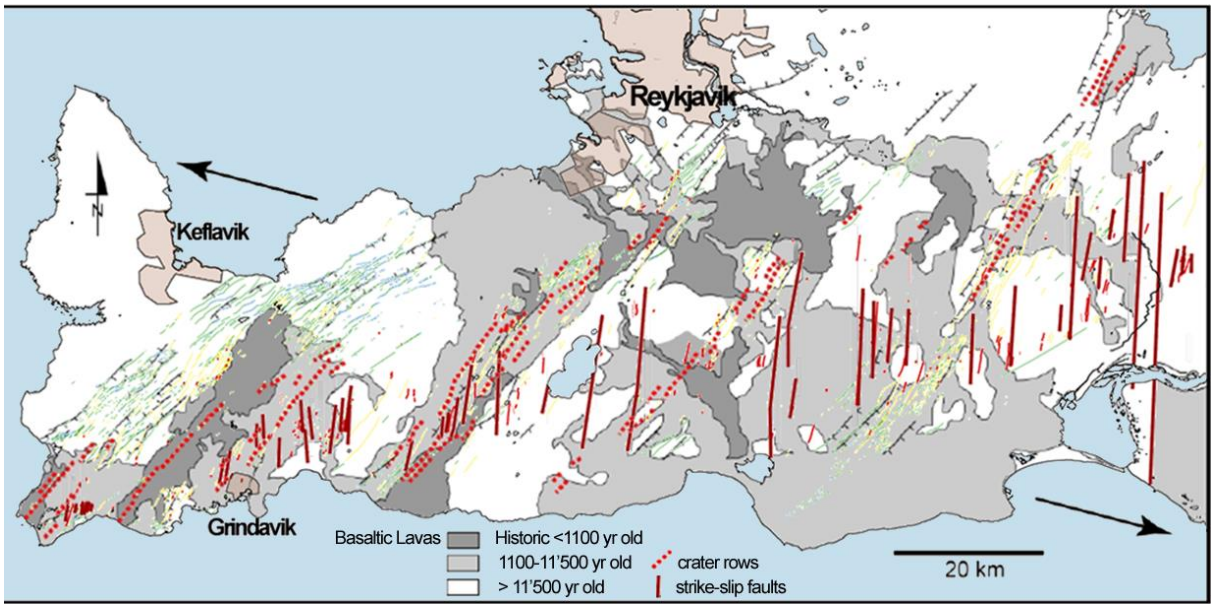

Figure 3.6: Simplified Reykjanes Peninsula geological and structural map. There is an intense activity of crust creation in recent time in RPOR, with large area covered by recent lava field and the presence of many craters' rows in the peninsula. The fissure swarms extent beyond the main rifting area to the North and to the South by following kilometric sigmoidal shape. The NS strike-slip faults are still present in RPOR, and they are centred on the estimated plate boundary area. Modified from A. E. Clifton & Kattenhorn, 2006; Karson et al., 2019.

The Reykjanes Peninsula is renowned for its magmatism, comprising five distinct volcanic systems from west to east: Reykjanes, Svartsengi-Fagradalsfjall, Krýsuvik, Brennisteinsfjöll, and Hengill, each associated with their fissure swarm, exhibiting a kilometric sigmoid trend (Caracciolo et al., 2023; A. E. Clifton & Kattenhorn, 2006b; Sigmundsson et al., 2020b; Figure 3.8). The most recent volcanic activity was observed approximately 800 years ago (Caracciolo et al., 2023; A. E. Clifton & Kattenhorn, 2006b; Figure 3.6) until the Fagradalsfjall eruption in March 2021 (Barsotti et al., 2023; Pedersen et al., 2022; Figure 3.7). This magmatism is a result of the extensional activity in the region dating back to 6-7 million years, linked to the presence

of the mid-ocean ridge in this area (A. E. Clifton & Kattenhorn, 2006b; Sigmundsson et al., 2020b). The magmatic activity in the peninsula is linked to crustal accretion process occurring within an extensional rift (Sigmundsson et al., 2020b). However, the extension context is notably highly oblique (A. E. Clifton & Kattenhorn, 2006b; A. Clifton & Schlische, 2003). The peninsula rift stands out as the most oblique area in Iceland concerning the extension direction(Sigmundsson et al., 2020b), aligning it with a leaky transform fault system until the Hengill volcano area. Despite this high obliquity, the peninsula rift effectively accommodates all the plate spreading (Sigmundsson et al., 2020b).

The Hengill complex is positioned between the two study areas, serving as the boundary between the Oblique Rift and the Seismic Zone and forming a triple junction with the third arm oriented northward, leading to the WVZ where the Thingvellir rift is located (Grigoli et al., 2022; Sigmundsson et al., 2020b).

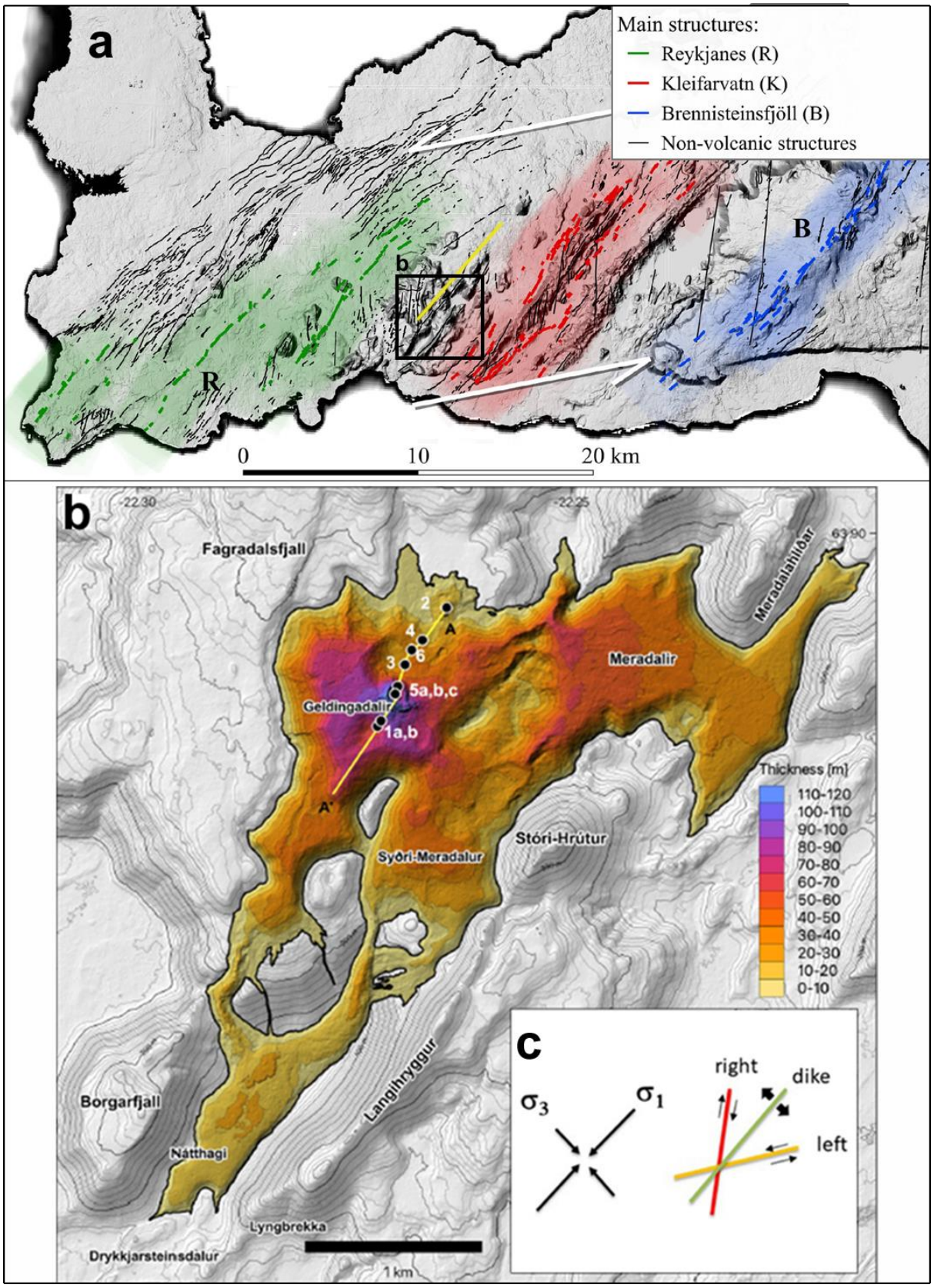

Figure 3.7: 2021 Fagradalsfjall event. **A:** Location and extension of the dike intrusion, in yellow, between the Reykjanes (Svartsengi) volcanic system and the Kleifarvatn one. From Bufféral et al., 2023. **B:** Lava field produced by this event with the location of the different vent of the eruptive fissure. From Pedersen et al., 2022. **C:** Horizontal stress and main related structures with the NS strike-slip faults in red, the dike extension in green and the plate boundary shearing in yellow. From (Einarsson et al., 2023).

Recently, like the main geological structures in the SISZ, N-S strike-slip faults, corresponding to a series of en-echelon structures, have been observed in Reykjanes as well (Bufféral et al., 2023; A. E. Clifton et al., 2003; A. E. Clifton & Kattenhorn, 2006b; Einarsson et al., 2020; Figure 3.8). Despite the rockier soil in the peninsula, which tends to showcase more chaotic faults, these faults belong to the same N-S fault family as their SISZ counterparts, where earthquakes occur (Einarsson et al., 1981; Karson et al., 2019). However, it is noteworthy that on one side of the Hengill complex, these faults exhibit low seismic activity and correlate with magma intrusion (Sigmundsson et al., 2020b). On the other side, within the SISZ, these faults are highly seismic even in the absence of magma (Einarsson et al., 1981, 2020).

Since the discovery of the N-S faults, their presence has been noted across the entire Reykjanes Peninsula, extending to its extreme western end (A. E. Clifton & Kattenhorn, 2006b; Einarsson et al., 2020). The two most recent high-magnitude earthquakes in the SISZ were also attributed to these NS faults (A. E. Clifton et al., 2003; Decriem et al., 2010; Decriem & Árnadóttir, 2012), as the reactivation of volcanic activity in the Peninsula during the years 2020/2021 (Bufféral et al., 2023; Einarsson et al., 2023; Hjartardóttir et al., 2023). Additionally, these structures have recently been observed in the Hengill region, which typically serves as the border between the SISZ and the Reykjanes Peninsula, suggesting a potential continuity between the two areas (Steigerwald et al., 2018; Figure 3.9).

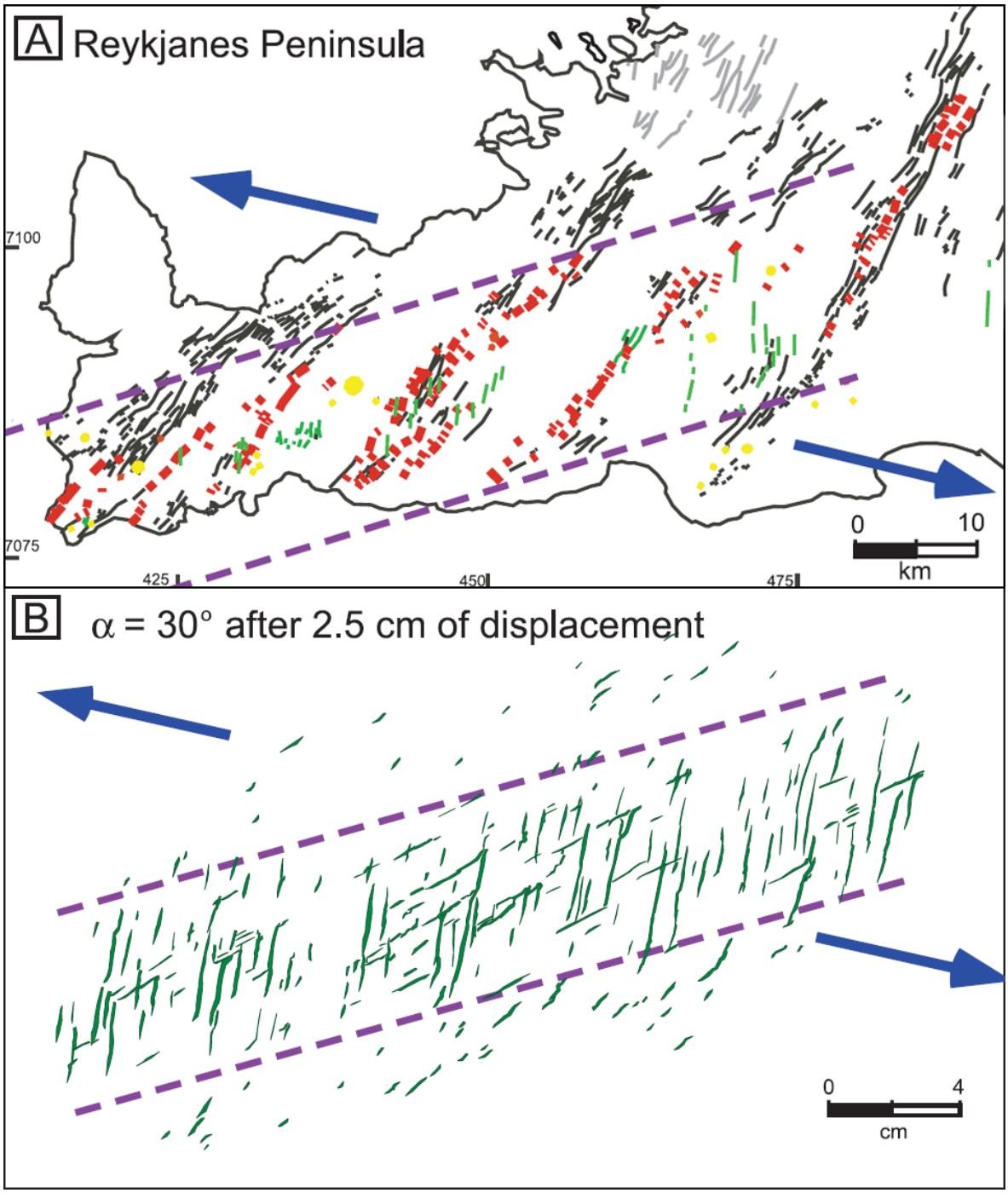

Figure 3.8: Highly oblique rift modelization. Comparison of tectonic map **(A)** RPOR with the volcanic zone between the purple dashed line, which correspond to the plates limit's area, with a wet clay analogue model's faults map **(B)** with a latex sheet to represent the plate's limit area. In **A**, the NS faults are green and the eruptive fissures in red. From (A. Clifton & Schlische, 2003).

3.4 Aims of the project

The principal goal of this study is to comprehend the interactions between tectonic and magmatic processes within an extreme oblique rift zone in Southern Iceland. The focus was to identifying common structural features between the Reykjanes Peninsula and the SISZ, particularly the N-S faults capable of generating earthquakes of up to M7.5 along the same plate boundary. Unlike the peninsula, the SISZ lacks magmatic contributions to plate spreading. Therefore, investigating both areas aims to enhance our understanding of the roles played by tectonics and magmatism in shaping oblique divergent plate boundaries. To achieve this goal, the study will concentrate on two primary scientific points:

- 1. Understanding the structural link between the deep plate boundary in the extensive ridge context and the N-S surface faults system.
- 2. Investigating the influence of tectonics and magmatism in the evolution and construction of highly oblique rifts and their potential transition into a leaky transform zone or a transform zone.

To achieve these goals, the main objectives are as follows:

- Mapping N-S faults in the Reykjanes Peninsula and the SISZ, establishing correlations with seismic data, and creating a comprehensive synthesis map extending from Reykjanes to Hekla.
- Define and categorize the en-echelon system of these faults.
- Perform a spatial analysis (East to West) of the N-S faults in the SISZ and the Reykjanes Peninsula, treating them as a continuum. Compare their characteristics, including depth, echelon strike, and length.
- Assess the relationship between the N-S faults and the regional stress developed by the extensional ridge context in these areas.
- Understand how these N-S faults interact with other structures in the Reykjanes Peninsula and explore their correlation with magma crustal propagation.

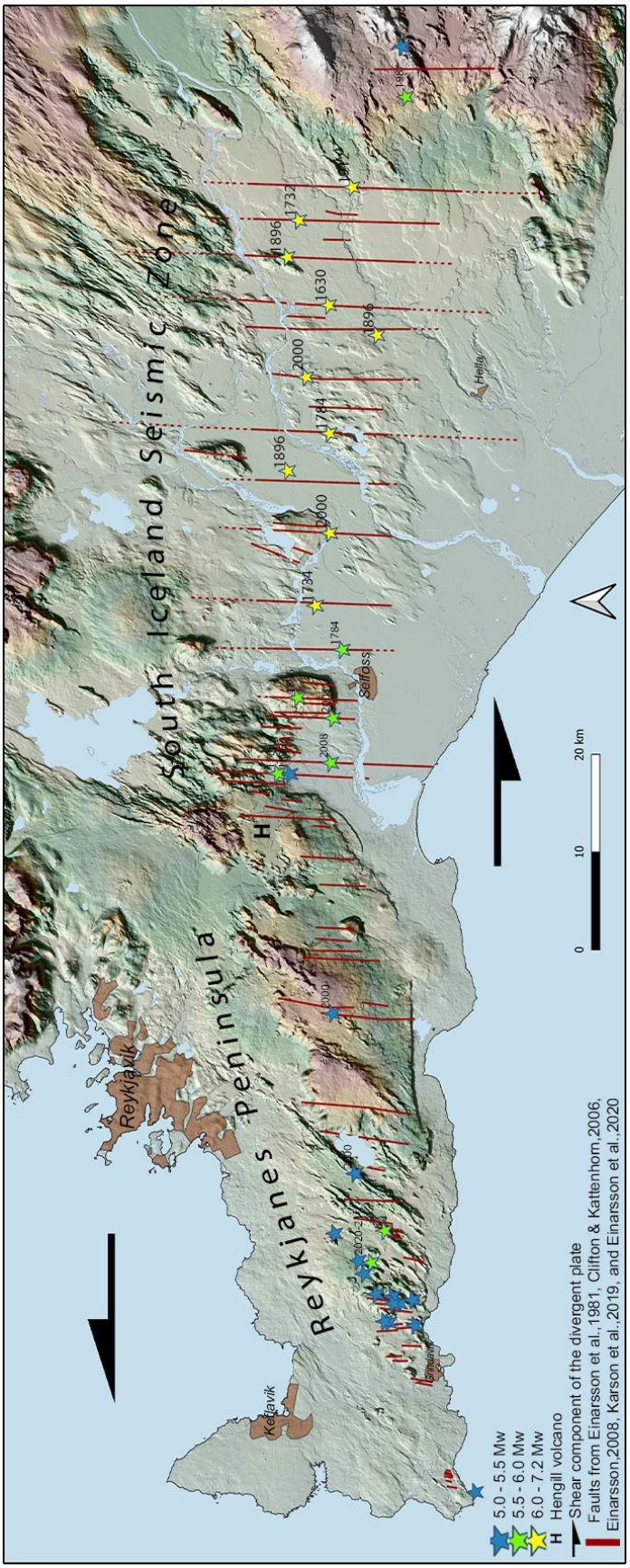

Figure 3.9: Recapitulative map of NS faults along the plates border in southwest Iceland. The main historic earthquakes (between 1600 and 1950) are approximately situated along their supposed faults and the recent high magnitude earthquakes (since 2000) are located by the South Iceland Lowland (SIL) seismometers network. Full red lines correspond to NS faults in the observed seismic activity zone and dotted line corresponds to total fault extension from literature.

Chapter 4

Methodology

4.1 Mapping strategy

To gather data on the N-S strike-slip structures spanning southwest Iceland, we undertook three field campaigns (March and August 2021 and July 2022). The initial campaigns (the two of 2021) concentrated on the Fagradalsfjall activity zone, specifically focusing on the induced earthquakes along the N-S faults (Bufféral et al., 2023; Einarsson et al., 2023). In July 2022, we revisited the region to expand the coverage from the western Reykjanes Peninsula to the eastern SISZ. The utilization of remote sensing played a crucial role in comprehensively documenting the N-S faults across this broad area.

In southwest Iceland, the vegetation is sparse, primarily consisting of moss, grass, and a few scattered small trees, with minimal forested areas. The limited vegetation cover facilitated the use of basic optical imagery of drones to observe surface fractures.

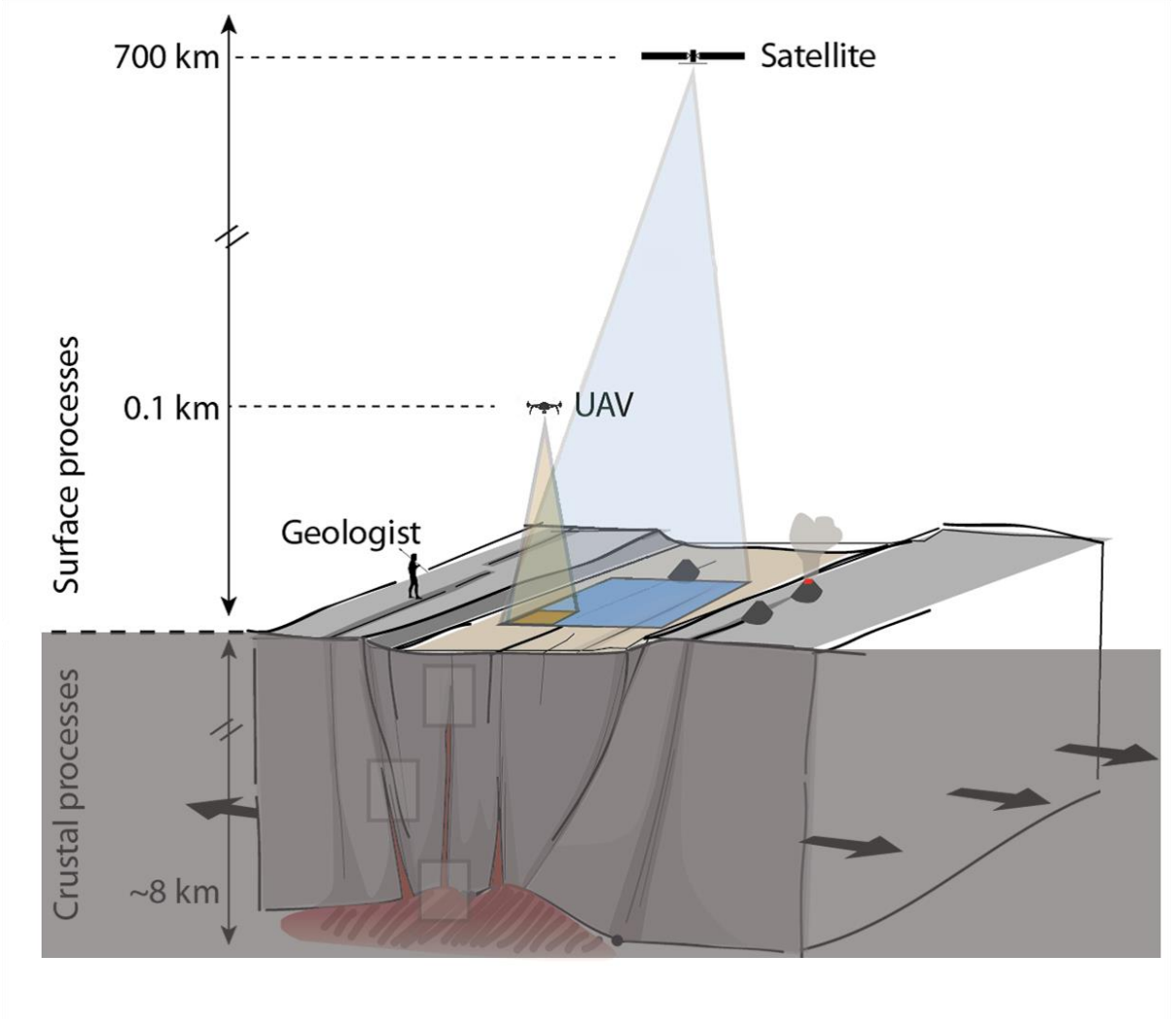

Figure 4.1: Multi-method diagram. We used different methods of data acquisition in the field as satellite imagery, aerial photography and structural observation and map. From Ruch.

While in the field, we employed various approaches for the selection and mapping of fractures. This multifaceted analysis enabled us to cover a substantial area with high resolution and to have a systematic ground control check using field observations in most cases. These methods span different scales, ranging from the most local, directly on the ground, to the most global, utilizing satellite data. These methods include various structural mapping approaches, from field observations to aerial photography, drone surveys and satellite imagery (Figure 4.1).

Given the broad area of study over 150 kilometres from west to east, we focused on selected representative portions of the fault system. The selection criteria were based on two key parameters. The first parameter involved spacing the samples strategically to encompass most of the faut system. The second parameter focused on identifying well-defined surface structures to facilitate effective mapping. To achieve this selection, we systematically sought out the most pronounced surface structures throughout the entire area using satellite imagery.

We selected five specific areas for mapping in addition to the surroundings of the 2021 Fagradalsfjall eruption site. The first area, situated to the extreme west of the Reykjanes Peninsula within the volcanic system of the same name, was chosen near the Reykjanesviti geothermal area based on the guidance of Honorary Professor P. Einarsson (Figure 4.2). Moving to the east of the peninsula, the second area is located to the south of the Bláfjöll ski station in the municipality of Ölfus, focusing on the faults of Gudrún and Hrossahryggir (Einarsson et al., 2020; Figure 4.2) . Our intention was also to survey the Kóngsfell fault adjacent to Bláfjöll, but persistent fog during the field trip prevented drone flights in that region. To establish a connection between RPOR and SISZ, we conducted drone flights over an N-S fault identified by Steigerwald et al. in 2018, situated in the Hengill complex. The fourth zone, located in the middle of SISZ, covers the Hestfjall hill and the adjacent plain, where a significant M6.0 earthquake occurred in June 2000 (Bergerat & Angelier, 2003; Jónsson et al., 2003; Figure 4.2). The last area is situated in East-SISZ, encompassing the faults of Vindáls, Réttarnes, Leirubakki, Tvörvafit, and Selsund (Figure 4.2). These faults are correlated with earthquakes likely occurring in 1630, an unknown date, 1294 or 1732 (or both), unknown, and 1912, respectively (Bjarnason et al., 1993; Einarsson, 2010; Einarsson et al., 1981).

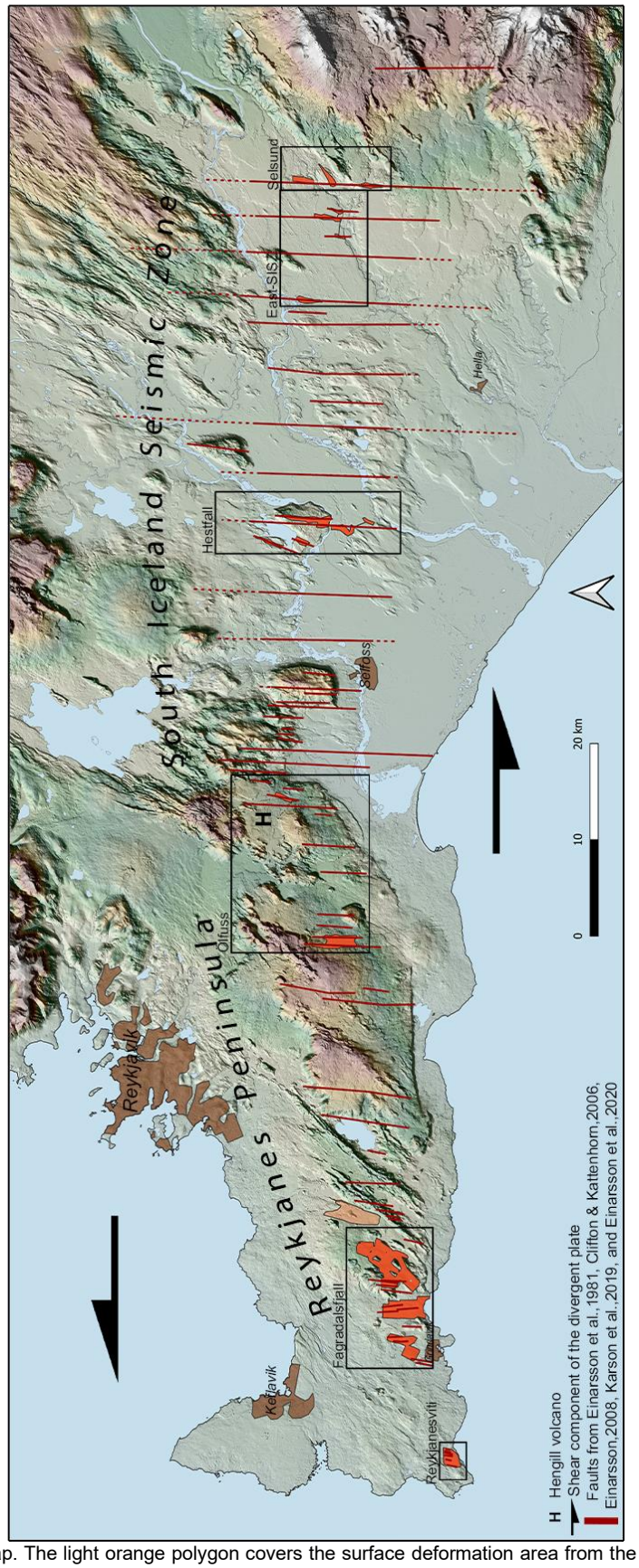

Figure 4.2: Flight zone map. The light orange polygon covers the surface deformation area from the October 2020 earthquake but there is no surface fracture visible there. The darker orange polygons are the uav-flight zone with visible surface fracture. They are merged in six zones geographically: Reykjanesviti, Fagradalsfjall, Ölfus, Hestfjall, East-SISZ, and Selsund. Selsund is individualized of East-SISZ area and Hengill is merged with Ölfus area to have approximately the same number of structures in each zone.

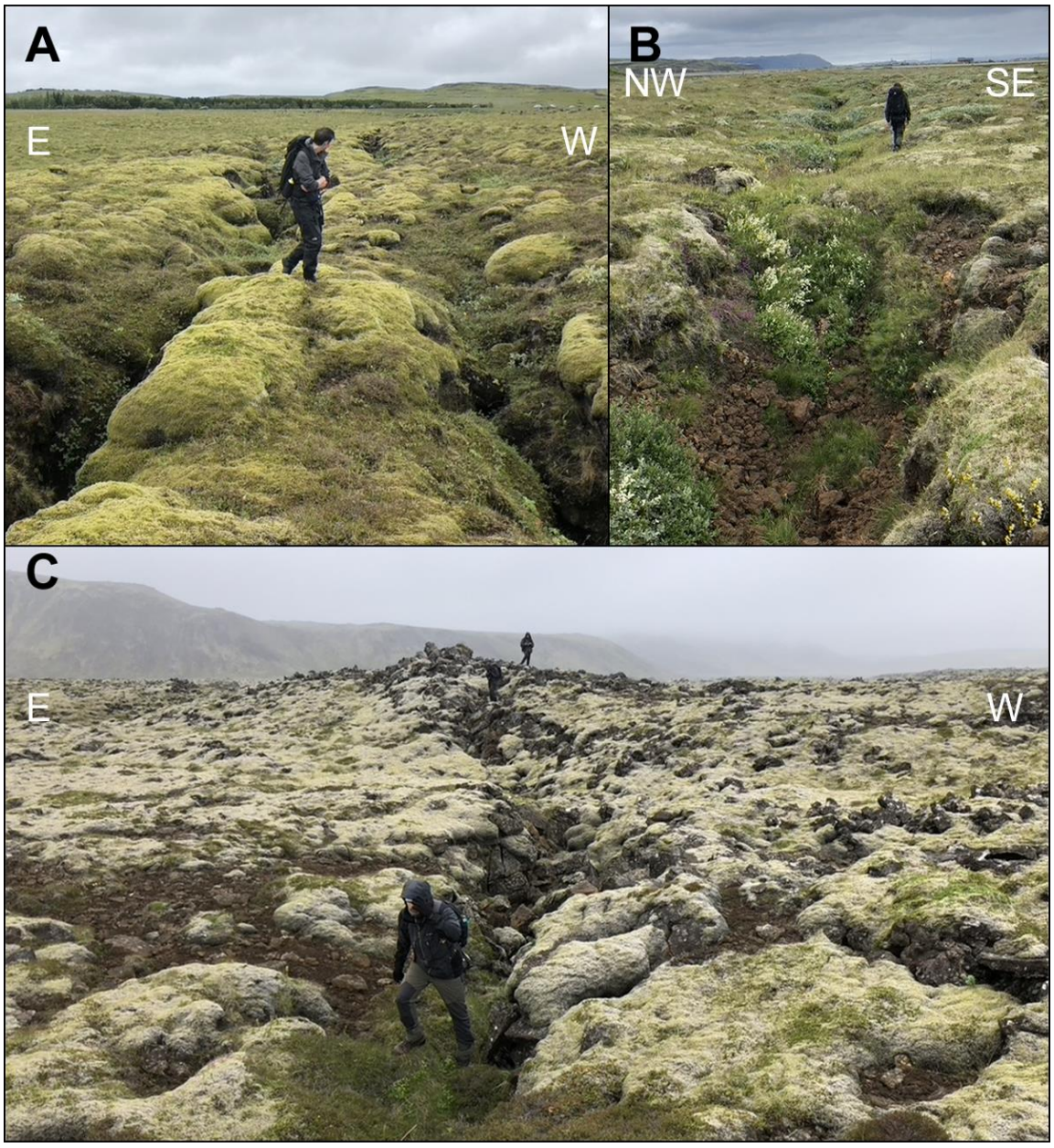

Figure 4.3: Field photography of surface fracture. **A:** Normal faults in the plain south of Hestfjall. **B:** NS en-echelon fractures in the plain south of Hestfjall. **C:** NS en-echelon in front of a multi-metric puh-up west of Fagradalsfjall eruption site.

Distinct soil types were identified in the surveyed areas, as their composition can influence surface structures (Figure 4.3). Around Reykjanesviti and the Fagradalsfjall eruption site, the predominant soil type consists of raw lava fields. In Hengill, the lava field is covered by a substantial layer of moss. Near Ölfus and on Hestfjall hill, a thin layer of grass characterizes the soil. Lastly, in the arable plain of South Iceland, there is a soft soil layer with grass, and even a sparse forest is present around the Leirubakki and Tvörvafit faults.

4.2 Field geology

While in the field, alongside the drone flights, we conducted structural measurements to enhance and correlate them with photogrammetry mapping. Various geological tools, including a meter, compass, and GPS, were employed for these measurements. We mostly measured the fracture strike and identified some push-ups hill from different covered areas because the other parameters were often not visible at the surface. For each measurement point and identified irregularities, we took GPS coordinates to precisely locate them. In total, we performed 100 measurements. It's worth noting that determining the true opening and its obliquity required identifying the asperity fit, which refers to the matching irregularities along the fracture's walls.

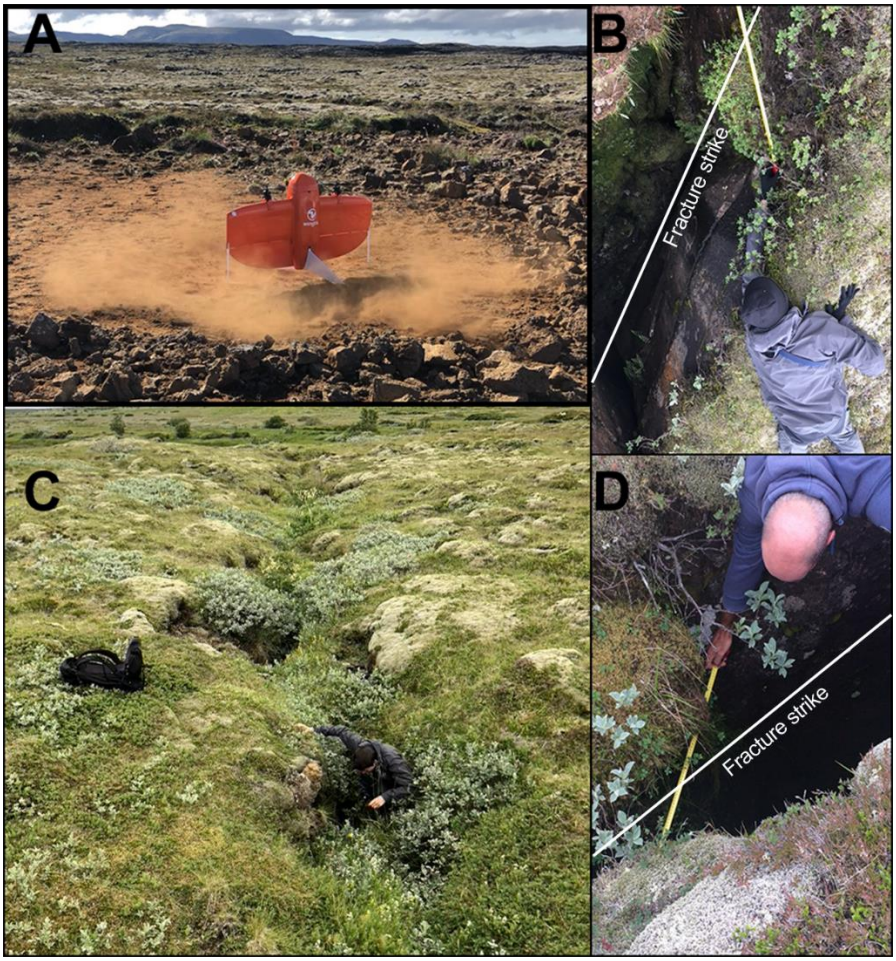

Figure 4.4: Field photography of fracture mapping. **A:** Wingtra 1 drone take off in Vogar, north of Fagradalsfjall. **B and D:** True opening measurement thanks to asperity fit identification in Hestfjall hill. **C:** Looking in the fracture to find asperity fit in the plain south of Hestfjall.

The examination of asperity fit is crucial for the study of fault kinematics. Through this analysis, we can delve into the mechanics of faulting, gaining valuable insights into the history and dynamics of geological processes of the studied area. Asperity fit enables us to ascertain the true movement of the opening, including its strike and length, utilizing the compass and meter, respectively (Figure 4.4 B, C and D).

4.3 Aerial photogrammetry and mapping

Photogrammetry is a technique employed to extract accurate three-dimensional information about the shape and scale of structures or landscapes from two-dimensional photographs. This process involves capturing, measuring, and interpreting images to create precise and detailed three-dimensional models. Various methods, such as LiDAR, ground photography, or aerial photography, can be used for data acquisition. To cover a large area, we opted for an Unmanned Aerial Vehicle (UAV) to collect optical images. Given the sparse vegetation in Iceland, it was not necessary to utilize LiDAR as a radar-based method to penetrate it. Additionally, the use of optical photography provided color information in conjunction with the Digital Elevation Model (DEM).

In summer 2022, we conducted surveys in all the previously mentioned areas using a Wingtra® fixed-wing UAV, classified as a Tailsitter Vertical Take-Off and Landing device (Figure 4.4 A). This plane-like drone has the capability to cover up to 1.3 square kilometres per flight within a 50-minute timeframe, provided good weather conditions and an optimal flight plan. Equipped with a SonyRX1RII, 35mm, full-frame, 42 MP camera, the UAV captured images at an altitude of approximately 100 meters. Due to the relatively flat terrain, the flight heights above ground level remained relatively

consistent. This elevation range was chosen as a compromise between ensuring sufficient overlap of images and achieving optimal pixel precision (Bufféral et al., 2023). The planned overlap (both frontal and on the side) was set at 70% during the flight, ensuring each point was covered by at least 9 pictures, a requirement for effective correlation in the three-dimensional model.

During the survey, we conducted a total of 36 flights distributed across all the covered zones, encompassing an approximate total area of 35.5 square kilometres. This comprehensive effort resulted in the capture of nearly 50,000 pictures throughout these flights.

The Wingtra® software can automatically georeference the images using the UAV's onboard GPS. However, to enhance accuracy to 2-3 centimetres, we employed Global Navigation Satellite System (GNSS) with Post Processing Kinematic (PPK) using a Trimble R2 antenna that we installed nearby during the flight survey. PPK involves differential calculations between a temporary GNSS base of known position and a GNSS antenna onboard, recording location data on the camera SD card. This method offers the advantage of not necessitating Ground Control Points (Bufféral et al., 2023).

With this precise georeferencing, we aligned the UAV pictures in Agisoft Metashape® software and we verify their consistency by keeping only the one with an estimated image quality above 0.7. Subsequently, on Agisoft, we computed a three-dimensional dense point clouds with the calculation of the point colour to conclude the photogrammetry analysis. It was run with a downscaling factor of 4 in comparison to the original photos as a compromised between computing time and resolution.

To map the fractures, we needed to make these three-dimensional point clouds more usable in mapping software, which involved converting them into lighter and two-

dimensional data. In Agisoft Metashape, we projected the elevation data onto Digital Elevation Models (DEM) raster with a resolution of 2-4 centimetres per pixel. Additionally, working with optical imagery allowed us to extract color orthophotos, which are the relief-corrected and merged surface pictures, with a resolution of 1-2 centimetres per pixel to complement the DEMs.

Combining data from the DEMs and orthophotos, we manually mapped the visible surface fractures in each selected zone. The fractures were mapped as a single line or divided into different segments. Cartography was conducted at a scale of 1:150 for soft soil areas and 1:200 for rockier terrain. The 2021 data, originating from around the Fagradalsfjall eruption, were mapped by different operators than the others, introducing a potential source of subjective error. Additionally, the largest N-S structures in this dataset were not well defined, and their selection was arbitrary, following a general N-S alignment.

Apart from mapping the fractures of the N-S faults, we also documented the fissure swarms intersecting them, as well as the NE-SW faults corresponding to the conjugate of the studied N-S faults, reflecting the Riedel structures in the system. Beyond directly observed surface fractures, we mapped larger en-echelon structures, ranging from alignments of surface fractures to alignments of alignments. Lastly, we also documented push-ups occurring between the en-echelon structures.

id	FlightZone	Type	Comment	Push-Up ?	StructSize	Certitude	Longitudes	angle	Length	fid	Zone
NULL	Meradalir_North	Push-Up	Elisabetta Mapped	Yes	2	1	-22,23499	104	20.043	4357	2Fagradalsfjall Zone
NULL	Stóri-Hrútur_East	Push-Up	Elisabetta Mapped	Yes	2	1	-22,229869	109	11.346	4358	2Fagradalsfjall Zone
12	Selsund_South	Push-Up	NULL	Yes	1	1	-19,971057	148	62.314	4359	6Selsund-Fault Zone
39	Selsund_South	Off-Axis Push-Up	Off Axis Structure	Yes	0	1	-19,969266	23	10.052	4360	6Selsund-Fault Zone
40	Selsund_South	Off-Axis Push-Up	Off Axis Structure	Yes	0	1	-19,969957	146	13.169	4361	6Selsund-Fault Zone
42	Selsund_South	Push-Up ?	NULL	Yes	1	2	-19,969336	109	23.229	4362	6Selsund-Fault Zone
43	Selsund_South	Push-Up	NULL	Yes	1	1	-19,96934	30	6.231	4363	6Selsund-Fault Zone
44	Selsund_South	Push-Up	NULL	Yes	1	1	-19,969196	60	20.115	4364	6Selsund-Fault Zone
48	Selsund_South	Push-Up	NULL	Yes	1	1	-19,970819	148	21.478	4365	6Selsund-Fault Zone
49	Selsund_South	Push-Up	NULL	Yes	1	1	-19,970992	142	13.62	4366	6Selsund-Fault Zone
50	Selsund_South	Push-Up	NULL	Yes	1	1	-19,969224	138	12.417	4367	6Selsund-Fault Zone
51	Selsund_South	Off-Axis Push-Up	Off Axis Structure	Yes	0	1	-19,968314	22	36.96	4368	6Selsund-Fault Zone
52	Selsund_South	Off-Axis Push-Up	Off Axis Structure	Yes	0	1	-19,967588	13	27.299	4369	6Selsund-Fault Zone
53	Selsund_South	Push-Up	NULL	Yes	1	1	-19,96922	68	34.697	4370	6Selsund-Fault Zone
64	Selsund_South	Conjugate Push-Up	Conjugate Structure	Yes	1	1	-19,969462	30	22.267	4371	6Selsund-Fault Zone
67	Selsund_South	Conjugate Push-Up	NULL	Yes	1	1	-19,969765	4	8.878	4372	6Selsund-Fault Zone
70	Selsund_South	Conjugate Push-Up	NULL	Yes	1	1	-19,970029	90	14.827	4373	6Selsund-Fault Zone
71	Selsund_South	Conjugate Push-Up ?	NULL	Yes	1	2	-19,97016	76	4.394	4374	6Selsund-Fault Zone
76	Selsund_South	Push-Up	NULL	Yes	1	1	-19,970649	134	31.996	4375	6Selsund-Fault Zone
83	Selsund_South	Push-Up	NULL	Yes	1	1	-19,970651	19	49.244	4376	6Selsund-Fault Zone
105	Selsund_South	Push-Up	NULL	Yes	1	1	-19,970125	129	23.617	4377	6Selsund-Fault Zone
106	Selsund_South	Push-Up	NULL	Yes	1	1	-19,969513	128	17.309	4378	6Selsund-Fault Zone
107	Selsund_South	Push-Up	NULL	Yes	1	1	-19,969544	61	12.604	4379	6Selsund-Fault Zone
108	Selsund_South	Push-Up	NULL	Yes	1	1	-19,969629	131	8.092	4380	6Selsund-Fault Zone

Figure 4.5: Dataset creation lookout. View of the attribute table of Qgis with all the different data field obtained for each structure.

In total, we documented a lot of distinct structures, all represented as lines in a vector layer within QGIS. To effectively utilize this extensive dataset, we established a database for the classification of structures with two types of data. The first, which was the one calculated through QGIS tools for each fracture, contains the Longitude, Strike, and Length fields. The second type contains various fields which were manually included, contains the Confidence in the mapping (Figure 5.12), the Zone of origin for the structure, Push-up details for discrimination, Type or name of the structure, and Struct-Size indicating the scale of the en-echelon (Figure 4.5). This second group was populated during the mapping process using the QGIS attribute table.

Furthermore, to increase the spatial extent of the map created in QGIS, the Arctic DEM (Landmaelingar Íslands Atlas) with a 2-meter resolution was utilized as a base. The

coastline and river layers were incorporated from the Lýsigagnagátt database. Additionally, the urban area layer, simplified for clarity, was manually mapped.

Regarding the plots, they were generated using MATLAB®, relying solely on the fracture dataset and the earthquake dataset, which I will introduce below. The various information fields facilitated the selection of specific data directly in the code, enabling the labelling of different information on a single plot.

4.4 Earthquake catalogue

The earthquake data were sourced from the online catalogue provided by Skjálfta-Lísa, a platform that monitors and archives seismic activity in Iceland. These earthquakes are primarily automatically detected through the permanent Icelandic South Iceland Lowland (SIL) seismic network, boasting a magnitude of completeness of M_{LW} 0 and a location error of approximately 1 kilometre (Hensch et al., 2016). This network, initiated by the Icelandic Meteorological Office to primarily monitor the South Iceland Seismic Zone (SISZ) and the Tjörnes fracture zone (Kowsari et al., 2020), was established between 1990 and 1993. It comprised 14 stations directly within the studied area and an additional 4 in its vicinity since early 2000s (Angelier et al., 2008; Figure 4.6). The SIL magnitude scale used is the local moment magnitude (M_{LW}), and it has not been converted to moment magnitude in this study.

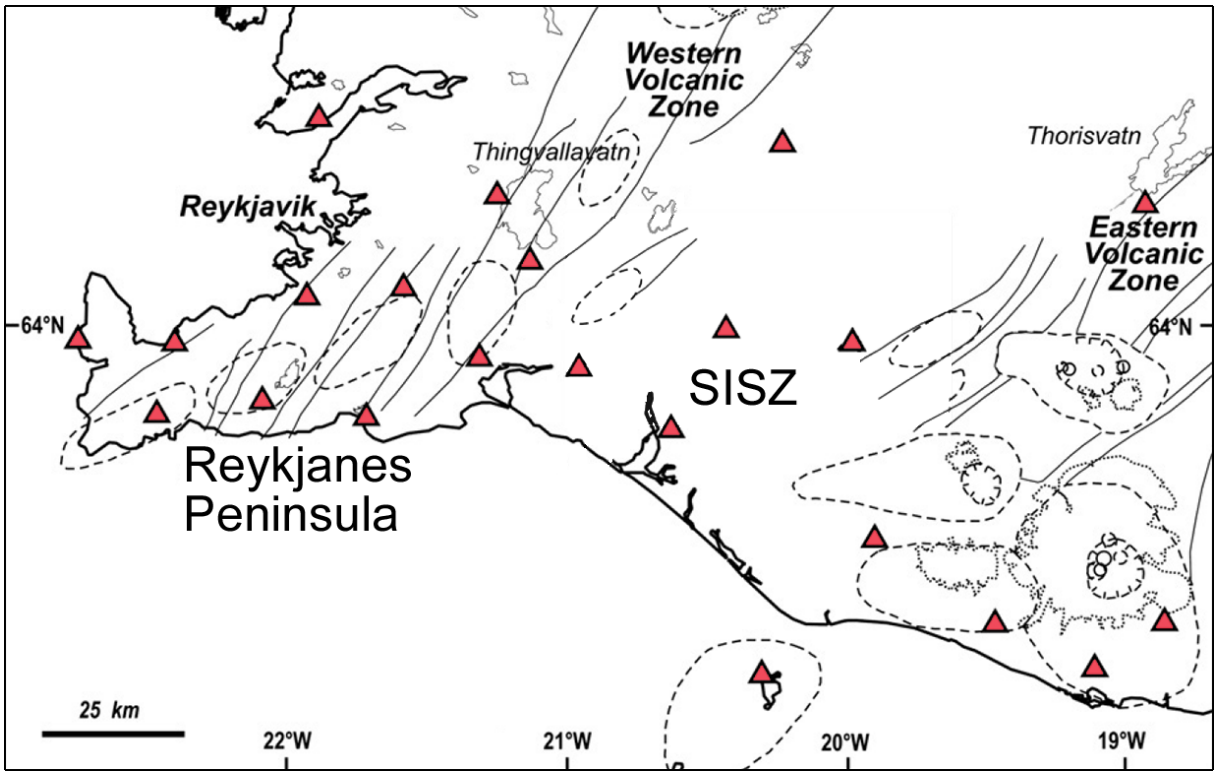

Figure 4.6: SIL station location map. Map of the seismic station, in red triangle, of the SIL system in the surrounding of the Reykjanes Peninsula and the SISZ in southwest Iceland. Modified from (Angelier et al., 2008).

For this study, we collected earthquake data from the Skjálfta-Lísa platform, specifically focusing on the Hengillinn, Reykjanesskagi, and Sudurlandsbrotabelti zones. The dataset encompasses the online database spanning from 2009 to December 31, 2022, providing a comprehensive collection of earthquake events.

Subsequently, after consolidating all earthquakes into a single dataset, we applied discrimination criteria to tag those located beyond 10 kilometres from the presumed plate boundaries, those associated with the Hengill power plant-induced seismicity cluster, and those with a magnitude lower than 2 M_{LW}. This discriminatory process was executed, like the fractures' data information field, to be able to restrain to the desired data directly in MATLAB® code.

Chapter 5

Results

5.1 Field observations and mapping

In this section, we present the data obtained in the field through maps and structural field measurements. The maps created onsite are approximate and the mapped structures are positioned relatively together. We covered three main NS faults in different areas, spanning the Reykjanes Peninsula and the SISZ. From west to east, these areas include west of the 2021 Fagradalsfjall eruption site, the northern part of the Gudrun fault in the Ölfus area, and the Bitra fault reactivated during the June 2000 event to the south of Hestfjall hill (Figure 5.1).

The structures mapped on the NS strike-slip faults in these onsite maps exhibit clear arrangements in different scales of en-echelon (Figure 5.1 and 5.2 A). The individual fractures are oriented NE-SW, and their alignment is more in the NS direction, similar to the main faults. Some positive topographic anomalies are located between the strike-slip fractures (Figure 5.2 B and Figure 5.5 C and D). These structures are characterized by compressional push-ups, typically located between en-echelon

features. The larger push ups can be multi-metric and are positioned between the largest en-echelon scales.

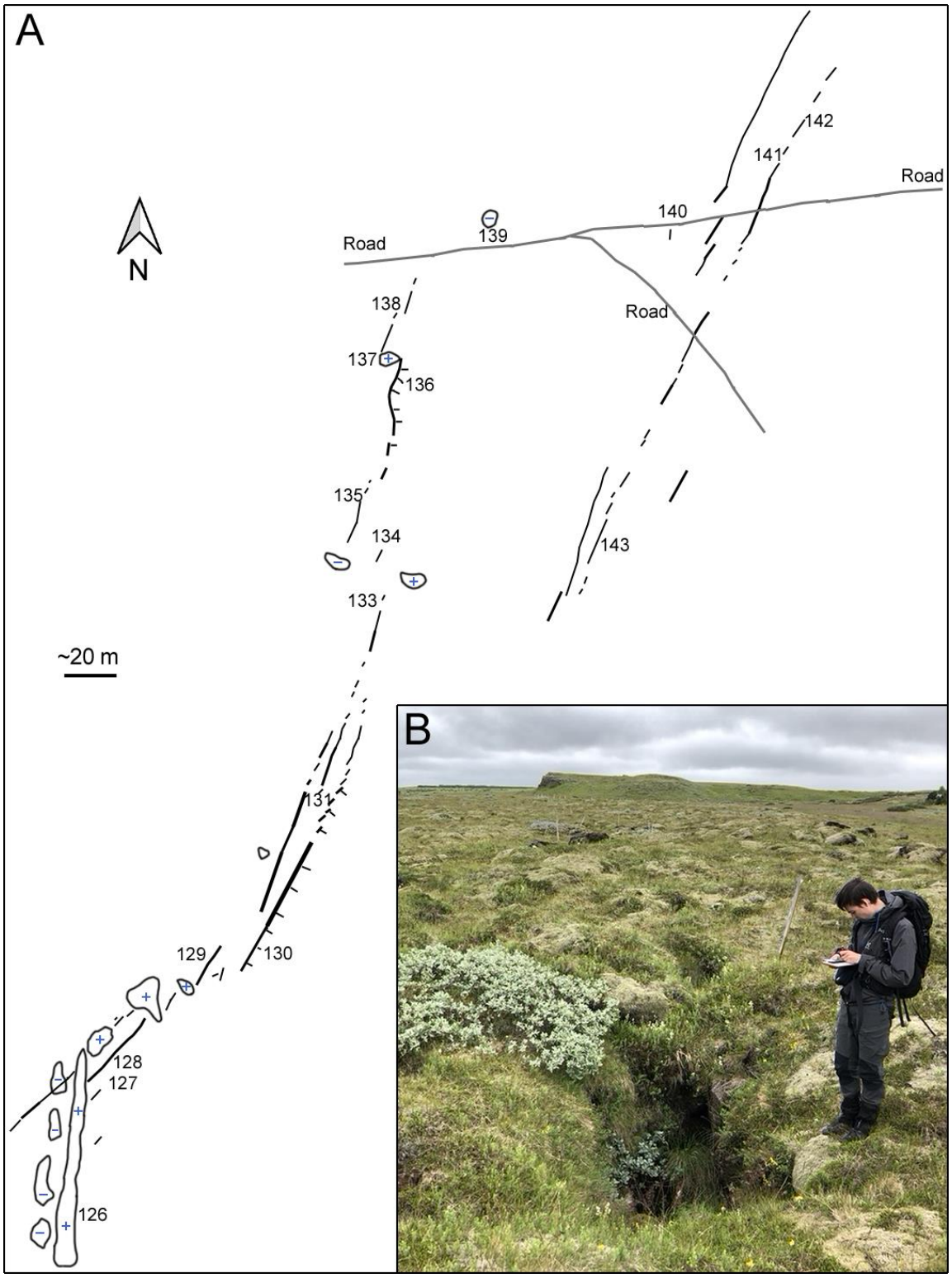

Figure 5.1: Field mapping. **A:** Map of a part of the plain south of Hestfjall. Each number corresponds to a GPS point taken, and the **+** and **-** sign to a positive or negative respectively topography area. **B:** Mapping a fracture on the field in the plain south of Hestfjall, 100 metres further south of the map in A.

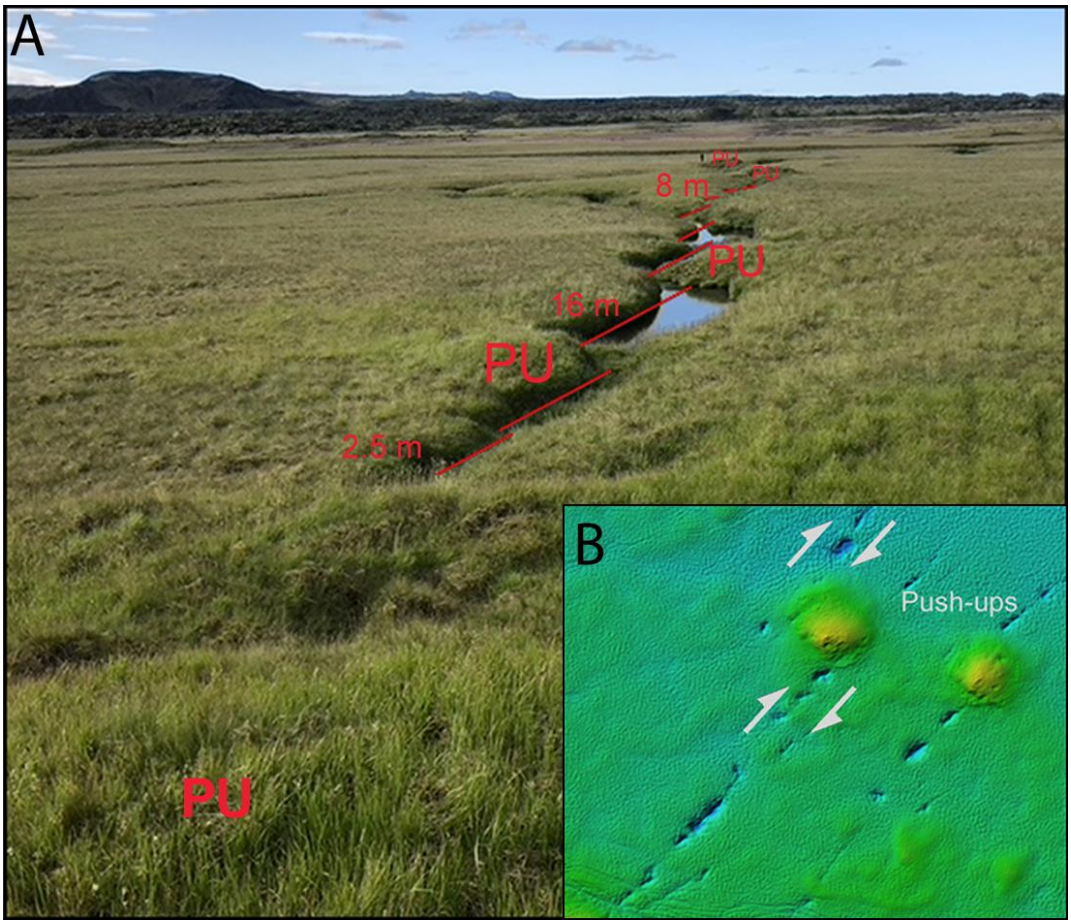

Figure 5.2: A: En-echelon fractures observation in south Selsund, with PU for push-up. **B:** DEM map of en-echelon fractures and push-ups. Shearing direction is shown in grey arrow for two arrays, enhancing the compression origin of push-ups.

We observe different levels or scales of alignment in the en-echelon structures. Here we used the terminology proposed by Bergerat et al. in 2003. There are five scales, with the largest tending to be more NS-oriented (Figure 5.3). The smallest scale consists of the fractures (tens of centimetres in length), which are the main structures observed in the field. Next, they align in arrays (few metres in length), which are sometimes visible in the field as topographical depressions. Scales larger than the array are not directly visible in the field, and therefore, they are interpreted in the mapping by fitting the alignment of smaller scale structures. Above the arrays, there are segments (from fifty to hundreds of metres in length), followed by faults (from hundreds of metres to one kilometre). The largest scale of the en-echelon is the NS faults (from three to fifteen kilometres in length) described earlier, which are not accurately mapped from the drone photogrammetry.

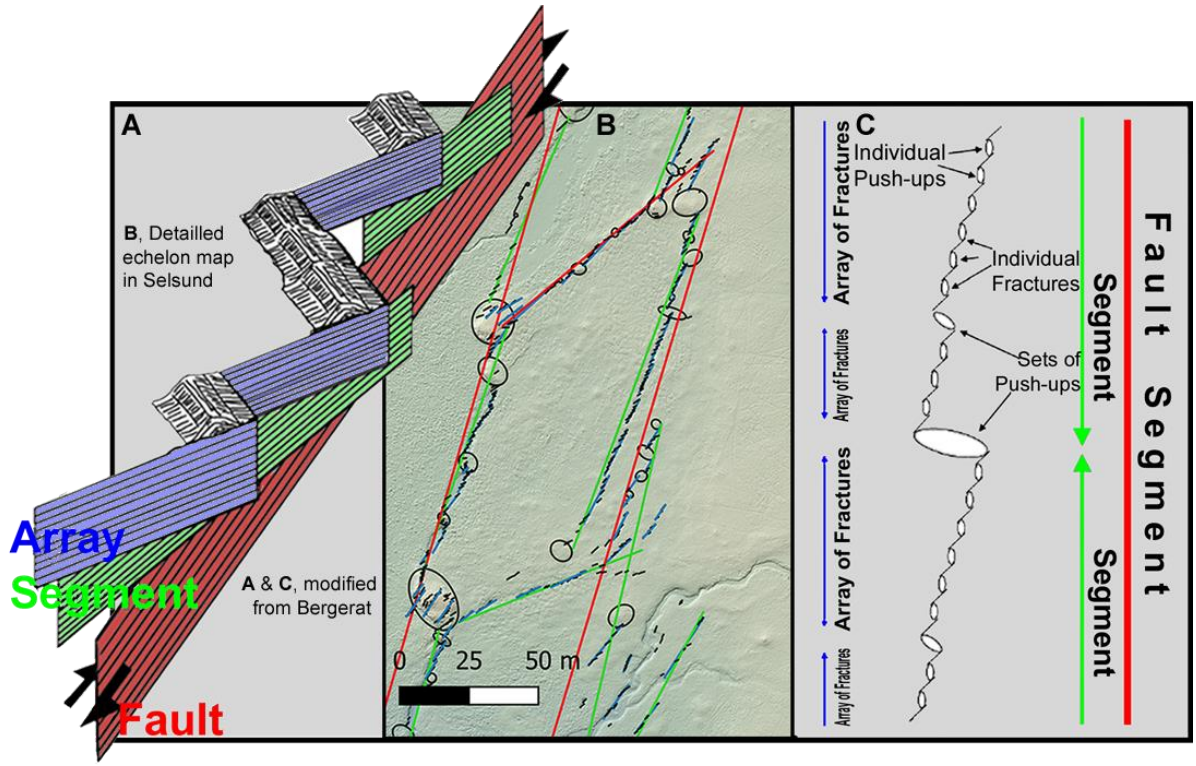

Figure 5.3: En-echelon structures observations. The structure are colorized in the same colour code than everywhere with in red the faults, in green the segments, in blue the arrays, and in black the fractures. **A:** Schematic interpretation of a multi-scale en-echelon arrangement with their correlated push-ups and their depth structures connexion. Modified from YY. **B:** Surface precise map of the four mapped en-echelon scale in a part of south Selsund. **C:** Simplified surface map of the en-echelon organisation of the NS faults. Modified from (Bergerat et al., 2003).

We identified only 21 distinct asperity fits, with half of them located in the Reykjanes fissure swarms, a few kilometres north of the plate border area near Vogar. The measured opening obliquity of the NS faults is consistently right-lateral, predominantly exhibiting high obliquity (Figure 5.4). Indeed, the majority of the measured obliquities are above 60° (Figure 4.4 B and D). In the plain south of Hestfjall hill, there is a left-lateral measured obliquity in a fracture-oriented NE-SW, like the identified conjugate of the NS fault. Additionally, adjacent to the left-lateral opening, there is a fault without obliquity, classified as a normal rifting fault in the field due to its significant vertical offset (Figure 5.5 A).

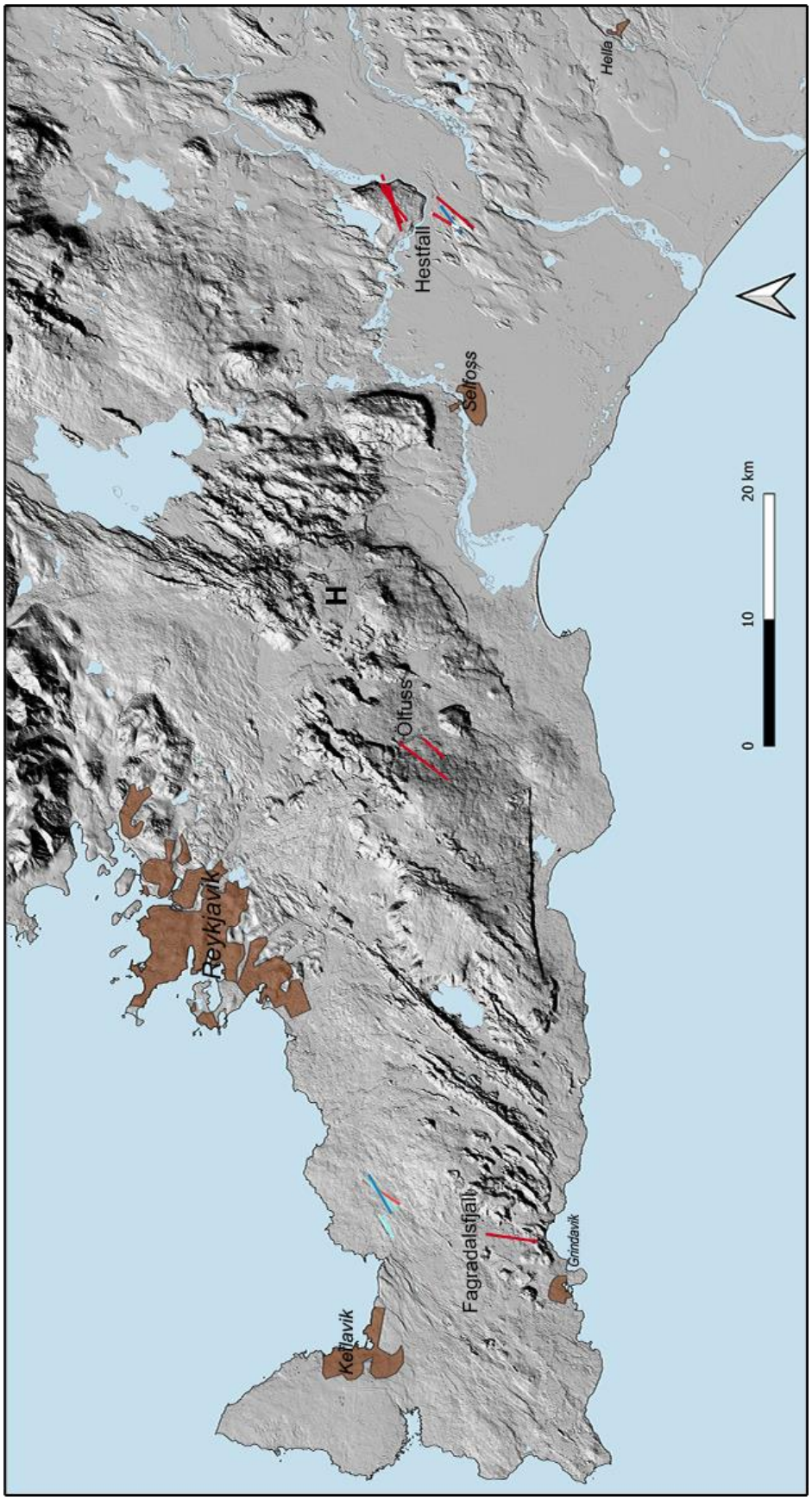

Figure 5.4: Opening obliquity map. The opening obliquity data are displayed in line oriented in function of the fracture strike and of length determined in function of the true opening. The obliquity is shown with the colour bar, where dark blue corresponds to 30° or more of left lateral obliquity, white corresponds to 0° obliquity, and dark red corresponds to 30° or more of right lateral.

5.2 GIS mapping

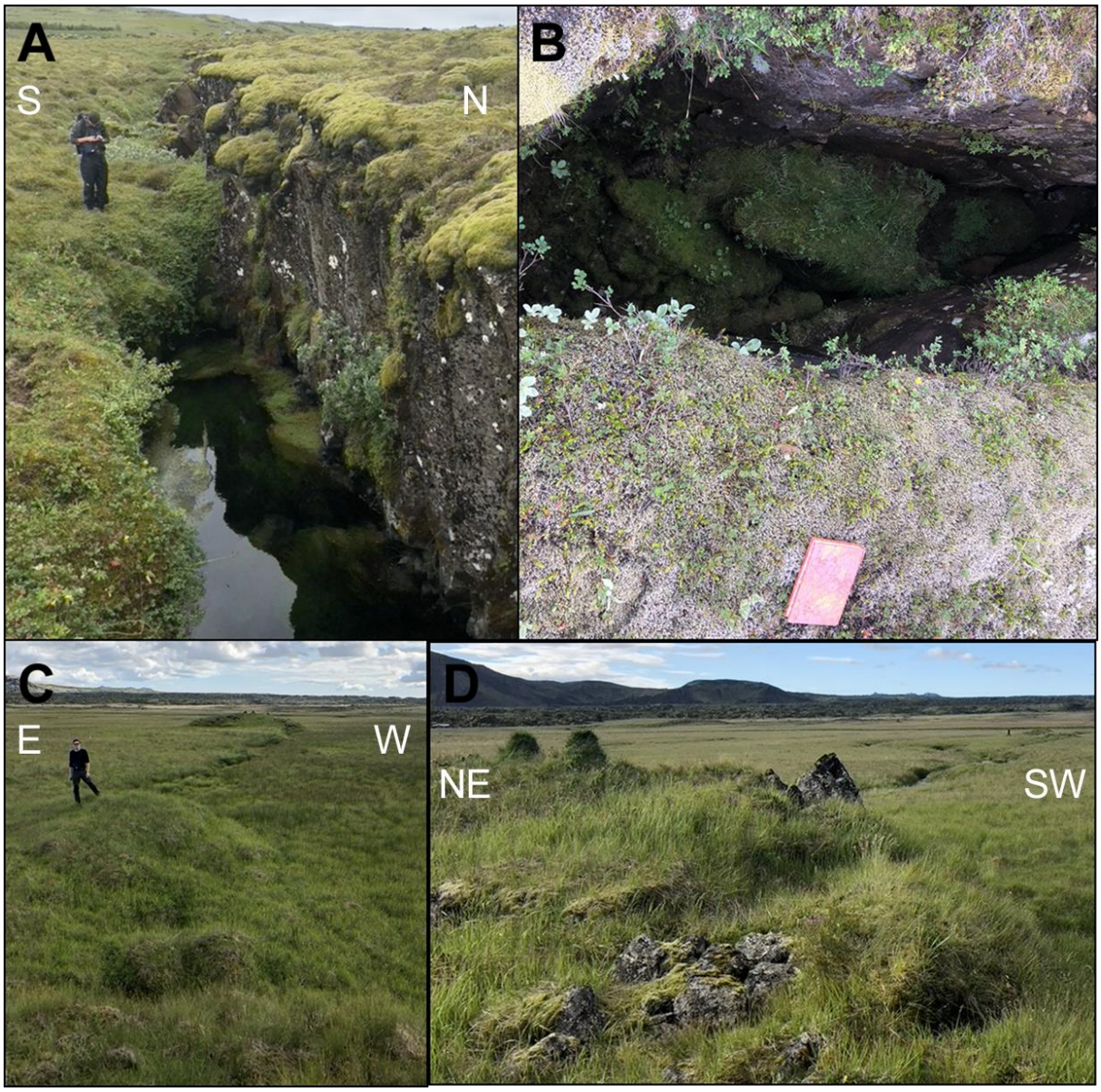

Figure 5.5: Field photography of observe structures. **A:** Normal faults in the plain south of Hestfjall with few metres of vertical reject. **B:** NS fractures with an important right lateral opening (XX°) with a nearly vertical dip in Hestfjall hill. **C and D:** Large multi-metrics push-ups along a NS fault in south Selsund.

The mapping of these en-echelon structures derived from photogrammetry results is considerably more precise than the onsite maps and offer an unprecedented overview on their spatial coverage, geometry, orientation, and distribution. These fractures are mapped and localized directly on the DEMs and orthophotos, resulting in a total of approximately 19,500 structures (Figure 5.6, 5.7, 5.8, 5.9, 5.10, and 5.11). Among

these mapped features, only a little over 14,000 are retained and displayed in the final results; the remained ones consist of non-definitive or remapped structures. Additionally, this dataset is combined with around 4,000 selected fractures mapped by Elisabetta Panza near the Fagradalsfjall eruption.

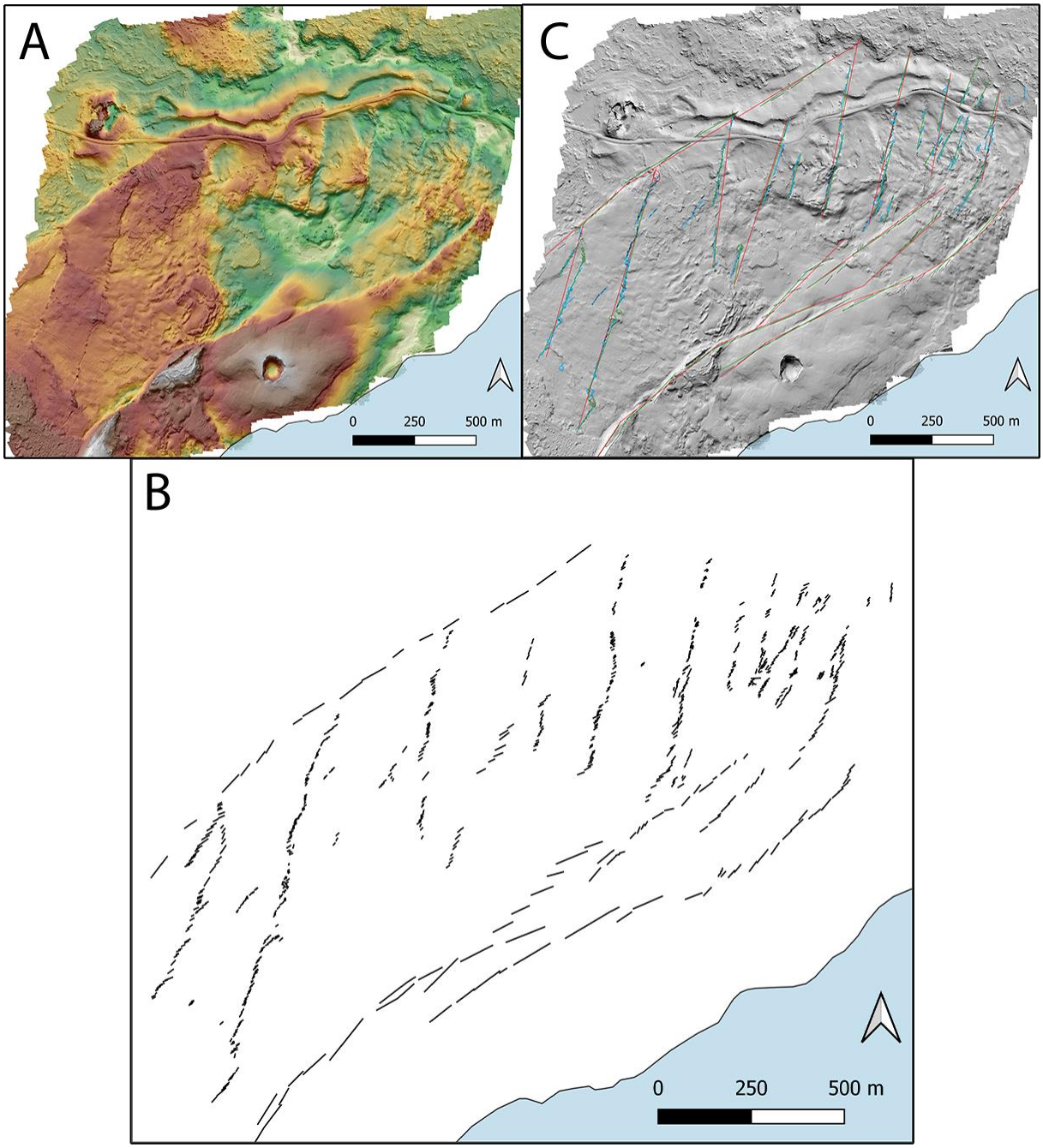

Figure 5.6: Mapping results of the Reykjanesviti area. **A:** Raw DEM obtained by drone pictures. **B:** En-echelon fractures' size only map. **C:** En-echelon larger size (arrays in blue, segments in green, and faults in red) on a shaded relief map.

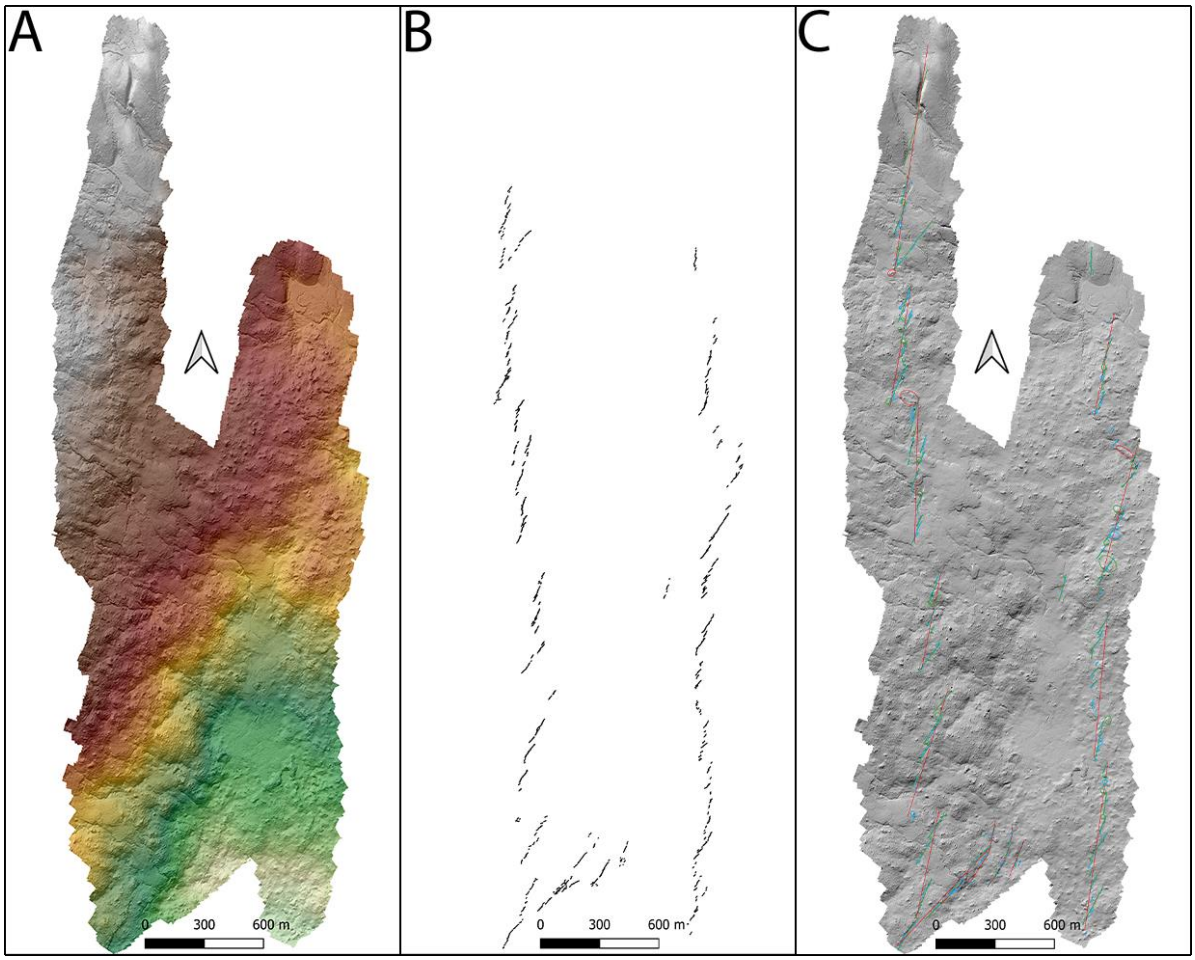

Figure 5.7: Mapping results of the western part of Ölfus area. **A:** Raw DEM obtained by drone pictures. **B:** En-echelon fractures' size only map. **C:** En-echelon larger size (arrays in blue, segments in green, and faults in red) on a shaded relief map.

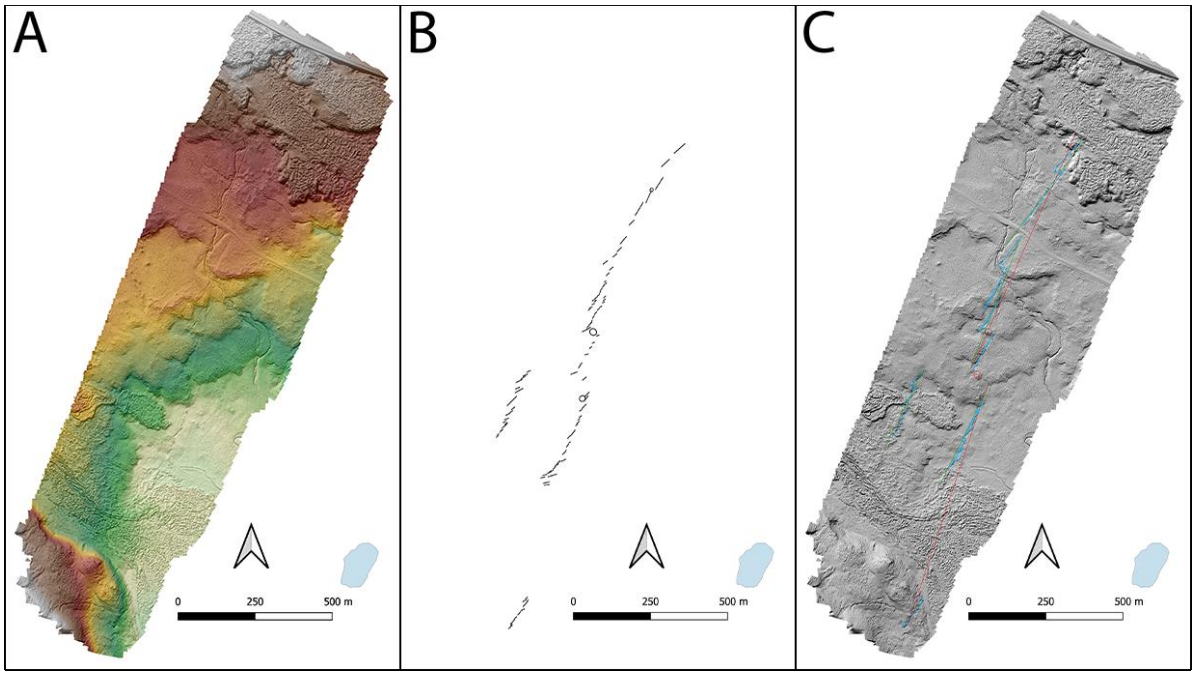

Figure 5.8: Mapping results of the eastern part of Ölfus area, at Hengill. **A:** Raw DEM obtained by drone pictures. **B:** En-echelon fractures' size only map. **C:** En-echelon larger size (arrays in blue, segments in green, and faults in red) on a shaded relief map.

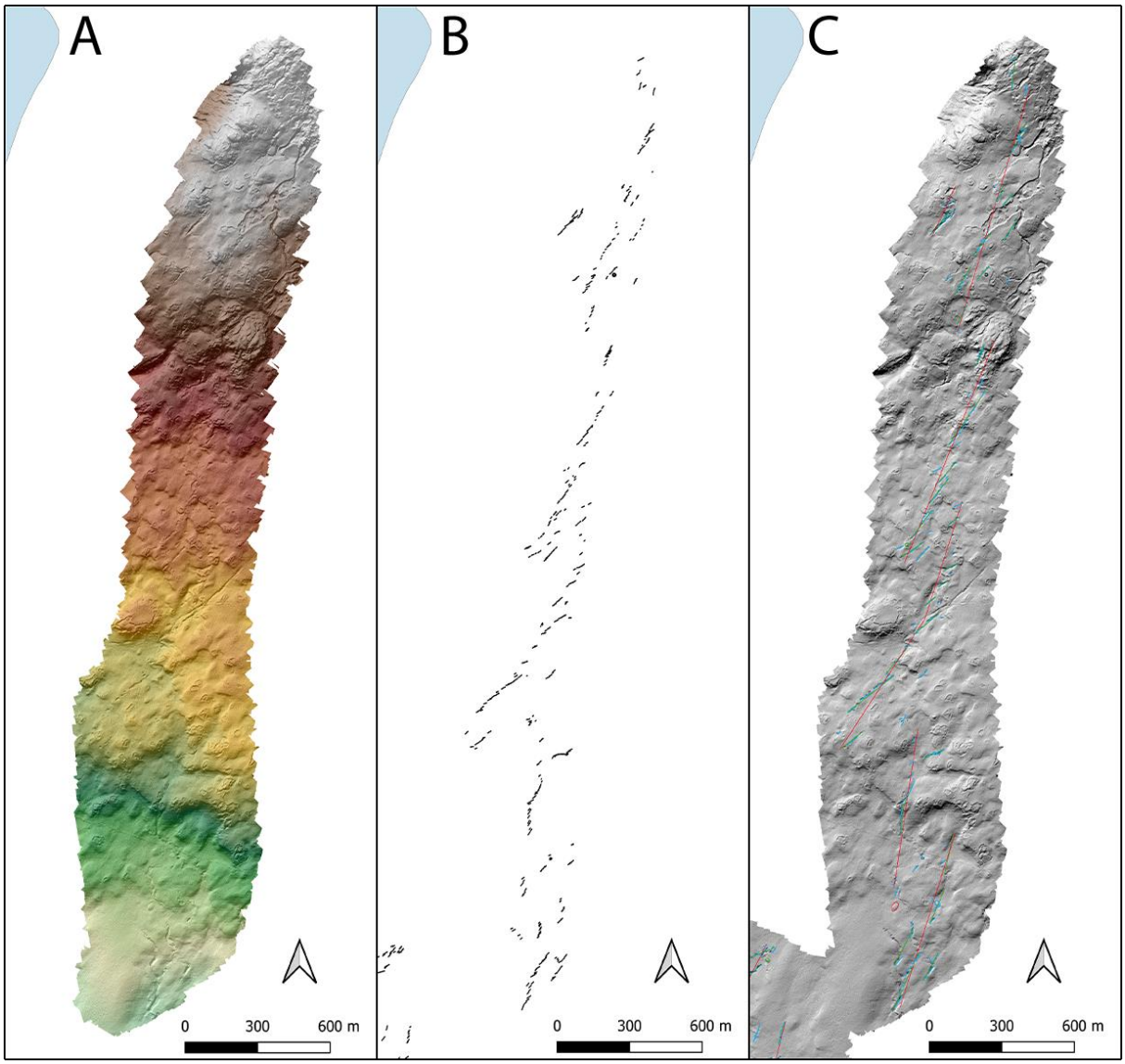

Figure 5.9: Mapping results of the Hestfjall hill area. **A:** Raw DEM obtained by drone pictures. **B:** En-echelon fractures' size only map. **C:** En-echelon larger size (arrays in blue, segments in green, and faults in red) on a shaded relief map.

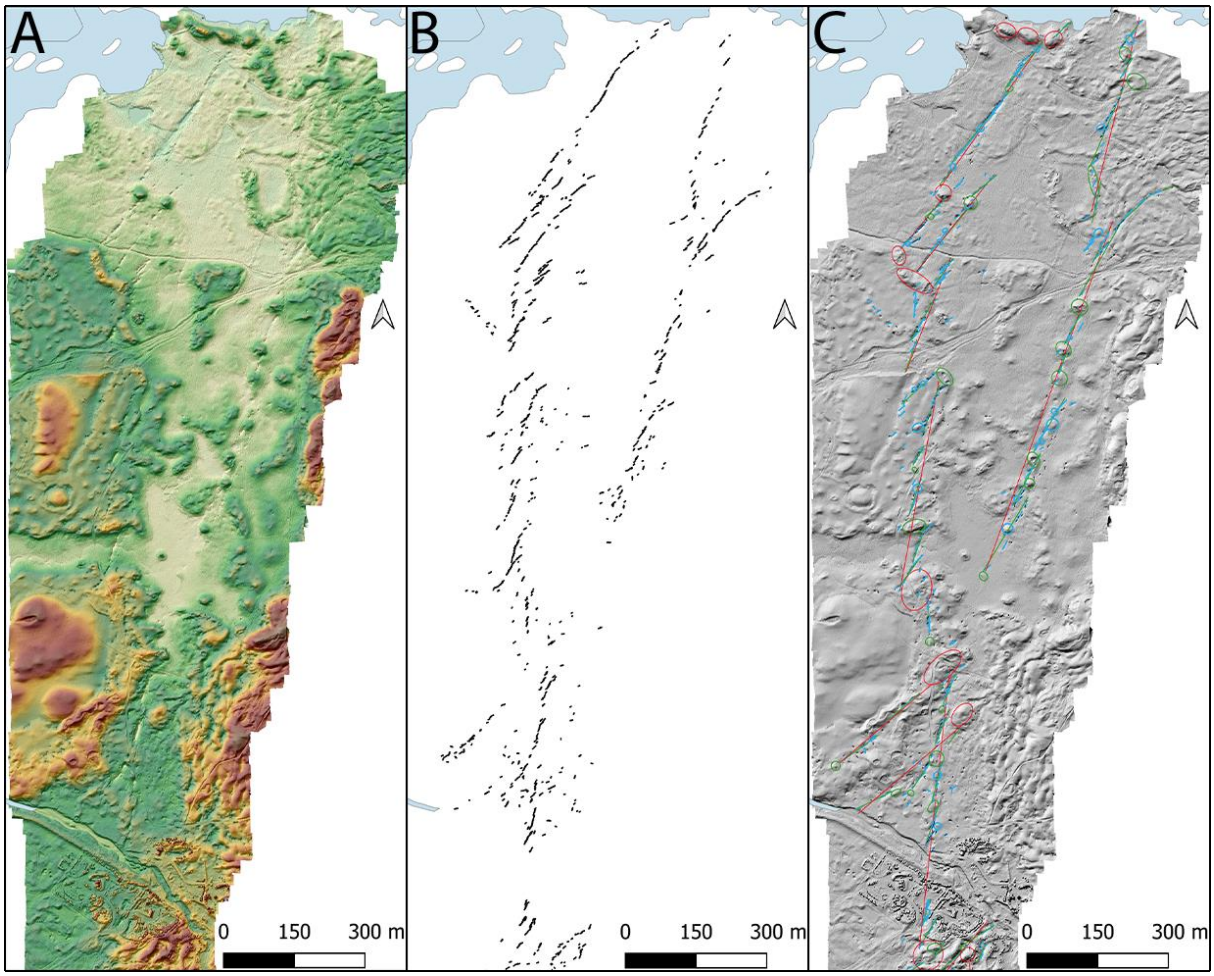

Figure 5.10: Mapping results of the western studied NS fault of the East-SISZ area, Vindáls. **A:** Raw DEM obtained by drone pictures. **B:** En-echelon fractures' size only map. **C:** En-echelon larger size (arrays in blue, segments in green, and faults in red) on a shaded relief map.

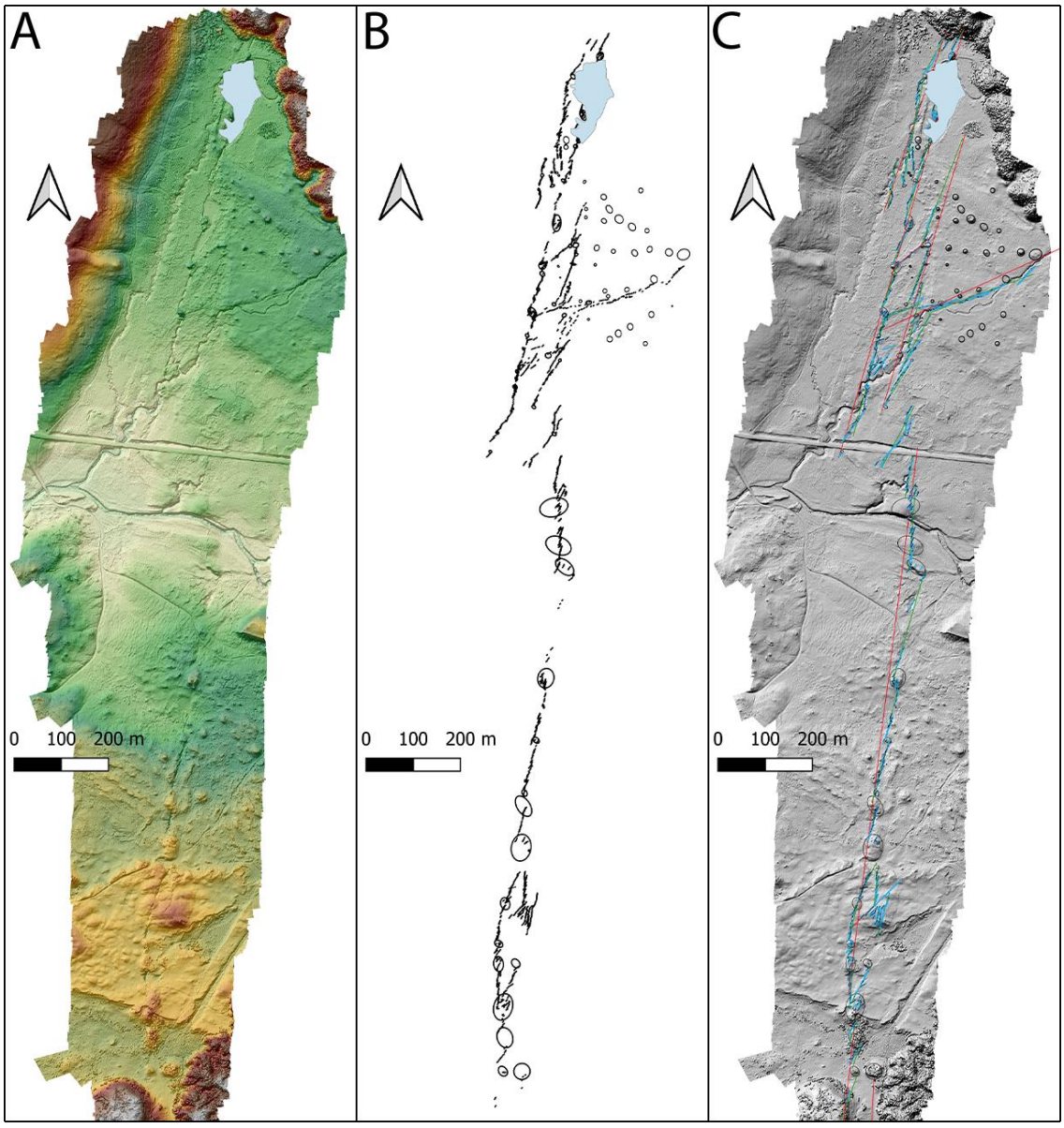

Figure 5.11: Mapping results of the south Selsund area. **A:** Raw DEM obtained by drone pictures. **B:** En-echelon fractures' size only map. **C:** En-echelon larger size (arrays in blue, segments in green, and faults in red) on a shaded relief map.

We identified three distinct types of structures across the entire study area. They are categorized into three fault families based on their alignment strikes or the presence of a prominent vertical offset. The most prevalent type is oriented N-S and referred to as N-S Riedel prime (R') shear faults. The other two families are oriented NE-SW, distinguished by the presence or absence of a vertical offset, and are named NE-SW Normal faults and NE-SW Riedel (R) shear faults (like the left lateral opening obliquity seen previously), respectively.

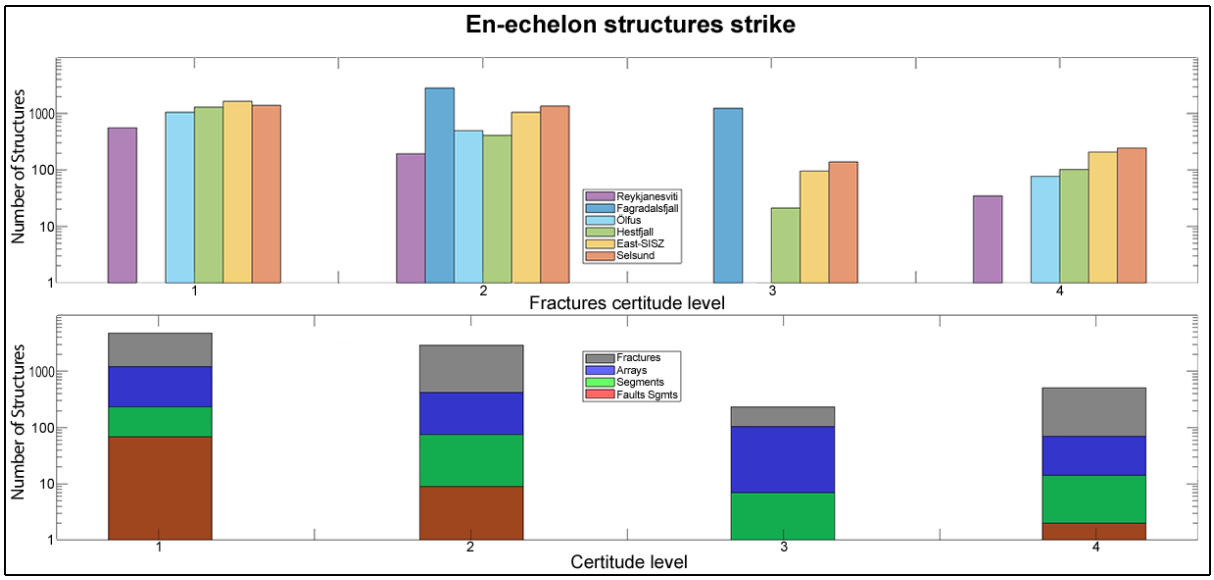

Figure 5.12: Mapping confidence histogram. Each structure has an associated certitude level from 1 to 4, that correspond respectively to absolute certainty, high confidence, high confidence but with an external uncertainty factor (like vegetation, erosion, water), and moderate confidence. **A:** Fractures' confidence displayed in function of the six different zones. **B:** Confidence for each scale of en-echelon structures.

In Vindáls, westernmost fault of East-SISZ area, and south-Selsund (see Figures 4.2 for location; Figures 5.10 and 5.11), which represent two of the most intricately studied regions along with the Fagradalsfjall surroundings due to their particularly soft soil, various non-aligned structures were observed. These include isolated push-ups in Selsund and individual fractures or small arrays around the main fault traces in Vindáls.

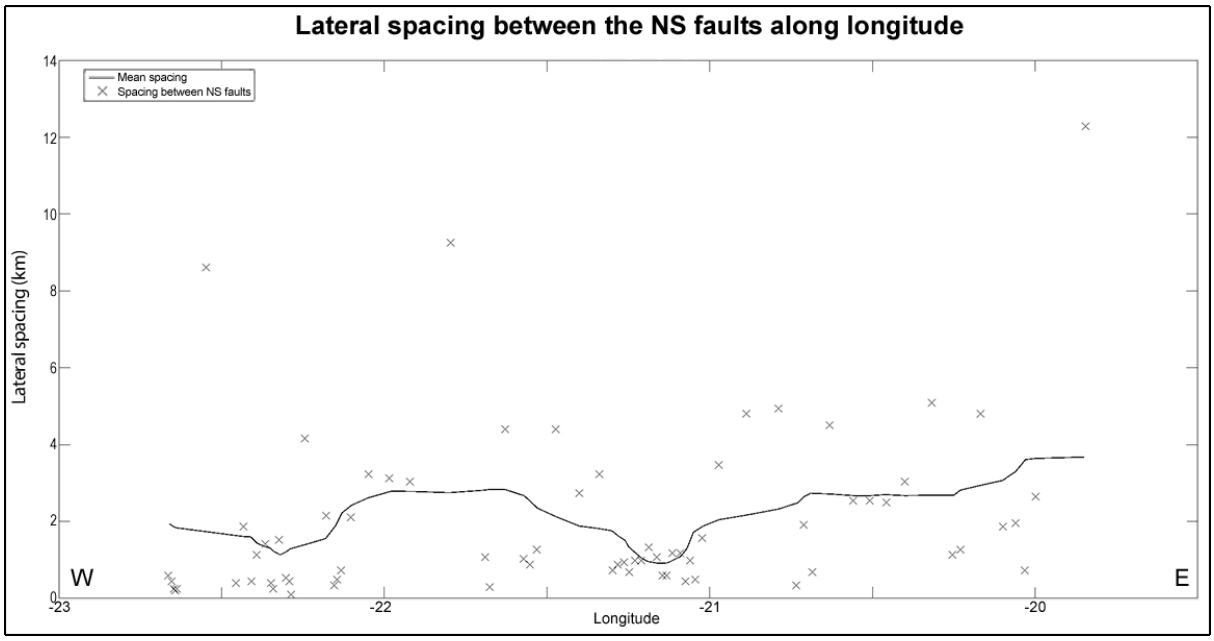

Figure 5.13: Lateral spacing between NS strike-slip faults from the literatures. The local mean is obtained by a moving window of 10.

The data obtained from GIS mapping is presented in various plots, primarily comprising two main types of figures. The first type includes rose diagrams that highlight the structures' strike based on their respective geographic zones (Figure 5.16). The second type consists of plots illustrating the structures in relation to their longitude, along a W-E projection, showcasing the fracture strike (Figure 5.14), length (Figure 5.15), or their numerical distribution. Additionally, the means, localized along the longitude for the second type of figures, are calculated and depicted on the plots.

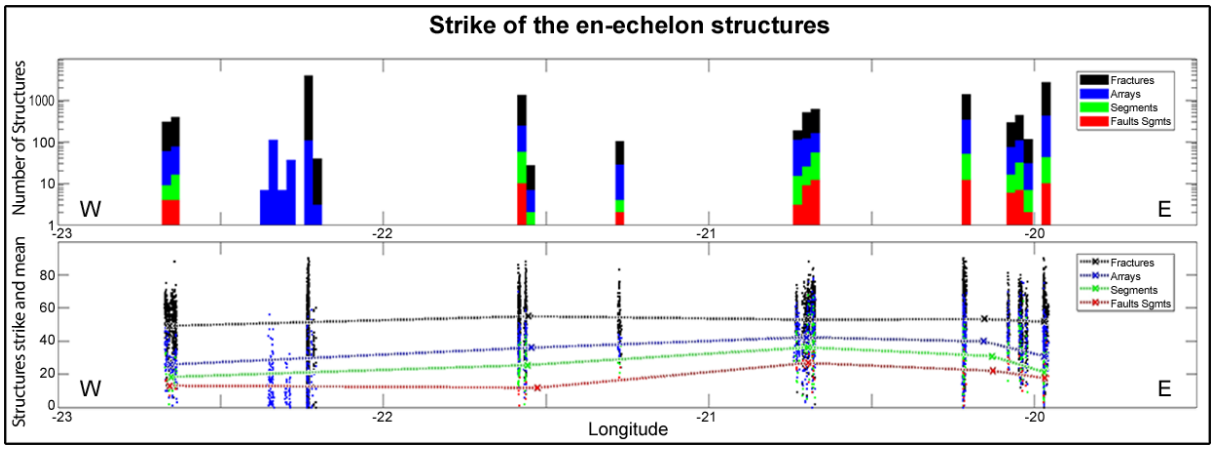

Figure 5.14: Strike of en-echelon structures of NS faults. **A:** Number of structures for every en-echelon scale on a E-W projection. **B:** Structures' strike for every en-echelon scale on a E-W projection.

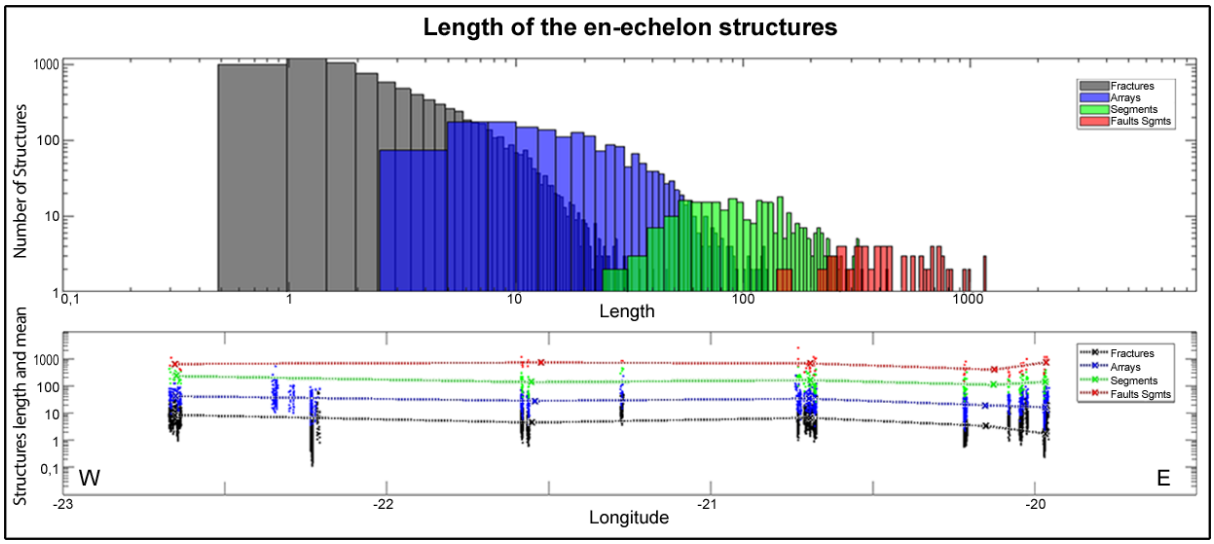

Figure 5.15: Length of en-echelon structures of NS faults. **A:** Structures' length distribution for every en-echelon scale. **B:** Structures' length for every en-echelon scale on a E-W projection.

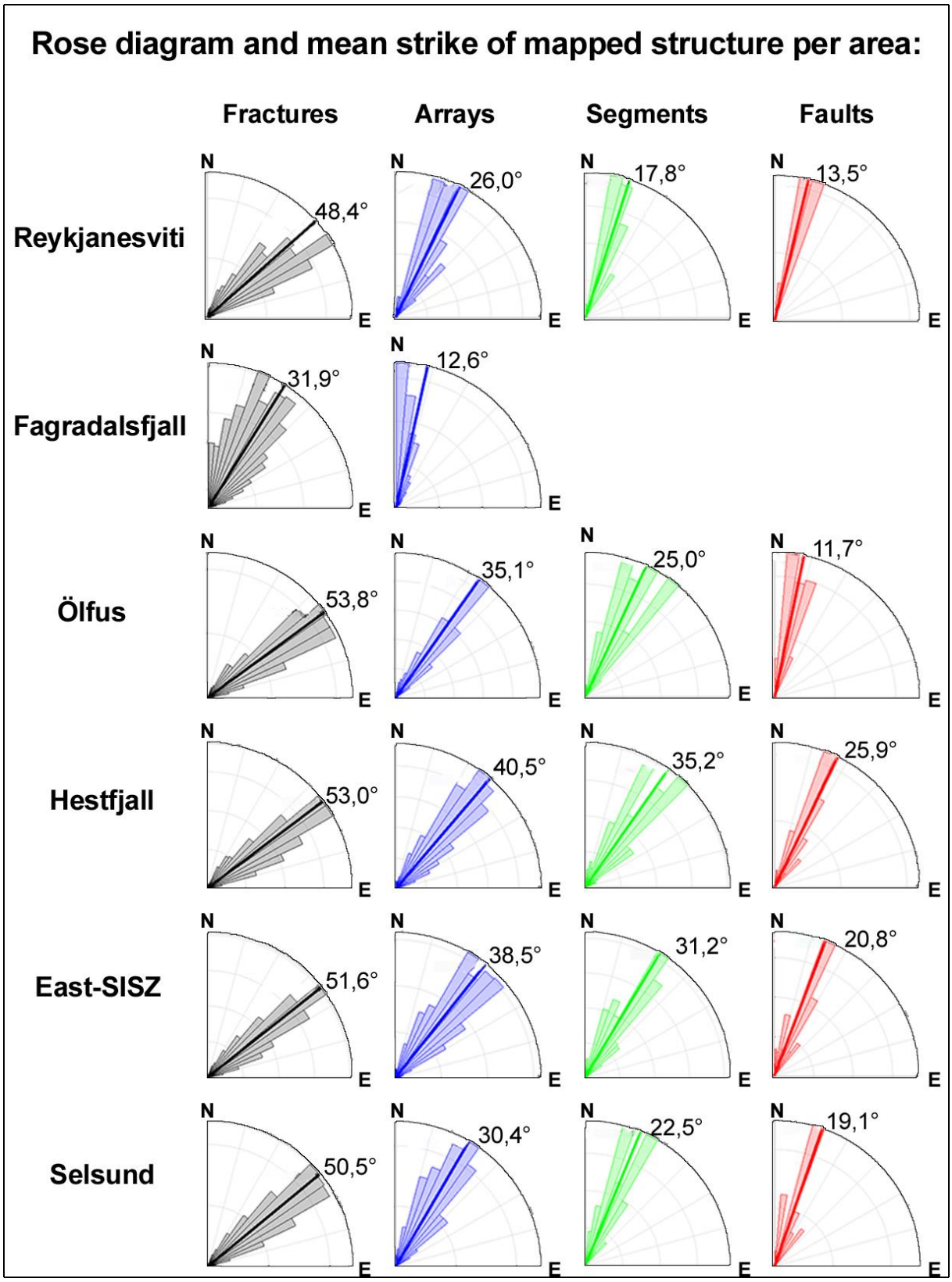

Figure 5.16: Rose diagram of en-echelon structures of NS faults.

5.3 Earthquake catalogue

After merging all earthquake catalogues, the combined dataset spans approximately 128,000 events recorded between 2009 and 2022 in the study area (Figure 5.17 and 38), resulting in an average occurrence of 25 events per day. The recorded earthquake magnitudes range from 0 M_{LW}, representing the minimum measured magnitude as mentioned earlier, to 5.6 M_{LW}. The two highest magnitude events occurred on 20.10.2020 and 24.02.2021. Notably, during this time window, 15 events occurred with a magnitude exceeding 5 M_{LW}.

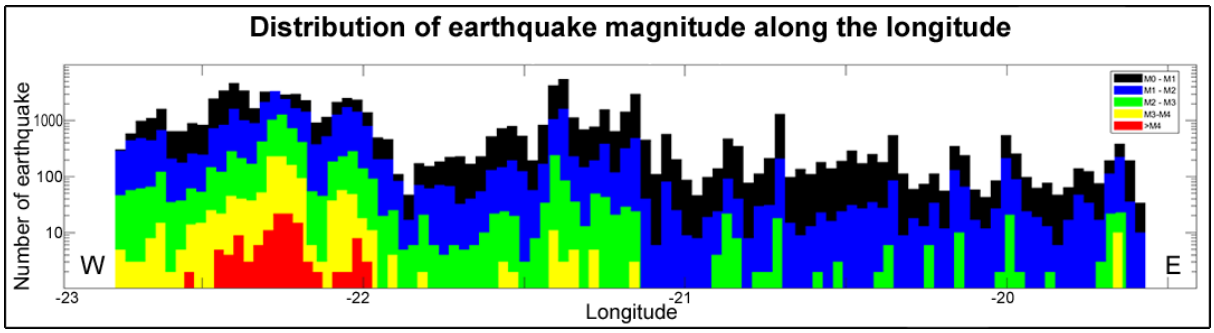

Figure 5.17: Earthquakes histogram on a E-W projection for each different magnitude.

In this region, the majority of earthquakes are shallow, with a depth of less than 5 kilometres. The maximum observed depth in these data is 24 kilometres, associated with a magnitude of nearly 0 M_{LW}. However, 95% of the events occur at depths above 10 kilometres in the east of the monitored region and above 7 kilometres in the west (Figure 5.19). The depth data are graphically represented in relation to the density of events along the longitude, depicted as a heatmap.

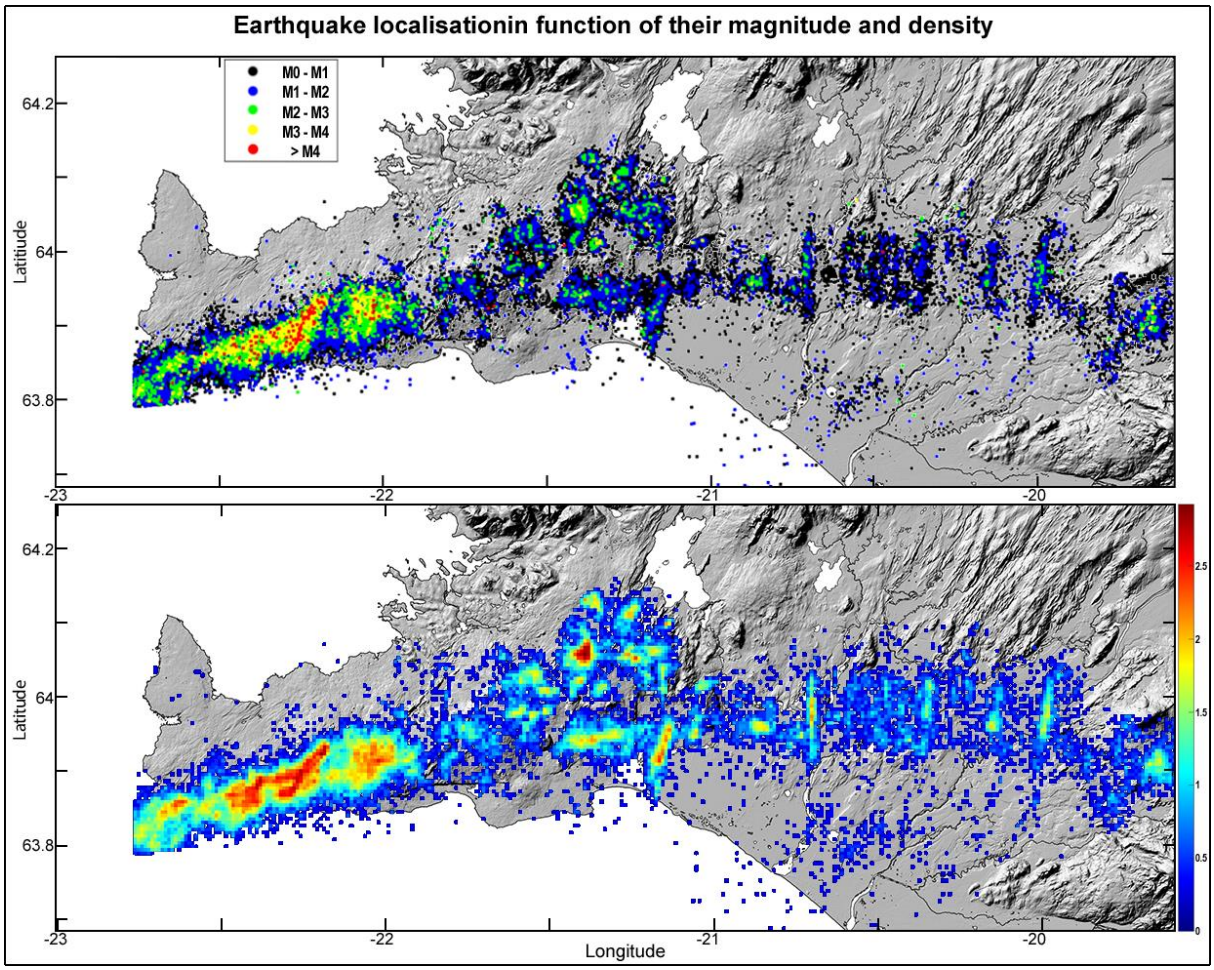

Figure 5.18: Earthquakes' location map. **A:** Earthquakes map in function of their magnitude. **B:** Density map with digits of 500 metres with the colour bar corresponding to the logarithmic number of events occurring in each digit.

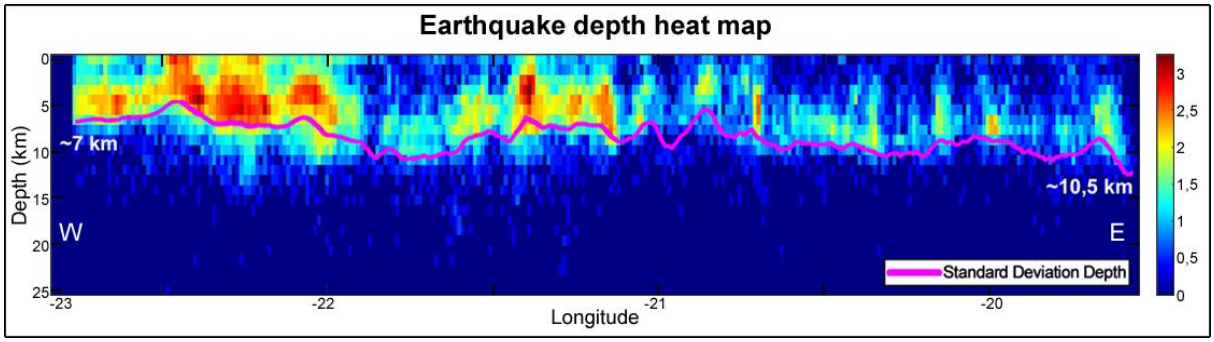

Figure 5.19: Earthquakes' depth along the E-W projection. 95% of the earthquakes occur above the rose line, which is calculated with a moving window of 10. The density map with digits of approximatively 500 metres along longitude a 1000 metre along depth with the colour bar corresponding to the logarithmic number of events occurring in each digit.

Chapter 6

Discussion

6.1 RPOR-SISZ faults

Seismicity distribution from SISZ to RPOR

In SISZ, characterized by minimal pollution from dike intrusions or geothermal power plants, unlike the Reykjanes Peninsula and Hengill volcanic system, we observe that the predominant seismic activity takes place along the major NS faults (Figure 5.18 and 39). Although no large seismic event occurred in our data time range, these NS faults exhibit ongoing inter-seismic activity. The epicentres of this activity are concentrated in the central areas of each fault, hindering the determination of the total rupture length of these NS faults, as discussed earlier.

In RPOR, particularly in its western part, the eruptive episode of 2021 shows a very high concentration of events. The dike emplacement is clearly visible in both the magnitude map, where nearly all events of M_{LW} 4.0 or higher occurred, and the density map, exhibiting a distinct positive anomaly in the number of events that nearly matches the order of magnitude observed in Hengill's power plant (Figure 5.18). This area of

high concentration of events corresponds to co-seismic activity and provides valuable information to determine the total rupture length of fault segments. Additionally, in the Ölfus area, situated between Hengill and Fagradalsfjall, the seismic activity is less pronounced, revealing alignments of NS earthquakes similar to those observed in SISZ.

Evidence of fault reactivations

The results obtained from the aerial mapping of surface structures, combined with a synthesis of historical events of large magnitude, do not exhibit a direct link in the SISZ area. Despite the highest recorded magnitudes in historical times, dating back to the eleventh century and reaching around M7, with the maximum observed displacement for these events at the surface fault trace being only 1 to 2 meters (Angelier et al., 2008). The remaining displacement required to account for the total movement is distributed within a deformation area (Einarsson, 2010). However, throughout the SISZ, there are observed push-ups that reach heights of up to several meters, displaying various shapes such as round or elongated, with lengths that can extend to nearly 100 meters, as seen in Vindáls (Figure 5.10). These sizes, directly correlated to the shortening range, are orders of magnitude larger than the displacement associated with a single seismic event and strongly suggest that these faults have been reactivated several times in the past.

Moreover, the size of push-ups along the same fault exhibits significant variability, ranging from tens of centimetres to meters. Such variation is inconsistent with a single fault activation, as it would imply a high variability in the displacement rate of several orders of magnitude for a single event. Alternatively, this large spatial variability may be associated with distinct events along the same fault. The differences in size could

be attributed to multiple reactivations for the larger push-ups, while the smaller ones may have been active only once.

In Selsund (Figure 5.11), remnants of pre-event features are still visible in the landscape, notably seen in sheep paths. The considerable sheep activity in the southern part of the fault has resulted in distinct walk paths that intersect the fault line. One such path intersects the fault in an area with substantial topographic differences, constraining all the sheep to cross the same passage. This provided an estimate of the displacement along the fault of approximately 1.7 meters (Figure 6.1). However, on this sheep path, evidence suggests multiple fault reactivations with three or four distinct instances showing displacements ranging from 1.5 to 2.5 meters. These observations serve as direct evidence of fault reactivation in the SISZ. Additionally, the two earthquakes occurring in 2000 within the SISZ took place on pre-existing faults, indicating further instances of fault reactivation (Einarsson, 2010).

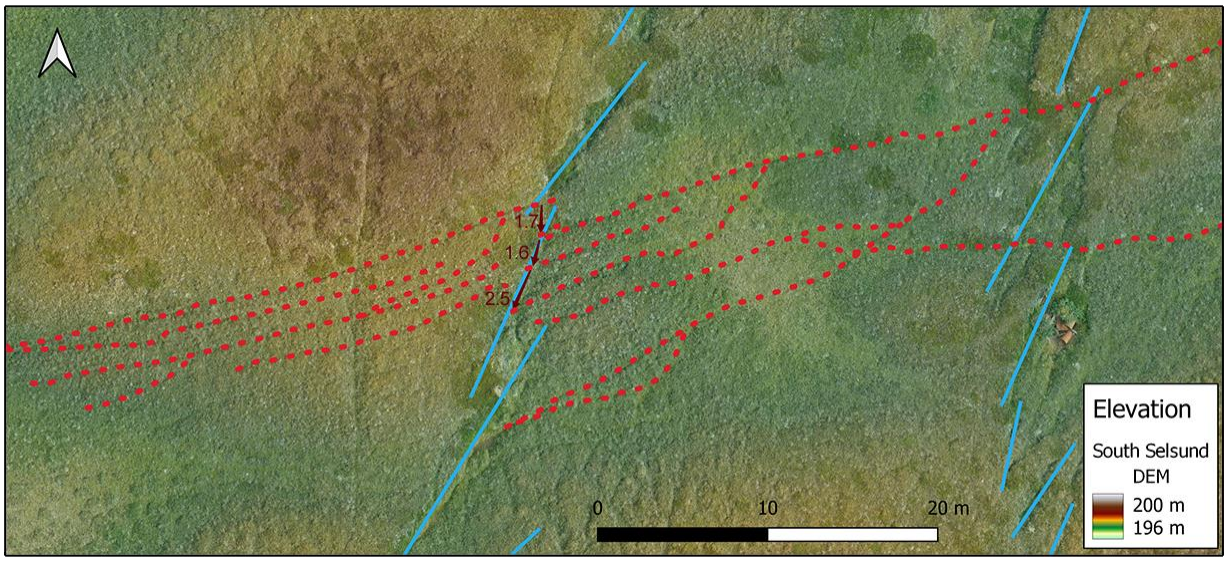

Figure 6.1: Sheep path displacement in south Selsund. Blue lines are the mapped NS en-echelon arrays, Red dotted lines are the sheep paths that cross the faults. There is an offset and a potential multiple activation of the fault as on the west side the only well marked path is the upper one, unlike those to the east of the faults, where multiple paths are well visible. The numbers are the distance of the multiple displacements of the path in metres. The 2.5 metres displacement could also be linked to the lower west path (the only one that does not merge with the upper one) but we linked it with the upper one as it is a lot more developed than the lower west.

In the Reykjanes Peninsula, several significant earthquakes, with a magnitude around 5, occurred within our analysed time frame. These events are all associated with the 2020-2021 intrusion and eruption event of Fagradalsfjall, but they all originated from pre-existing NS faults (Bufféral et al., 2023; Einarsson et al., 2023; Hjartardóttir et al., 2023). Fresh surface fractures resulting from these events were also collected and mapped by Elisabetta Panza in this project. However, these data, in addition to being mapped by a different person than the present study, were collected shortly after the earthquake events. Since then, many temporal structures and surface ruptures that have been mapped have since disappeared. These two differences account for the high heterogeneity observed in this zone compared to the other areas of the study.

In both covered regions, we have observed that nearly all recent seismic events occurred along pre-existing NS faults. However, our results indicate that these strike-slip events also reactivate other pre-existing structures, such as normal faults associated with rifting activity. Rifting structures in the form of normal faults have been mapped in three zones: at Reykjanesviti and West-Ölfus (see Fig. 16 for location), where deformation is still ongoing, and at the south of Hestfjall in central SISZ, where these normal faults likely originated from old WVZ activity.

This reactivation is primarily observed in Ölfus and Hestfjall, where NS faults intersect pre-existing rifting structures. Interestingly, we identify that the segment and fault strike and length, although recently reactivated in strike-slip motion, such as south of Hestfjall, are not coherent with their non-normal counterparts. Conversely, the strike and length of fractures and arrays are identical to their en-echelon counterparts outside of these normal fault areas (Figure 6.2). These similarities in the smaller en-echelon structures could be indicative of the reactivation of these non-NS faults by the NS strike-slips. As ultimately all the en-echelon scales are oriented between the main fault

movement of NS and these older NE-SW rift structures, and since this rifting activity is the source of all the Icelandic crust, it may be the origin of the en-echelon organization of the NS fault.

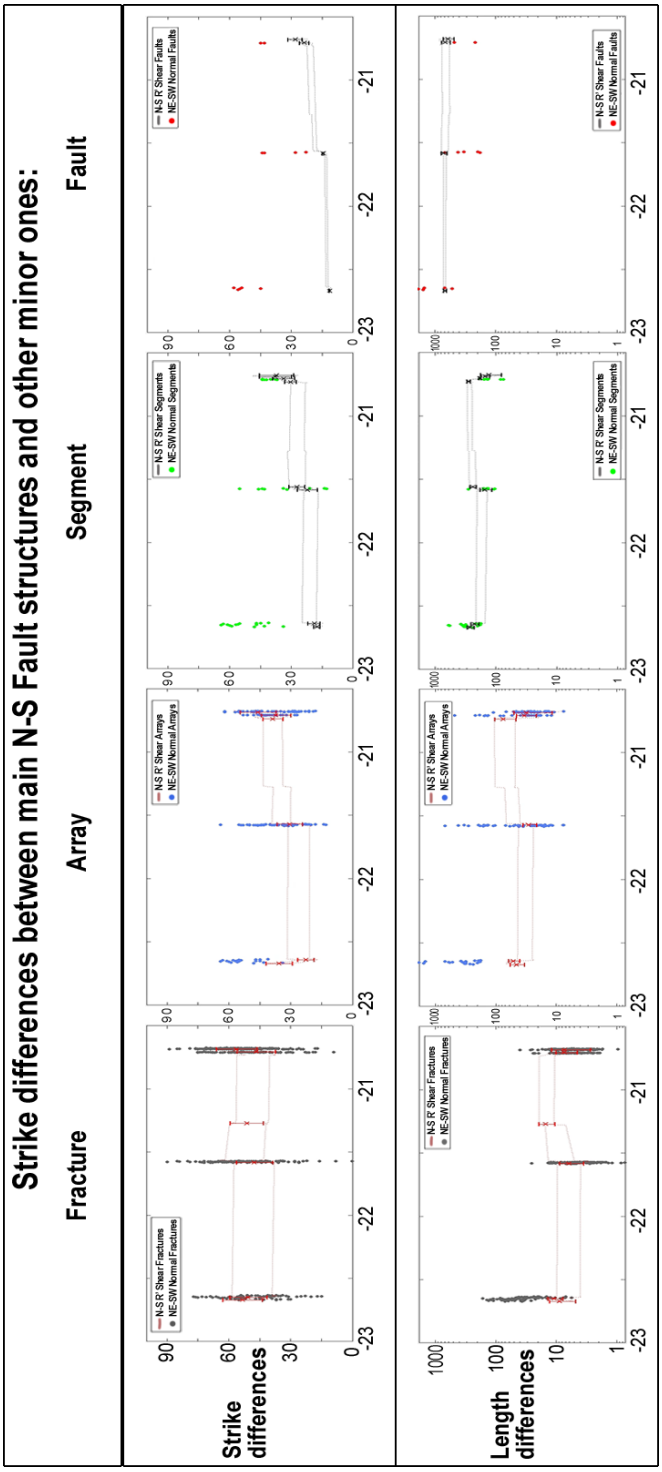

Figure 6.2: Reactivation of the NE-SW normal faults structures in the NS shear faults context. The standard deviations lines are the NS faults, and the point are the preexisting normal faults. In the larger en-echelon size, the correlation between the two datasets is low (mainly in strike) but for the fractures and arrays size they are very similar, which induce that the smaller en-echelon size could be more recent and linked to a reactivation along the old normal faults' orientation.

Distribution of fault lengths

The length analysis derived from the aerial mapping results does not yield consistent or usable information. Across all en-echelon sizes and in each zone, the results do not exhibit a clear consistency, with a heterogeneous distribution of the fault length (Figure 6.3). Although there is a general similarity in the W-E studied projection, a chaotic disparity persists. It appears that the results are more influenced by the type of soil and its roughness rather than other factors. Therefore, considering the high soil heterogeneity in large areas, the length parameter is deemed unsuitable for studying similarities among faults using aerial photography and will be excluded from further discussion.

Contrary to the varied lengths observed in individual en-echelon fractures, the fault plane length exhibits a distinct trend along the E-W axis (Figure 3.9). Despite a notable uncertainty owing to its subsurface nature, a consistent and gradual decrease is noticeable in a westerly direction, with no well-defined limit observed at the Hengill triple-point. The mean lateral spacing of these NS faults remains relatively consistent, ranging between 2 and 3 kilometres. In the Reykjanes region, up to Hengill, the spacing hovers around 2 kilometres before gradually increasing to ~3 kilometres eastwards in the SISZ (Figure 5.13). This trend could be attributed to the thicker soil in east SISZ, potentially concealing some NS faults and resulting in two main groups of spacing, one around 2 kilometres and the other approximately 4 kilometres. The second main hypothesis related to this trend will be further elaborated below.

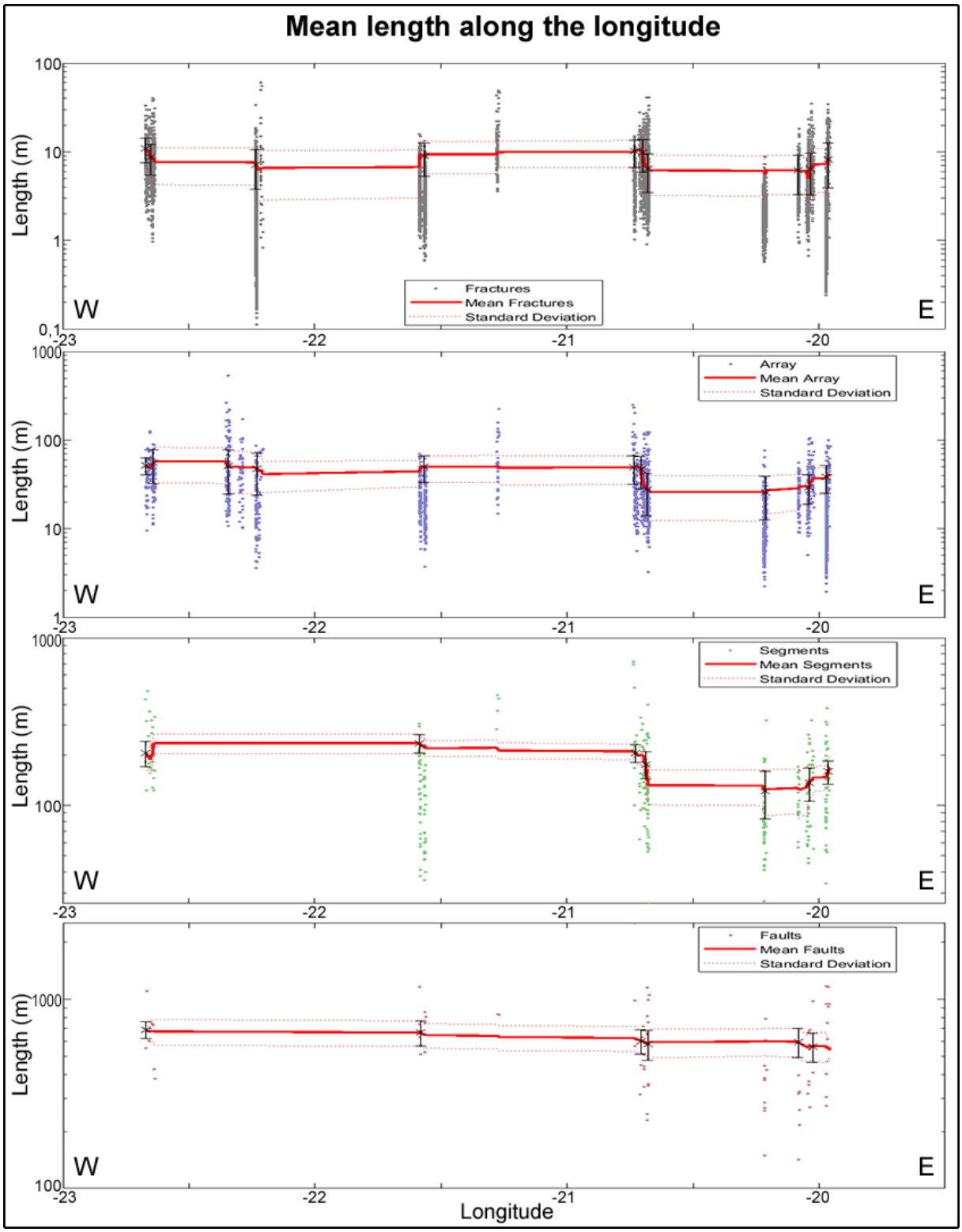

Figure 6.3: Length evolution of the en-echelon structures along the E-W projection. The length local mean, which is obtained by a moving window of 50, is not corelated of the E-W projection. In general, the lengths are a little bit shorter in the east because the soil is softer there.

Distribution of fault strikes

Regarding the strike, the mapping results of the en-echelon structures exhibit greater consistency compared to the length measurements (Figure 6.4). All en-echelon scales show a consistent trend characterized by a clear bend of the structure's orientation to the north westward. This bending is continuous and remains nearly constant along the entire 160 kilometres, with no distinct delineation observed between the two regions.

The presence of the same fault family in two different systems, coupled with the absence of a significant strike dissimilarity between RPOR and SISZ, along with their continuity, suggests a certain connection. This implies that they may not be as distinct as previously believed.

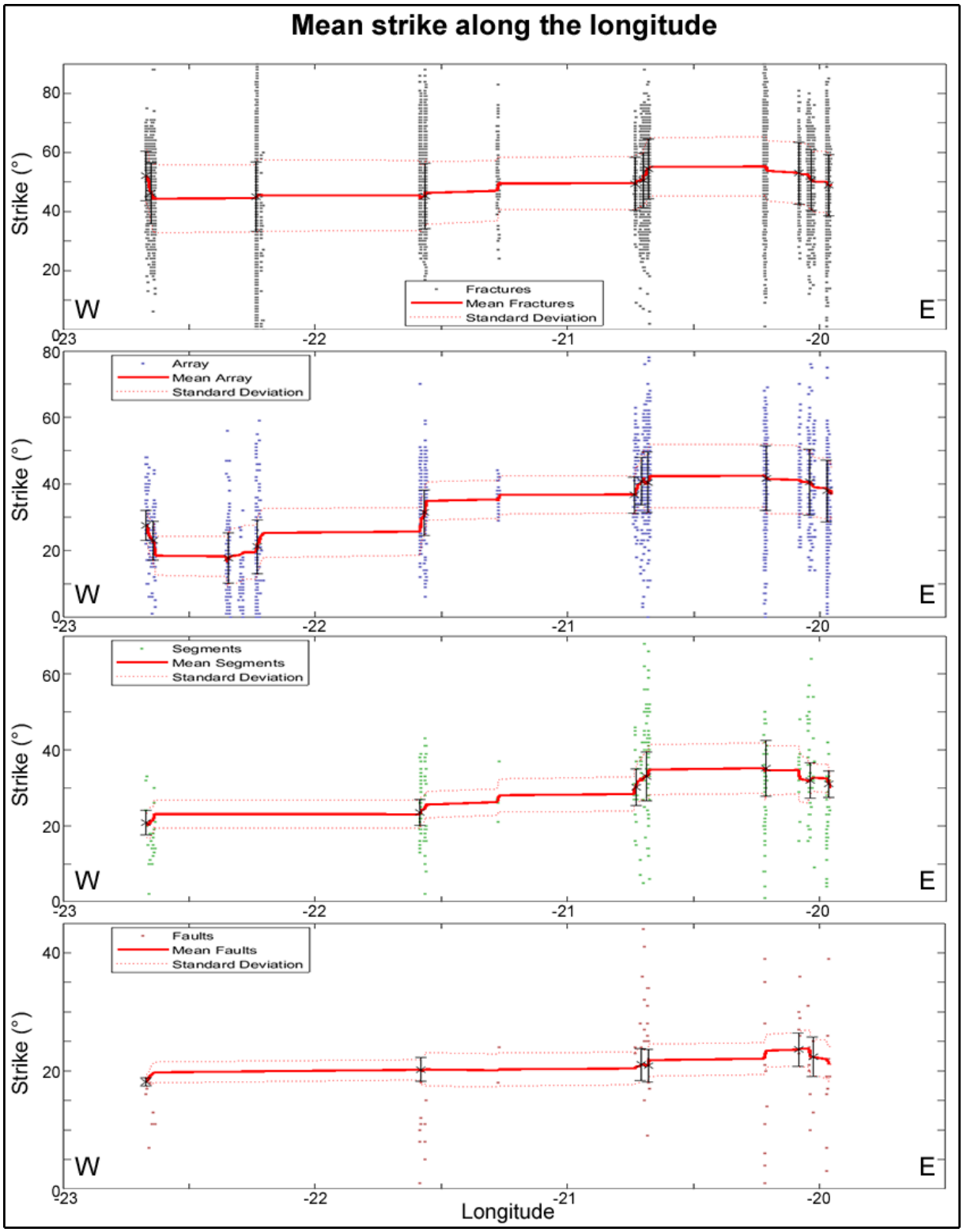

Figure 6.4: Strike evolution of the en-echelon structures along the E-W projection. The strike local mean, which is obtained by a moving window of 50, is well corelated of the E-W projection with a constant trend to be more oriented toward north to the west for all en-echelon size. This tend is also continue between SISZ and RPOR.

6.2 Differences between RPOR and SISZ

Limit between RPOR and SISZ at Hengill triple-point

The outcomes derived from the aerial mapping of the NS fault, as mentioned earlier, align with a gradual stress change along the longitude, suggesting no distinct disparity between the Reykjanes Peninsula Oblique Rift (RPOR) and the South Iceland Seismic Zone (SISZ). As these faults predominantly accommodate shearing in both RPOR and SISZ. It can be inferred that this NS fault family either overlaps the two distinct systems or serves as a connecting link between them. The primary observable distinction lies in the presence of crustal accretion, originating in the volcanic systems of the peninsula to the west of the Hengill triple-point.

The distinction between two clearly defined systems is accentuated by the presence of the Hengill volcanic system at their delineated boundary. The activity in Hengill introduces a significant contrast along the E-W axis, as it is also connected to the West Volcanic Zone (WVZ), serving as a focal point for much of its contemporary activity. Consequently, the Hengill triple-point highlights the differentiation between RPOR and SISZ, influenced not only by the dynamic rifting zone but also by its connexion with the dying rift of the WVZ.

There exists a substantial age disparity between the two regions, with SISZ being more than three times younger than RPOR (Sigmundsson et al., 2020b). This age difference is attributed to the occurrence of two consecutive rift jumps eastward, each corresponding to one of the regions and separated by approximately 5 million years as mentioned before.

Rotation of the plate boundary

The second prominent difference observed between the two regions is the bending of the plate boundary across the entire studied area. This boundary is oriented approximately at N90° in all of SISZ before gradually shifting westward along RPOR, reaching around N65° at the Reykjanes Ridge contact (Bufféral et al., 2023; Khodayar et al., 2018; Sigmundsson et al., 2022). Consequently, SISZ exhibits an extension oriented at 14° to the plate spreading direction, while RPOR ranges from 25° to 39°. Despite this bending of the plate boundary, the total regional stress remains consistent across the entire studied area, being driven by the plate spreading movement. However, this implies a change in the direction of local shear and tensional stresses, where shear stress remains along the plate border, and tensional stress remains perpendicular to it. As the tensional component of the total stress increases toward the west, volcanic activity appears to follow a similar pattern, with the most developed fissure swarms observed, apart from the exception of Hengill.

In SISZ, the orientation remains nearly constant and aligned with pure shear, contrasting with RPOR, where the orientation gradually bends westwards, indicating an increase in tensional shear. This extension is correlated with rifting processes and the presence of the volcanic system, highlighting a connection between plate border bending and volcanic activity.

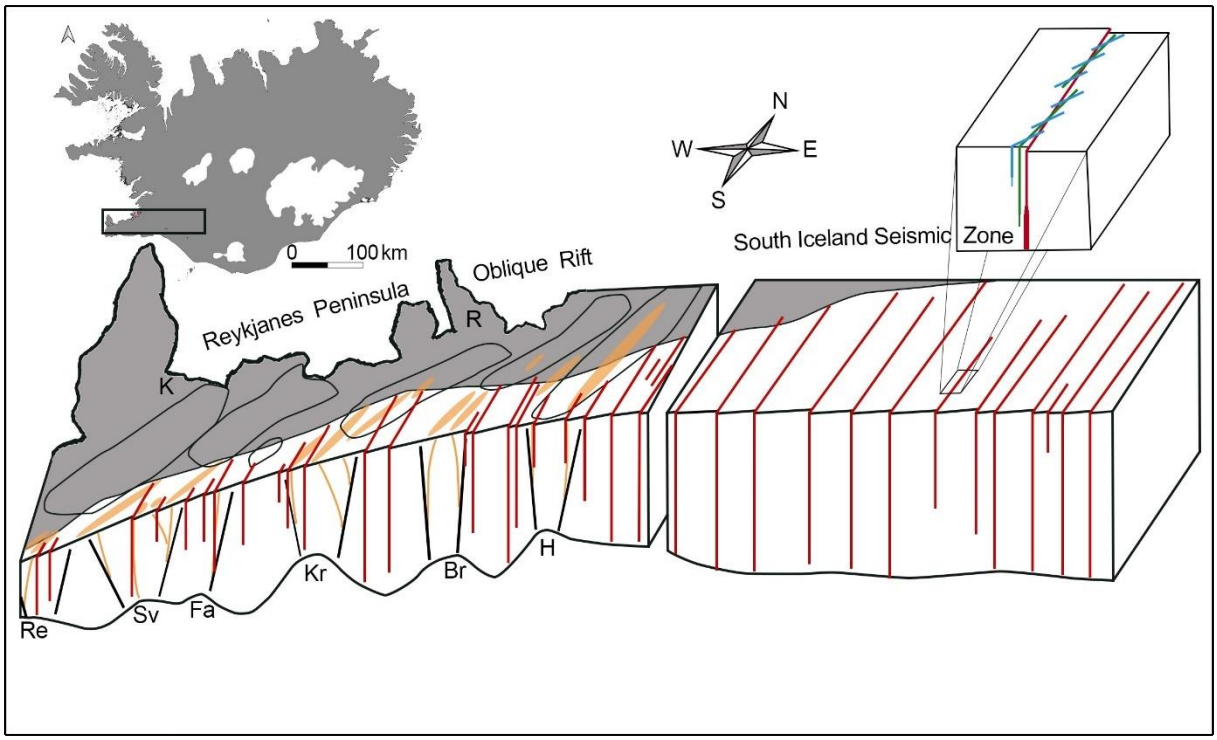

Figure 6.5: A: 3D-Block diagram of main structural features and with the regional stress in southwest Iceland. Only the northern half of the plates boundary's width area is shown. The blue lines are the NS faults, the red ones are fissure swarms of the RPOR volcanic systems, and the grey zone is the North American plate (and the Hreppar microplate) uniform area. The volcanic systems are RE for Reykjanes, SV for Svartsengi, FA for Fagradalsfjall, KR for Krýsuvík, BR for Brennisteinsfjöll, and H for Hengill. **B:** 3D block diagram zoom on an en-echelon section of a NS fault.

Therefore, the two main observable differences between the two regions are ultimately intertwined, as volcanic activity emerges as a secondary characteristic of the plate boundary bending. Additionally, in these conditions, the limit angle, between extension of the plates limit and the plate spreading direction, allowing crust creation ranges between 15° and 25°, situated between the angles observed in SISZ and RPOR.

6.3 East-west disparity

Earthquakes depth distribution and its origin

While the primary source of differences between the two regions has been outlined above, there are still unexplained disparities along the E-W segment from RPOR to SISZ. Einarsson et al. (1981) noted that the highest magnitude events of 7.0 occur in the east of SISZ, followed by a consistent magnitude decrease westward, reaching a maximum magnitude of 5.6 in the west Reykjanes Peninsula, occurring during the 2021 eruption crisis. This magnitude decrease toward West can be logically linked to a decrease in fault plane surface (Figure 6.7).

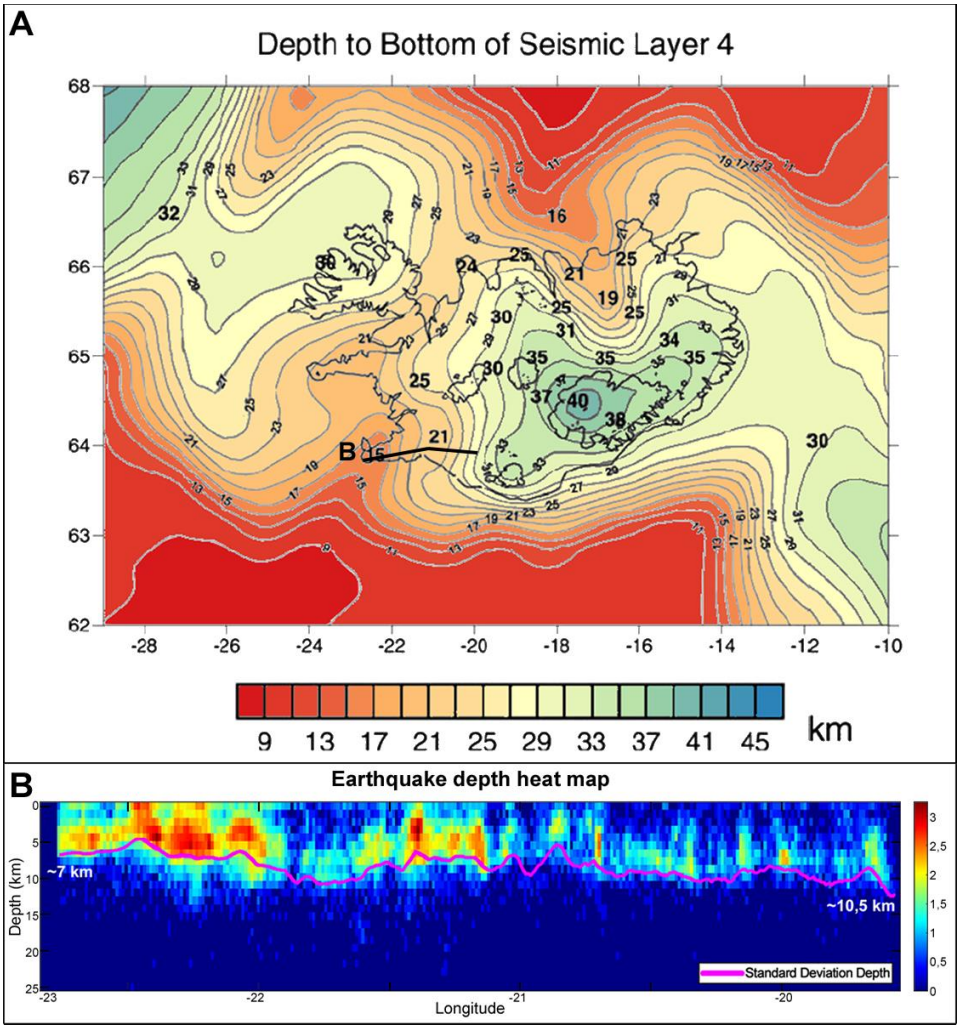

Figure 6.6: A: Moho depth map under Iceland. Earthquakes maximum depth and geothermal gradient are coherent with the crust thickness. Modified from Kaban et al., 2002. **B:** Earthquake occurrence cross section along studied area that correlate with A.

The first of the two plane parameters is the maximum depth of these faults. This depth is determined by the limit between brittle rock and their underlying ductile counterpart, known as the locking depth. The results indicate a decrease in maximum depth from 10 kilometres in the east to 7 kilometres in the west (Figure 6.6 B), which aligns with the locking depth calculated by Árnadóttir et al. in 2006. Apart from rock composition (oceanic crust, which spreads uniformly across Iceland), the geothermal gradient, higher in areas of crustal accretion and near volcanic zones (Kaban et al., 2002; Figure 6.6 A), further supports this observation and is consistent with the location of geothermal power plants.

As previously discussed, the second surface plane parameter, which is the NS fault length (Figure 3.9), also exhibits a constant decrease westward and this parameter comes with a high degree of uncertainty, so the information presented here is compiled from various sources (A. E. Clifton & Kattenhorn, 2006b; Einarsson, 2008, 2010; Einarsson et al., 1981; Karson et al., 2019). This parameter determines the width of the deformation area affected by the rock's mechanical properties, primarily its strength. As highlighted earlier, Iceland's basalt composition is generally similar across regions. Therefore, the primary controlling factor is heat, with hotter rocks being more ductile and able to accommodate deformation in a narrower area.

En-echelon strike disparity and its origin

The observed disparity in the en-echelon strikes, as revealed by the results, remains well-constrained (Figure 6.4). In the western regions, their strike tends to align more closely with the underlying NS fault. This alignment can be influenced by various factors related to the faulting process and stress conditions within the Earth's crust. Some of the key parameters include rock properties, stress anisotropy, and, as

discussed earlier, these parameters remain consistent across the studied area. Another significant factor is the influence of pre-existing features such as rifts, but as demonstrated, these features exhibit similarities throughout southwest Iceland. The last two major parameters are rock ductility and strain orientation.

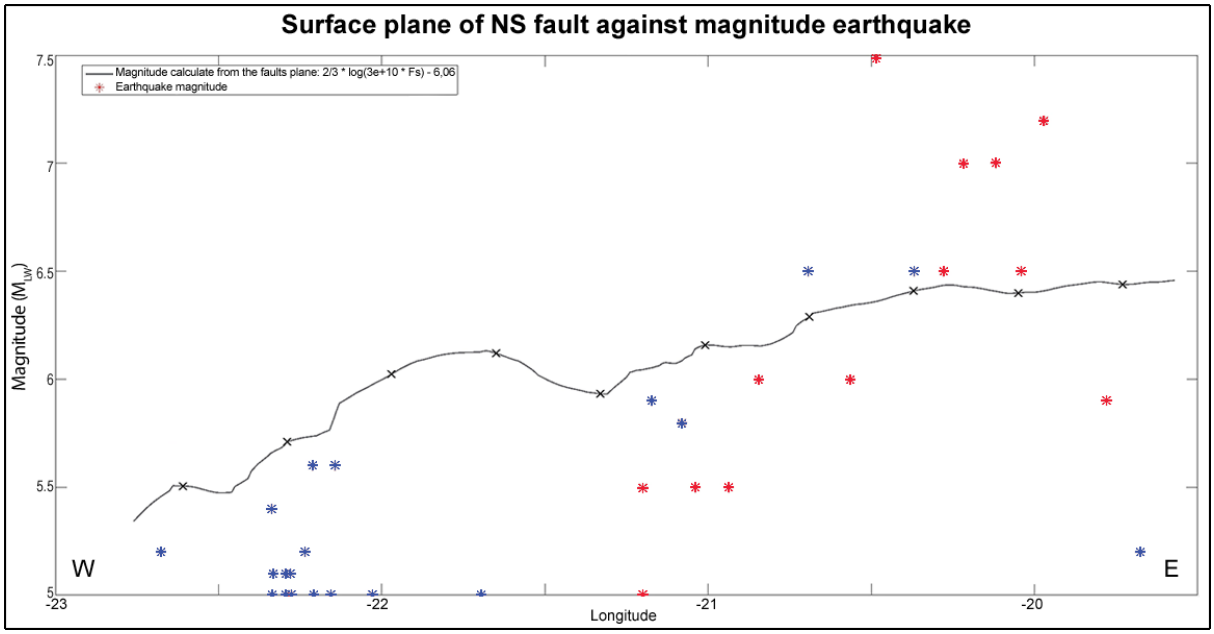

Figure 6.7: Surface of NS fault planes against earthquake magnitude. The black line is a local mean of the surface plane, obtained from the local maximum depth shown in figure 5.19 (with a moving windows of 20) and the fault total length of the NS fault shown in appendix XX(with a moving windows of 10), and transform in magnitude for a displacement of 1 metres with this equation 2/3 * log(3e+10 * Surface Plane * 1) – 6,06. Then the red stars are the historical large earthquakes which happened before 1950 and the blue stars are the recent events that happened after 1950. All recent events are not situated above the fault plane calculated magnitude, unlike some historic event, which could be explained by the different size of the time windows, an historical overestimation, or the fault plane could be underestimated for this event.

The rock ductility can offer an explanation, as it is linked to the geothermal gradient, as discussed earlier. This induced continuous deformation could lead to the en-echelon structures aligning more closely with the orientation of the underlying fault. However, higher ductility may also increase the potential for rock deformation.

The orientation of strain. As discussed earlier, there is a difference in regional shear from east to west, impacting the en-echelon strike, while the NS faults remain consistently oriented. Consequently, the en-echelon structures are likely to adjust to accommodate the changes in shearing associated with the dextral fault system. The

tendency would be for the structures to rotate in the same direction as the shearing rotation, which, in this case, would be towards the north as observed. However, this explanation alone may not be sufficient. Indeed, as discussed earlier, the shear direction remains constant along SISZ, contrary to the trend in strike, suggesting that other factors may contribute to the observed disparity.

In conclusion, determining which aspect of ductility has a more prominent impact on the strike difference is challenging, and it is possible that both parameters contribute to the observed trend, either individually or in combination. Additionally, there may be other influencing factors not covered in this discussion. Explaining the cause of this trend with primarily aerial mapping data remains difficult. To investigate deeper into this question, it would be beneficial to integrate the development of a numerical or analogue model with a new comprehensive field mapping campaign. This approach could provide better constraints on the causes of the observed en-echelon strike trend.

Chapter 7

Conclusion and perspectives

The objective of this project was to investigate the mechanisms of a highly oblique rift, aiming to understand the transition into a leaky or a tectonic transform zone within a subaerial section of a mid-oceanic ridge. A comprehensive analysis of this extensive area was primarily conducted through aerial mapping using QGIS, leveraging drone photogrammetry obtained with a Wingtra drone, a highly effective method for analysing and sampling large areas, especially in regions where vegetation allows for optical data collection. To maximize the sampling of NS strike-slip faults, which are present in both leaky and tectonic areas in southwest Iceland, we meticulously mapped and analysed length and strike data derived from tens of thousands of images to map 19’500 structures. This manually mapped dataset was a very time consuming method, but it holds the potential for exploring the training of artificial intelligence models for future surface fault mapping project.

Our findings indicate that the presence of pre-existing structures may provide an explanation for the well-developed en-echelon of the NS faults. These strike-slip faults revealed no observable differences in NS faults between the two types of highly oblique

plate spreading but rather a continuous trend on various parameter, and no distinct boundaries were identified between these adjacent systems.

We integrated earthquake data spanning from 2009 to 2022, which predominantly reactivate pre-existing faults, emphasizing the importance of understanding the geological history of the region, correlating them with our mapped data to enhance information and depth extensions of the NS faults. Yet, no clear demarcations between the two types of highly oblique plate spreading emerged.

Several parameters, including the NS fault length, earthquake depth, and magnitude, exhibit a consistent disparity throughout the studied area. We propose that this disparity is primarily driven by the crustal thermal gradient, which increases in the westward direction where the presence of volcanism is dominant. Furthermore, we propose that the E-W evolution of the geothermal gradient is influenced by the rotation of the plate limit. This orientation of the plate border concerning the spreading direction emerged as a critical parameter for the development of a leaky or tectonic transform zone from an oblique rift. The limit angle for this transition was found to be between 15° and 25°, with lesser tectonic characteristics and greater leaky characteristics.

However, a distinctive trend lacking a strong correlation with other parameters is the north bending westward of en-echelon strikes. No measured parameters seem to explain this difference, and it could possibly originate from the maturity of the system. Similar to the Riedel shear system, the fractures may shift to become more parallel to the main shear plane underneath with its development.

In addition, the relative juvenility of SISZ makes its evolution still ongoing. In general, it is related to the Tjörnes seismic zone, but we also explore the similarities and

connections between SISZ and RPOR, suggesting that they may function, at least partially, as a unified system, which could potentially develop itself into an oblique rift.

A

Appendices

GIS mapping

A1.1.

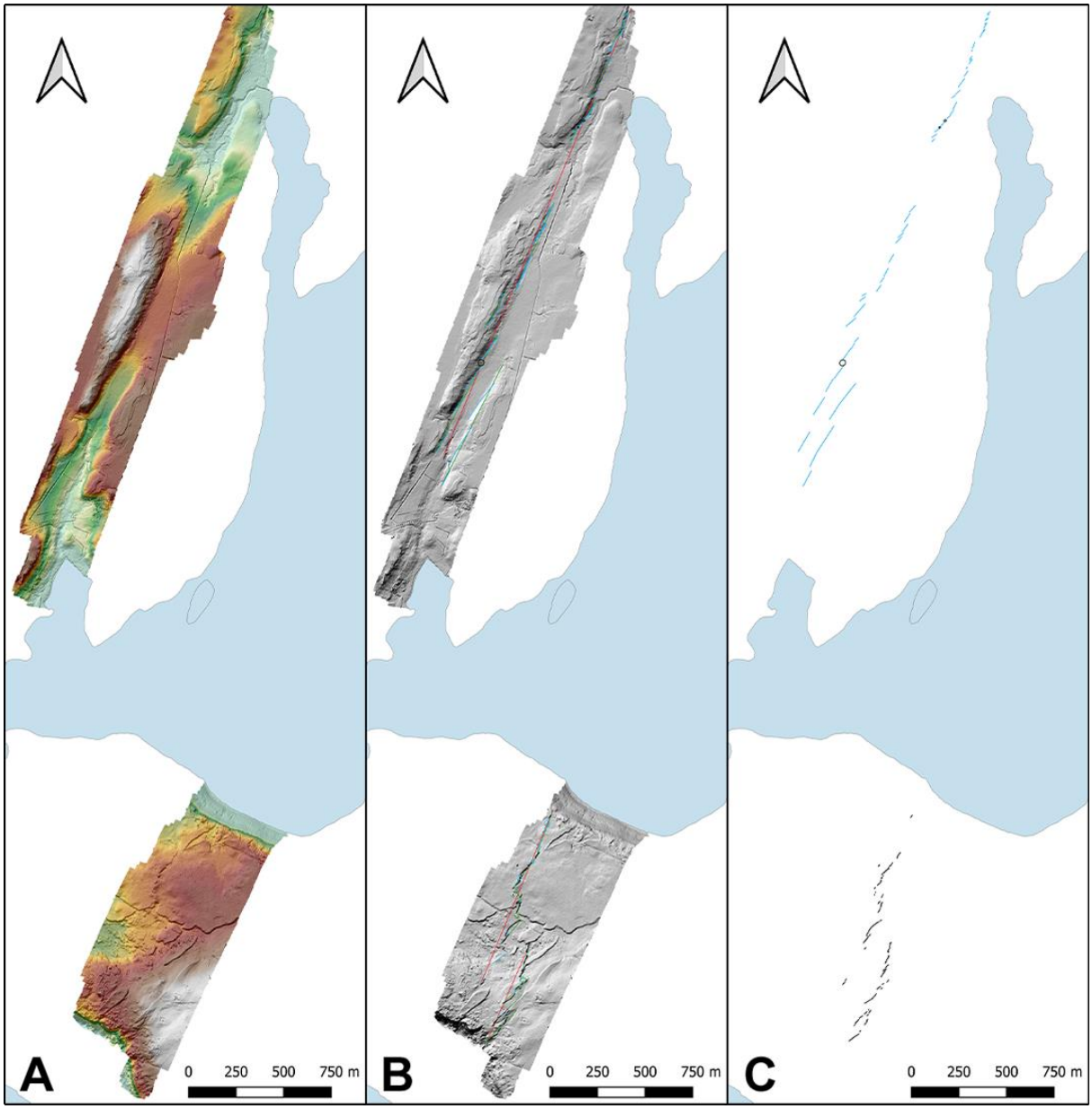

Appendix 1.1. Mapping results of the west-Hestfjall area. **A:** Raw DEM obtained by drone pictures. **B:** En-echelon fractures' size only map. **C:** En-echelon larger size (arrays in blue, segments in green, and faults in red) on a shaded relief map.

A1.2.

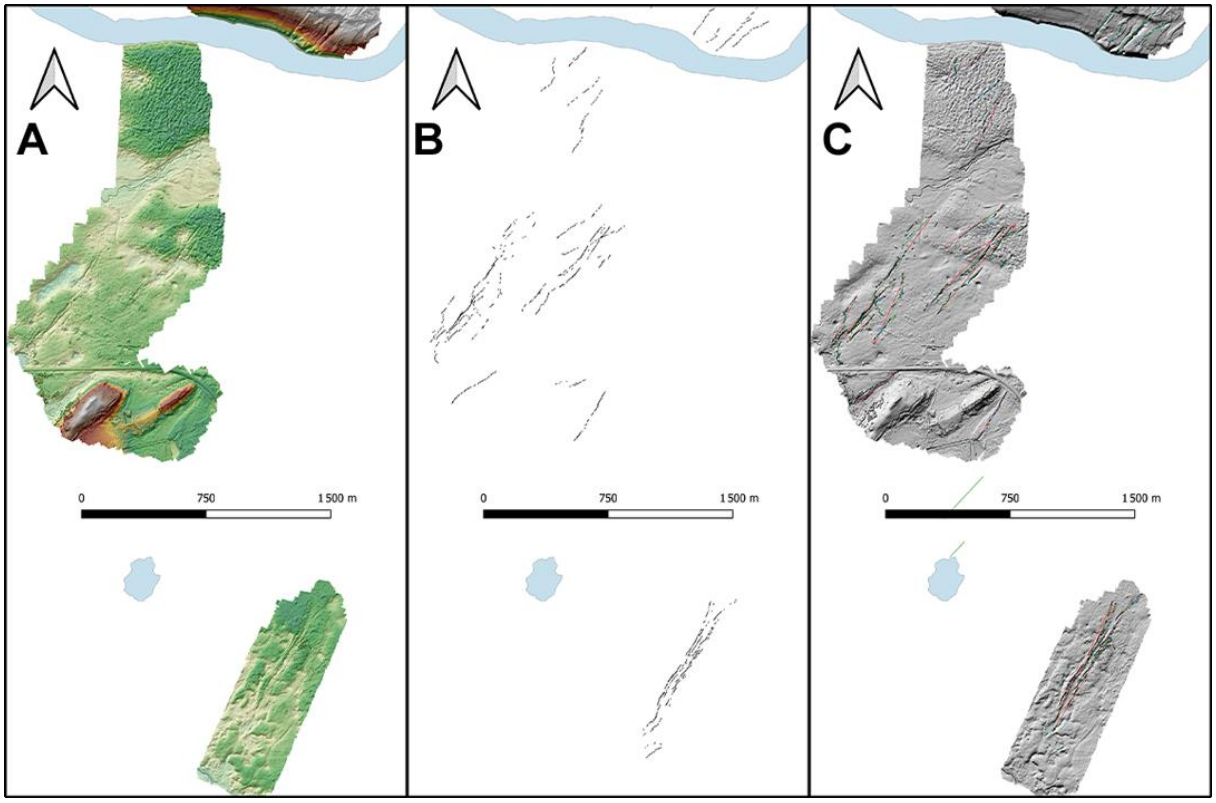

Appendix 1.2. Mapping results of the south-Hestfjall area. **A:** Raw DEM obtained by drone pictures. **B:** En-echelon fractures' size only map. **C:** En-echelon larger size (arrays in blue, segments in green, and faults in red) on a shaded relief map.

A1.3.

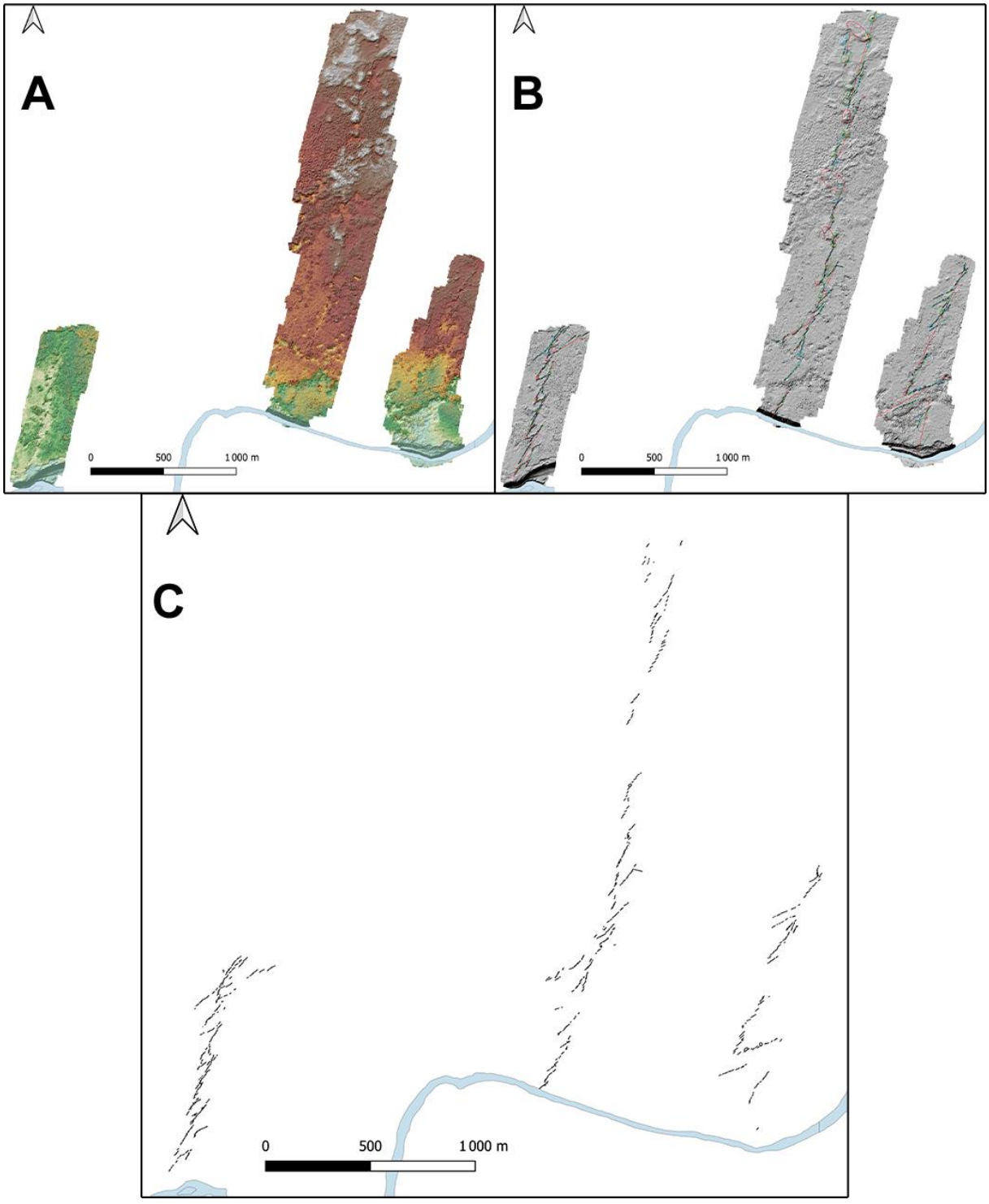

Appendix 1.3. Mapping results of the East-SISZ area. **A:** Raw DEM obtained by drone pictures. **B:** En-echelon fractures' size only map. **C:** En-echelon larger size (arrays in blue, segments in green, and faults in red) on a shaded relief map.

A1.4.

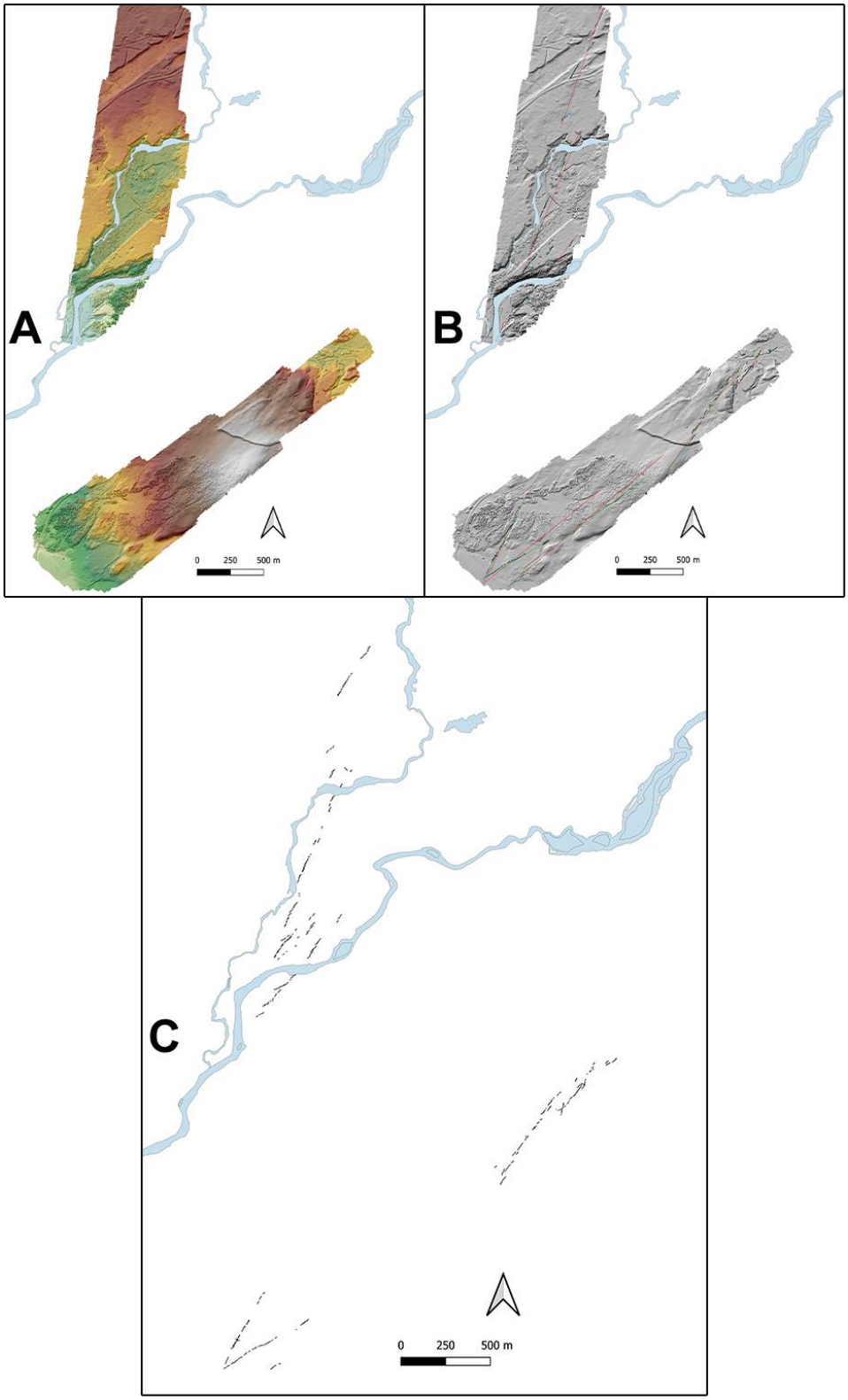

Appendix 1.4. Mapping results of the north-Selsund area. **A:** Raw DEM obtained by drone pictures. **B:** En-echelon fractures' size only map. **C:** En-echelon larger size (arrays in blue, segments in green, and faults in red) on a shaded relief map.

A1.5.

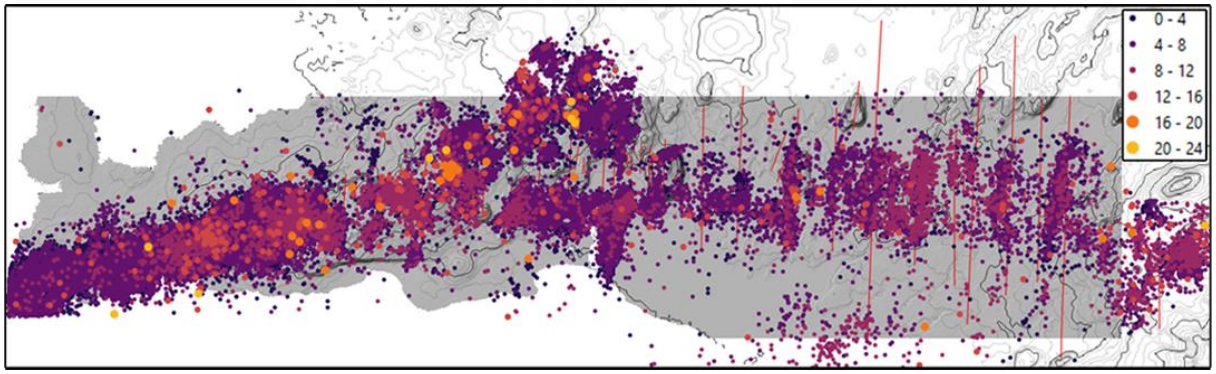

Appendix 1.5. Earthquakes depth map (in kilometres)

A1.6.

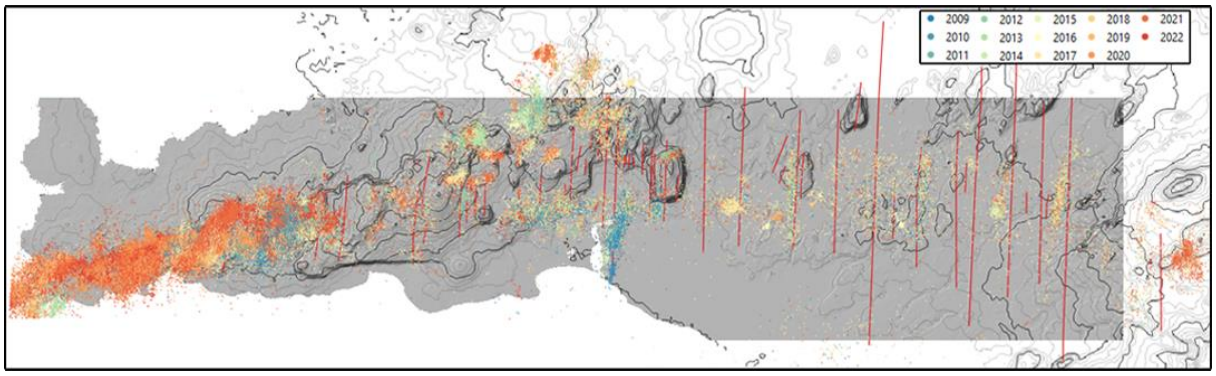

Appendix 1.6. Earthquakes discriminate by their happening year map

A1.7a.

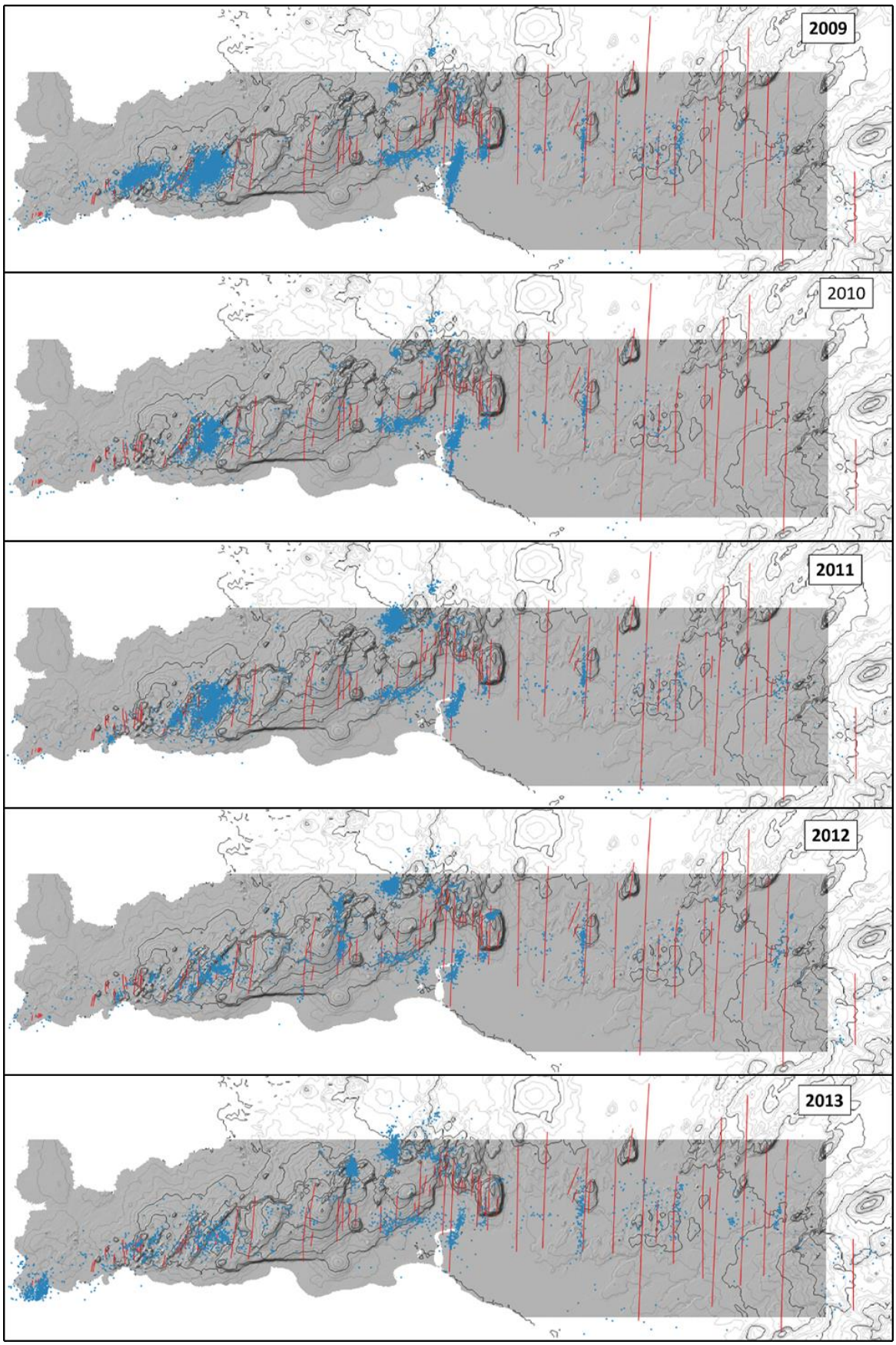

A1.7b

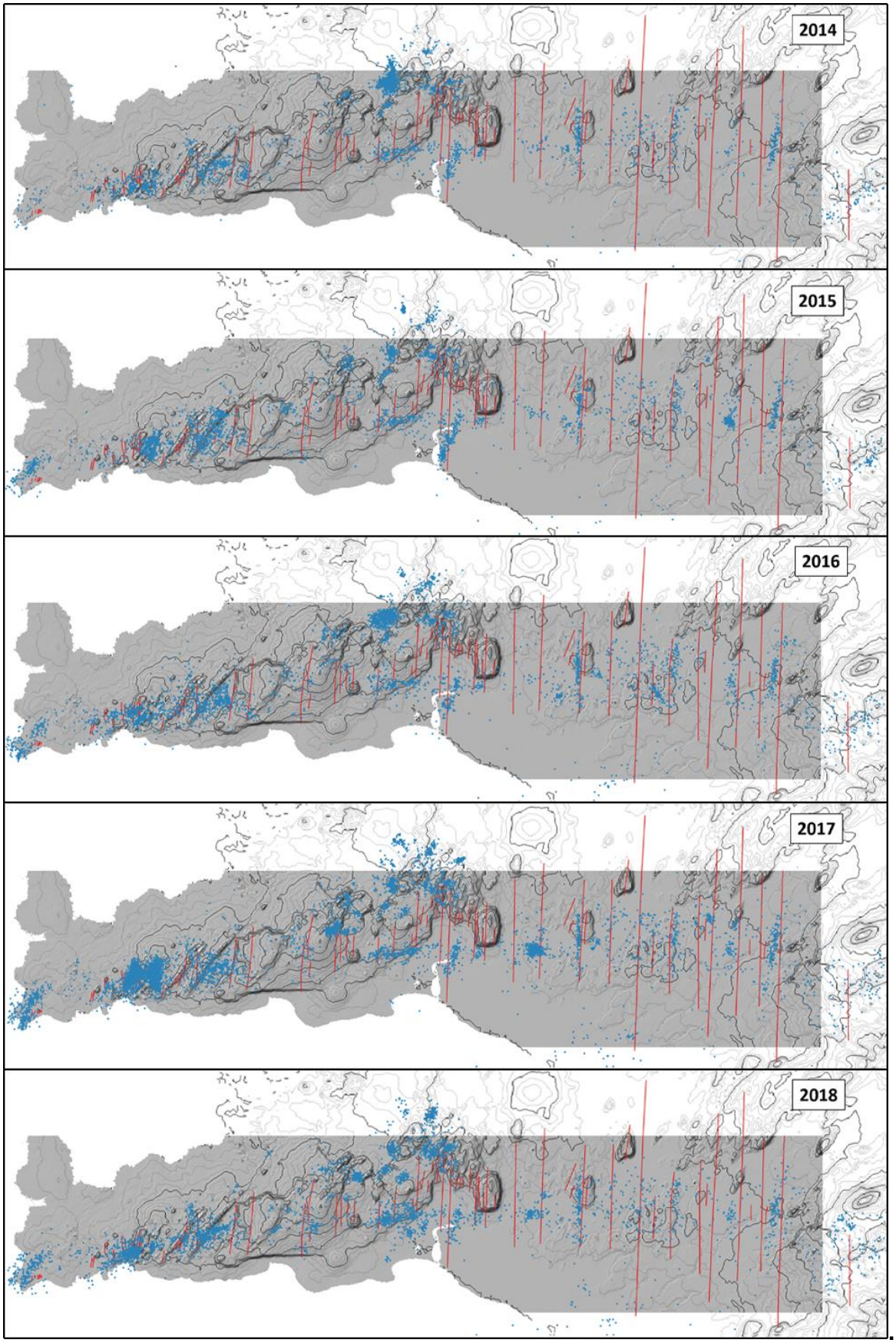

A1.7c.

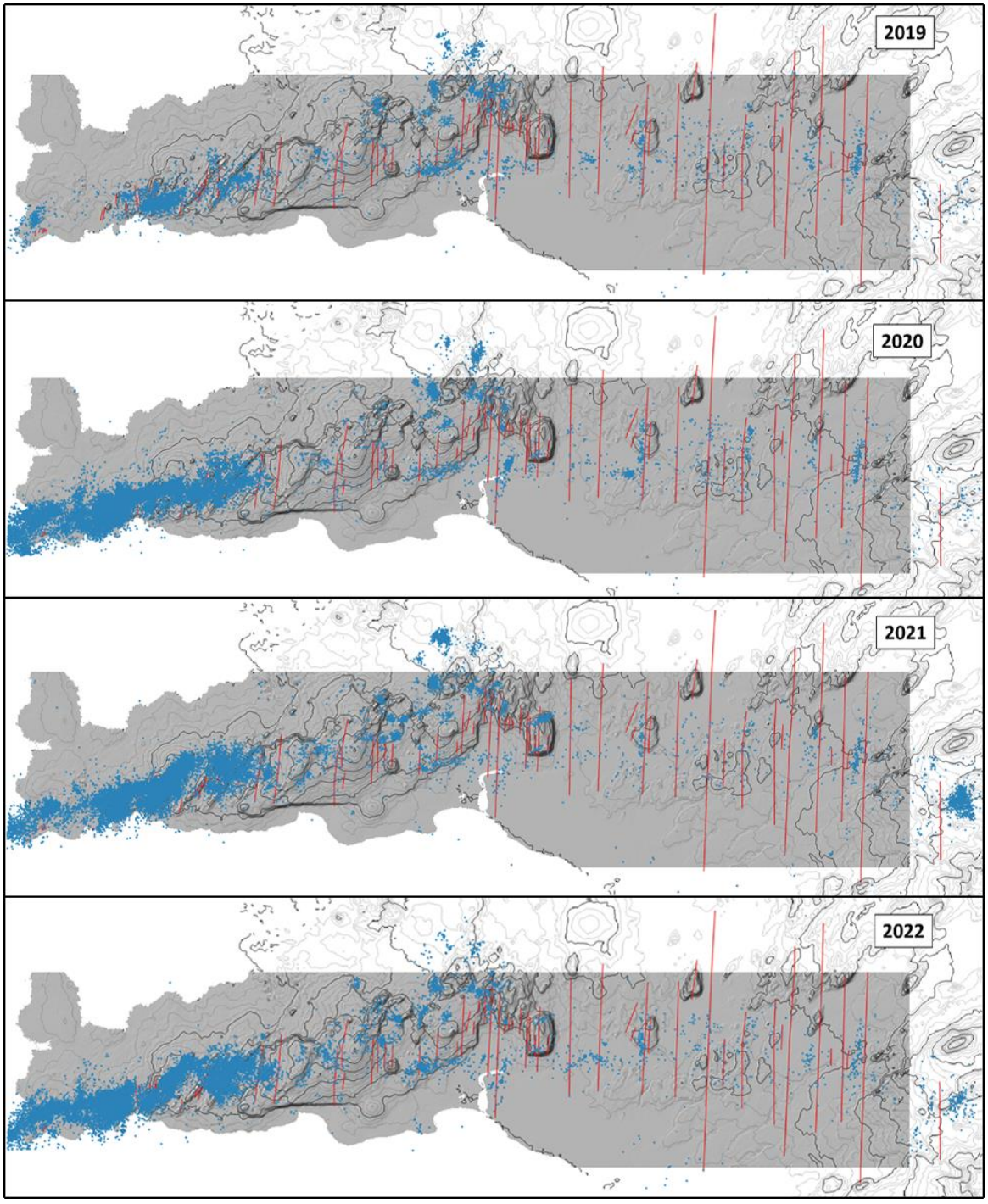

Appendices 1.7. Earthquakes location maps per years

MATLAB Diagram

A2.1.

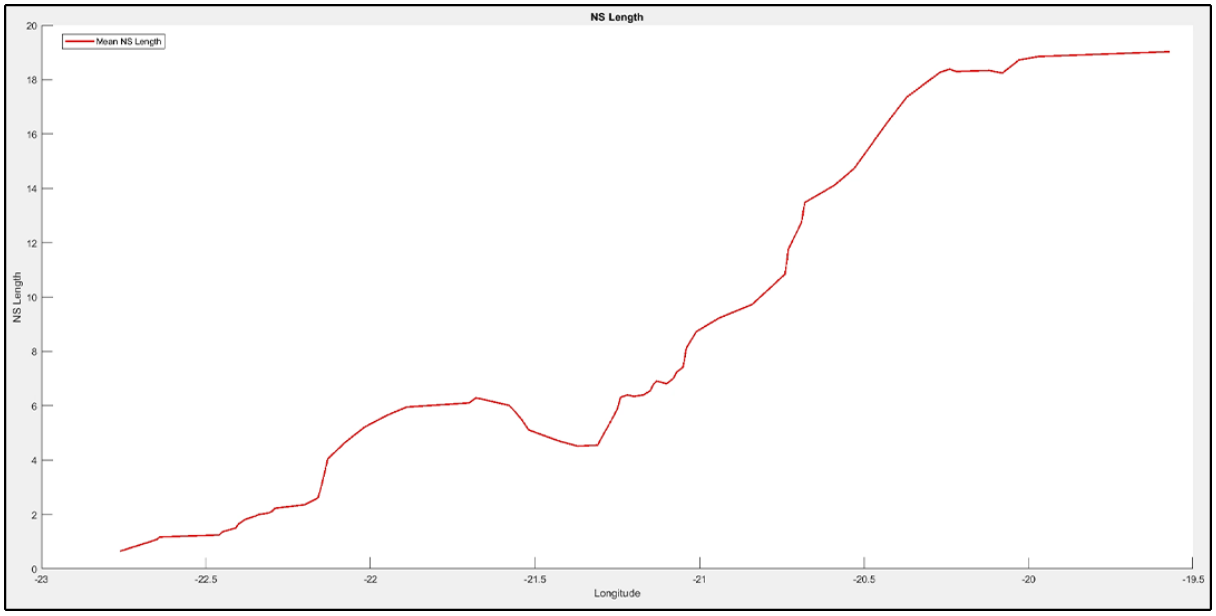

Appendix 2.1. Local mean length in kilometres of the NS main faults along the longitude

A2.2.

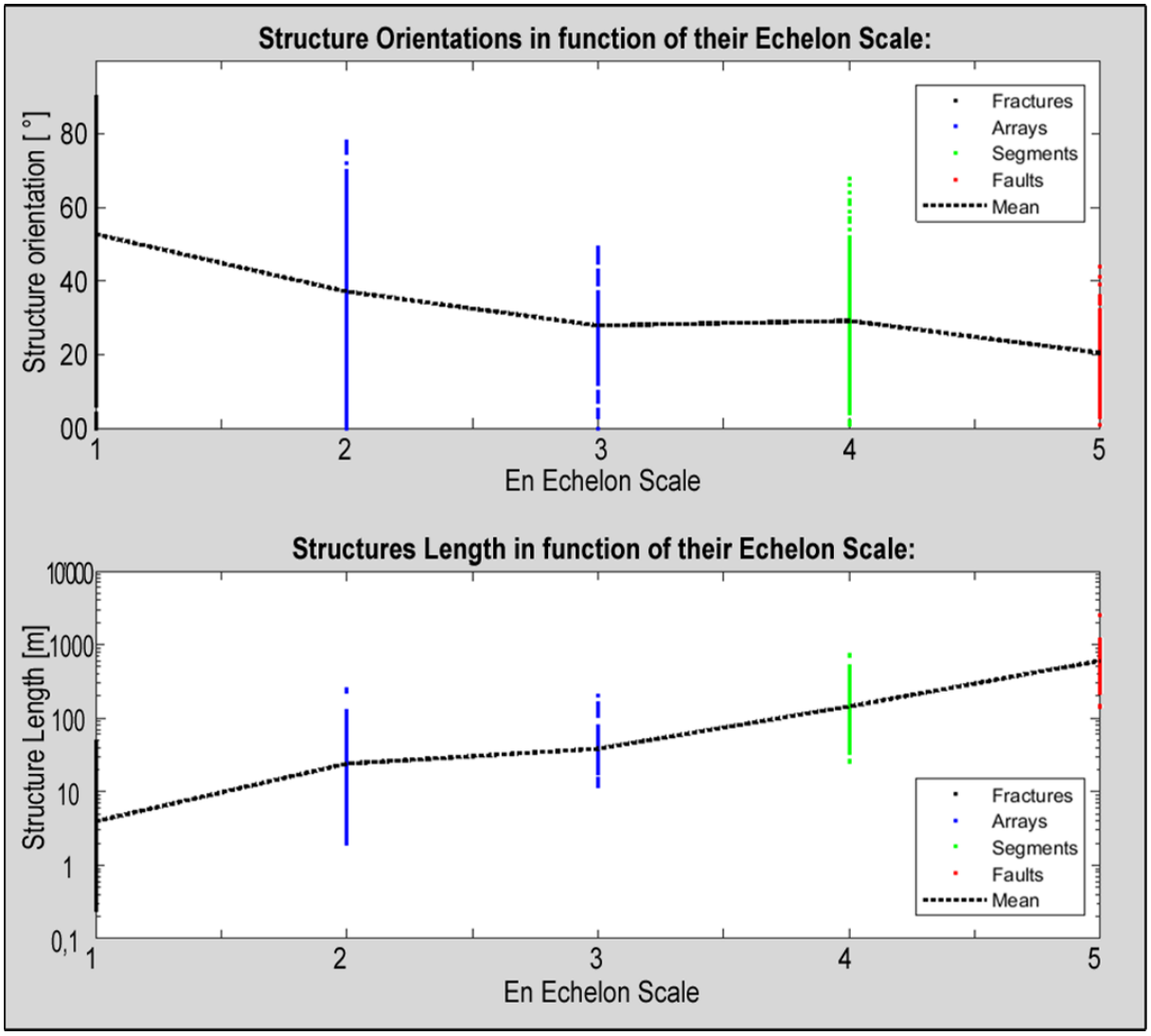

Appendix 2.2. Strike en Length disparity between the different en-echelon scale

A2.3.

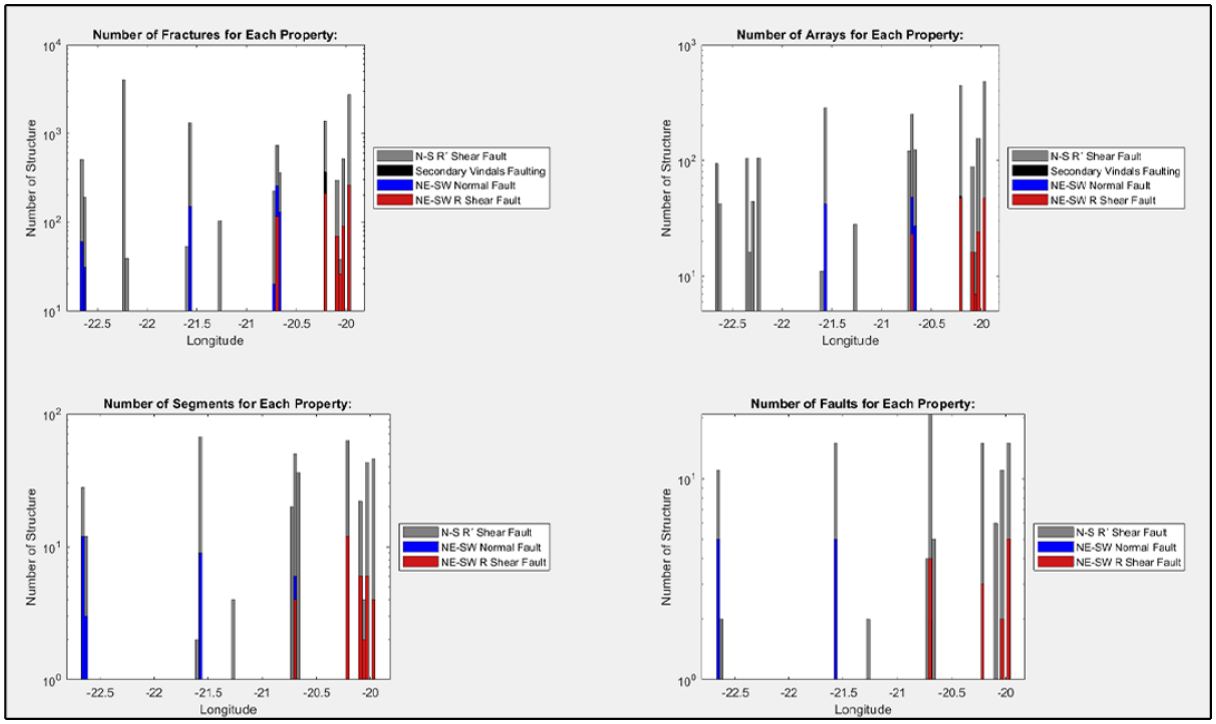

Appendix 2.3. Distribution of mapped number of the different types of structure along the longitude

A2.4.

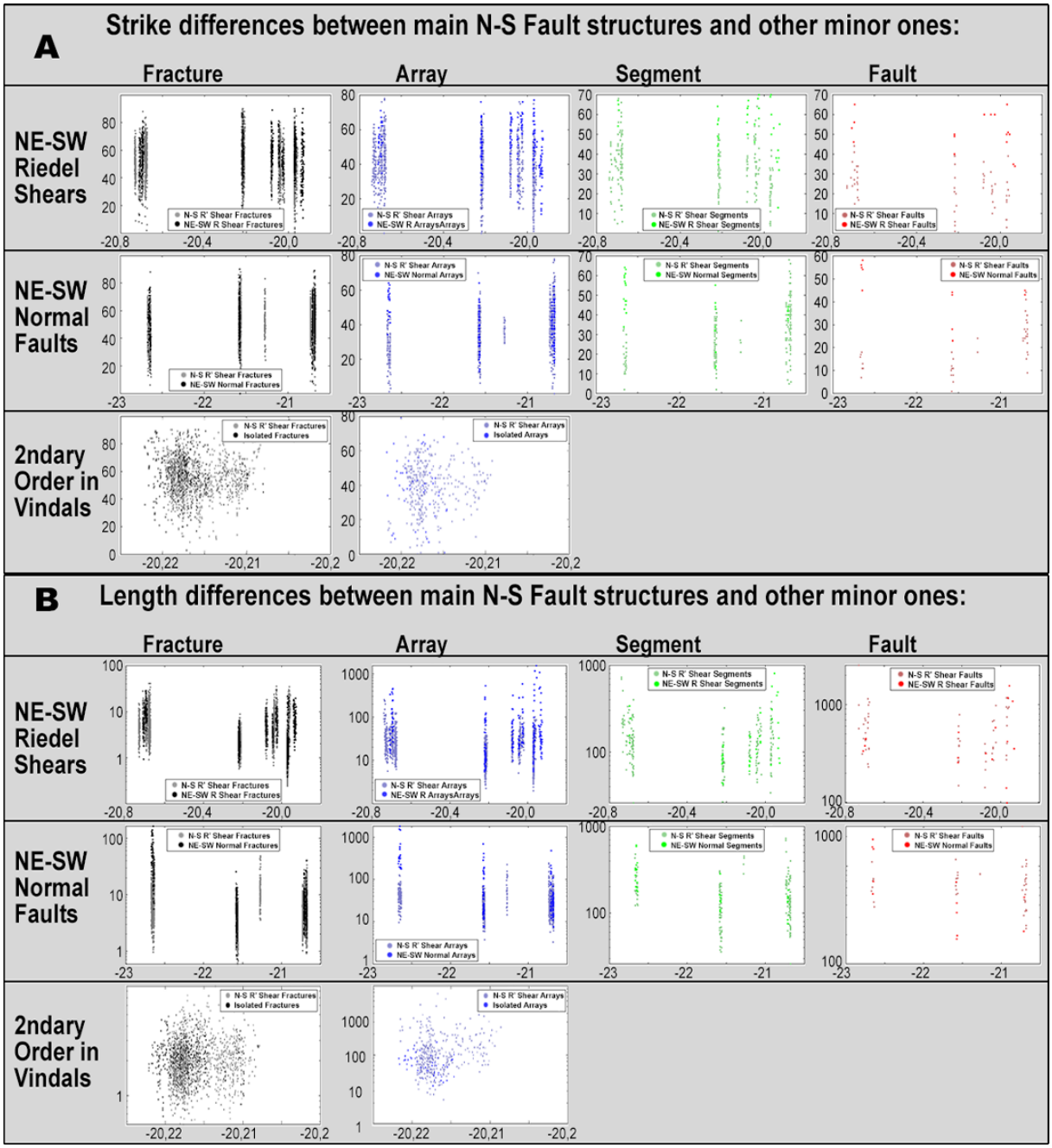

Appendix 2.4. Non-NS R' structures strike and length results

A2.5.

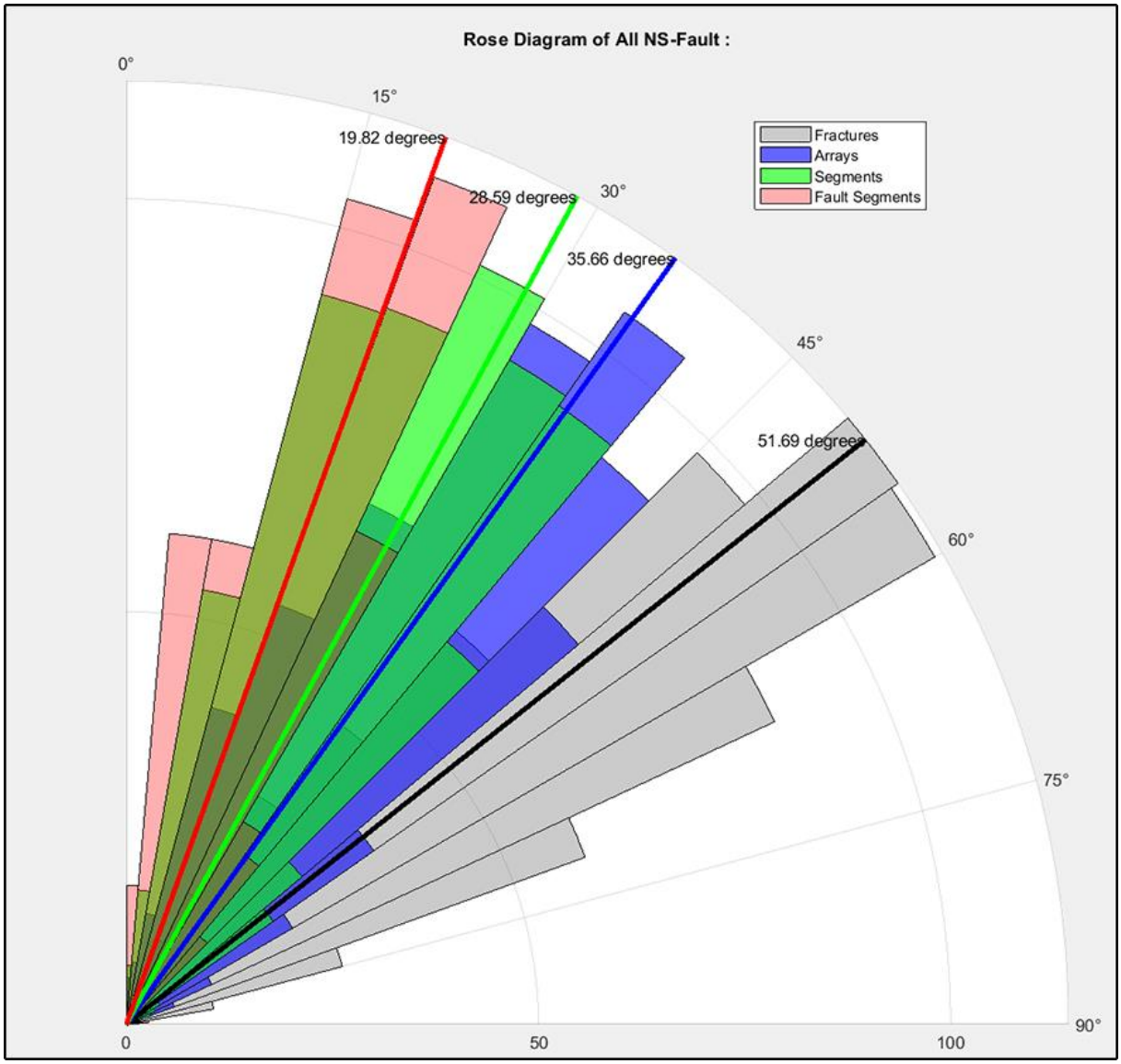

Appendix 2.5. Rose diagram of the strike of all en-echelon of NS fault with their respective mean

A2.6.

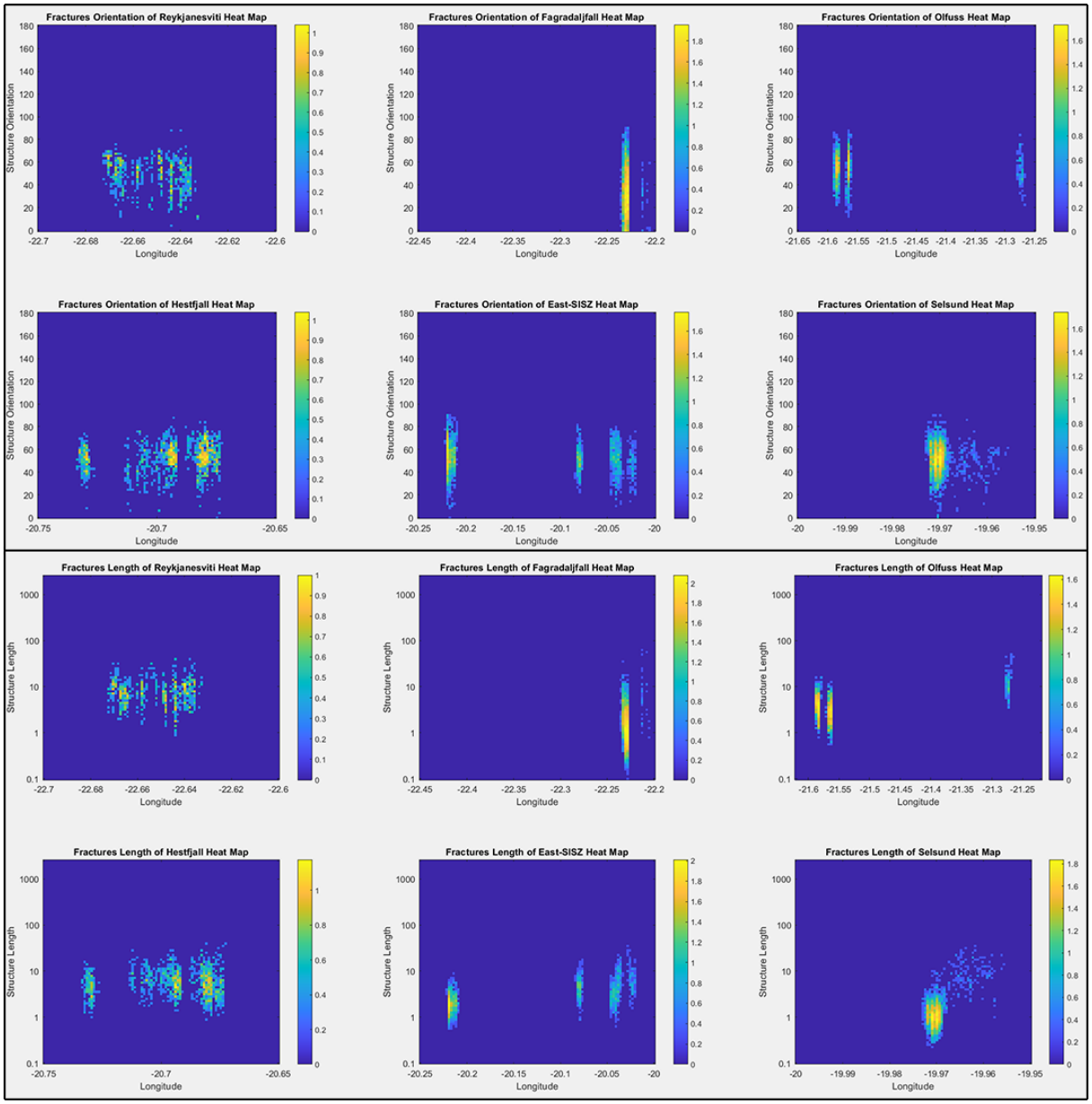

Appendix 2.6. Strike and Density results of fractures of NS faults along the longitude displayed in density plot

A2.7.

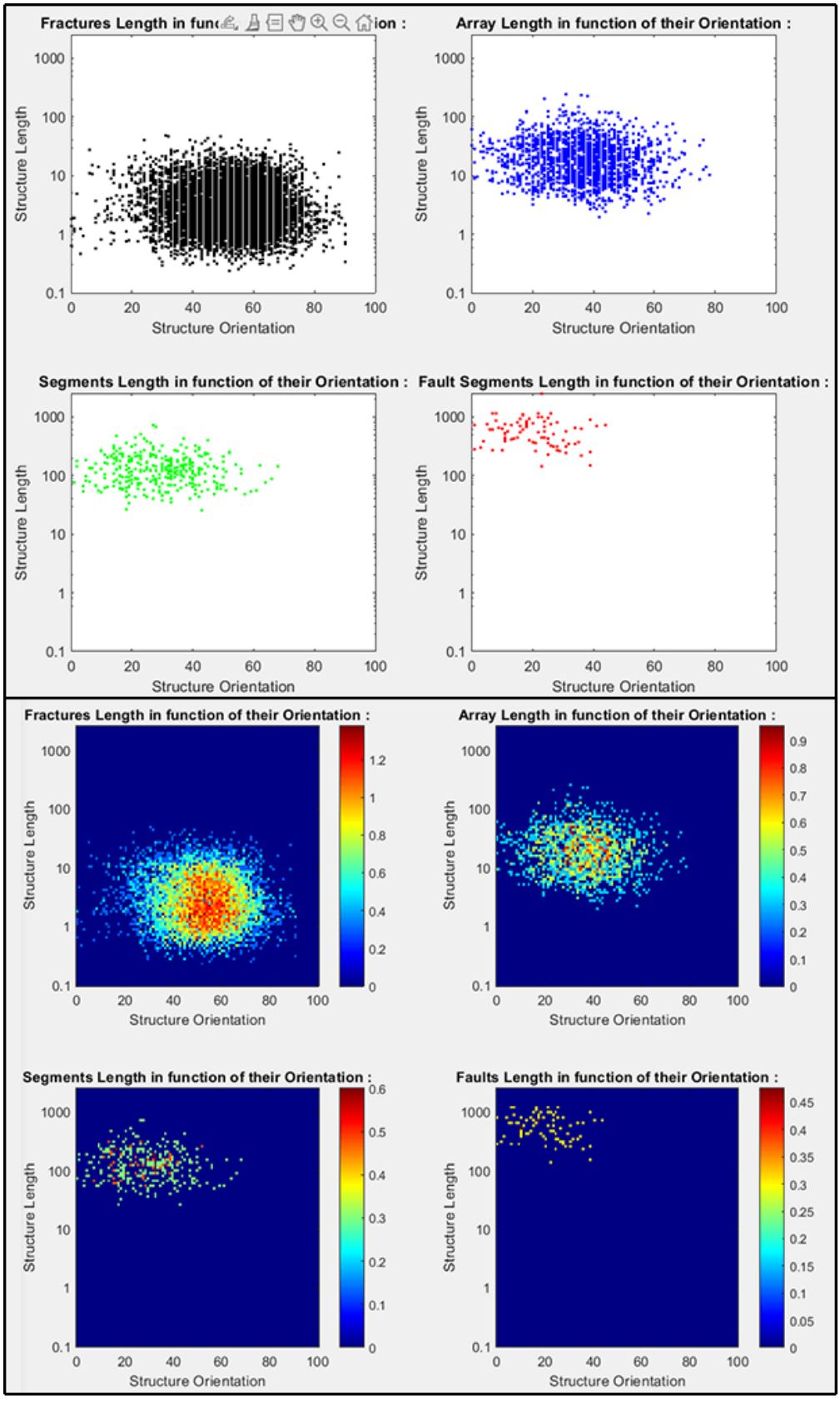

Appendix 2.7. Length of the NS structures in function of their strike

A2.8.

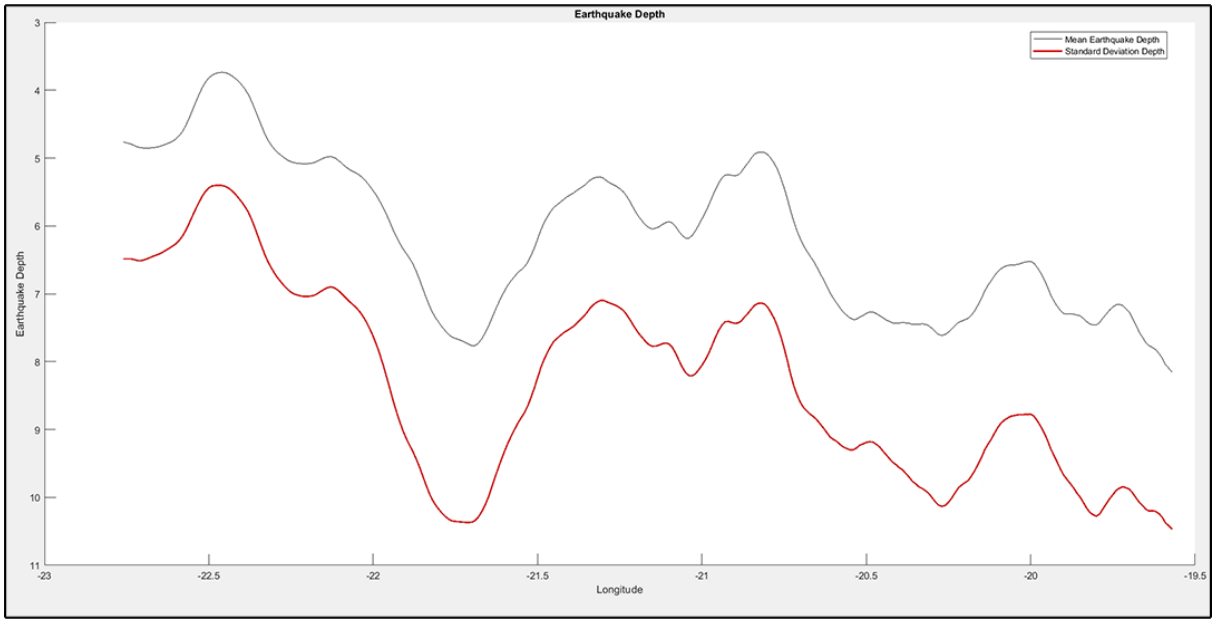

Appendix 2.8. Larger compute window mean for the earthquake maximum standard deviation depth, it is the data used to calculate the fault plane in Figure 6.7.

A2.9.

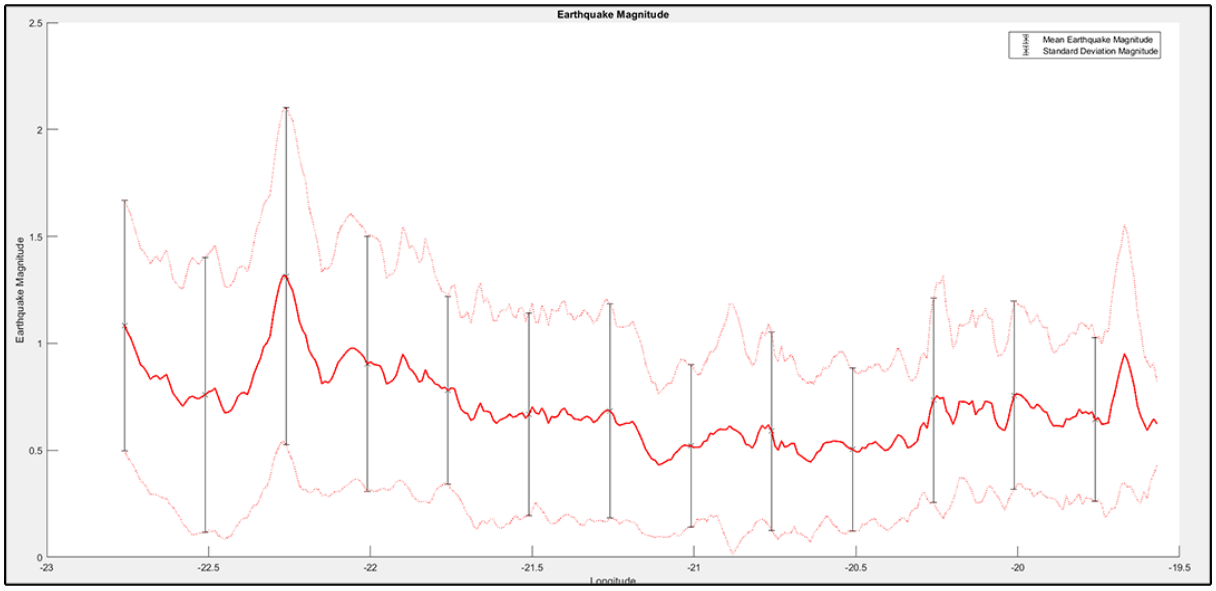

Appendix 2.9. Mean magnitude and its standard deviation in function of the longitude

A2.10.

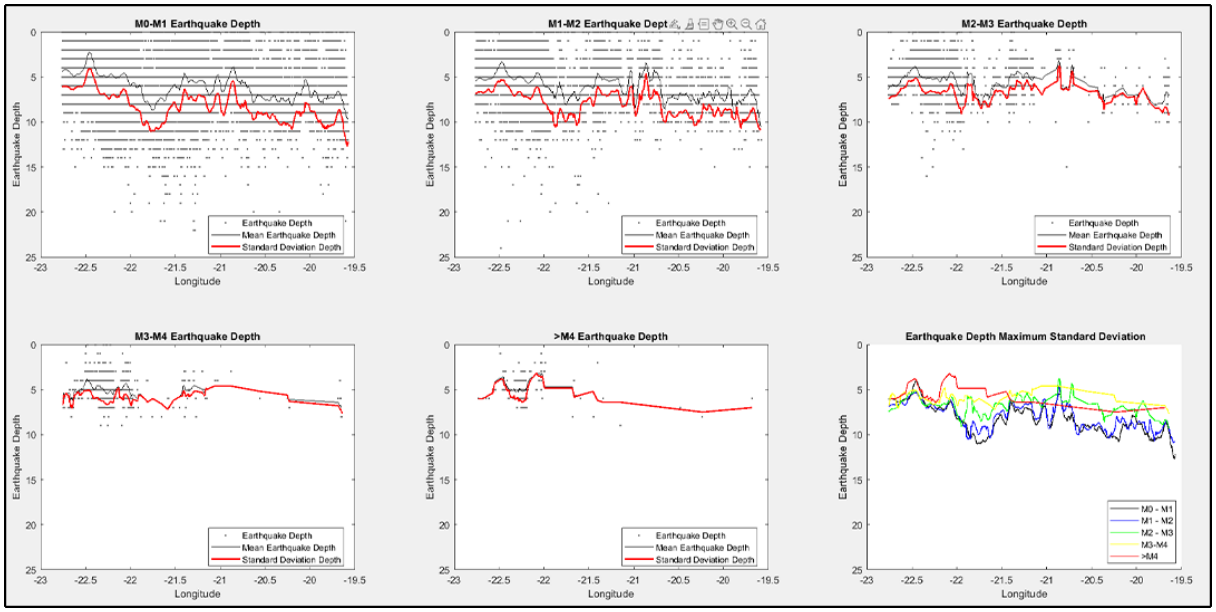

Appendix 2.10. Maximum standard deviation depth along the longitude in function of the event magnitude

From literature

A3.1.

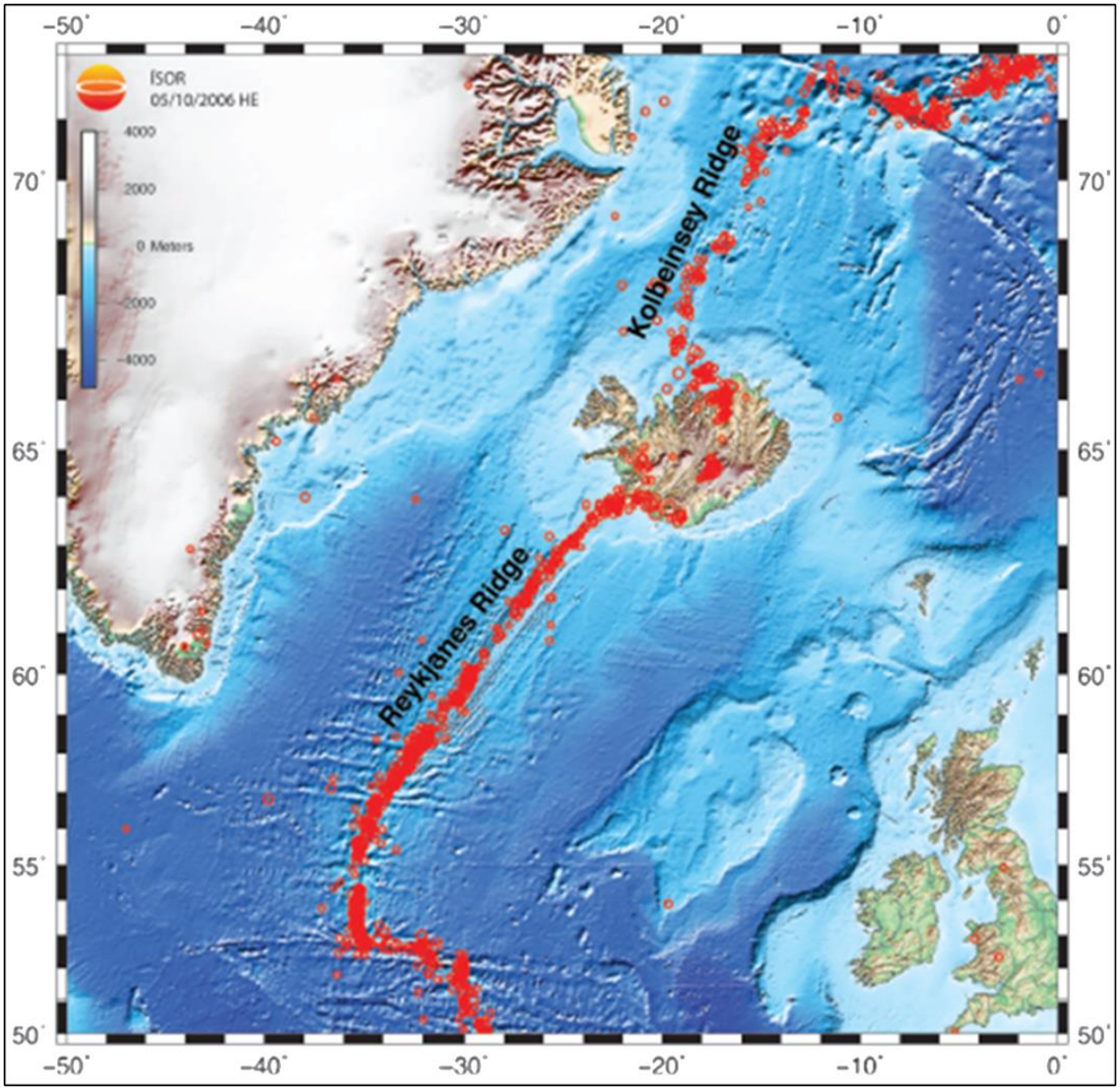

Appendix 3.1. Earthquake occurring along the North-Atlantic Ridge map with the location of the Reykjanes Ridge and the Kolbeinsey Ridge. From Einarsson, 2008.

A3.2.

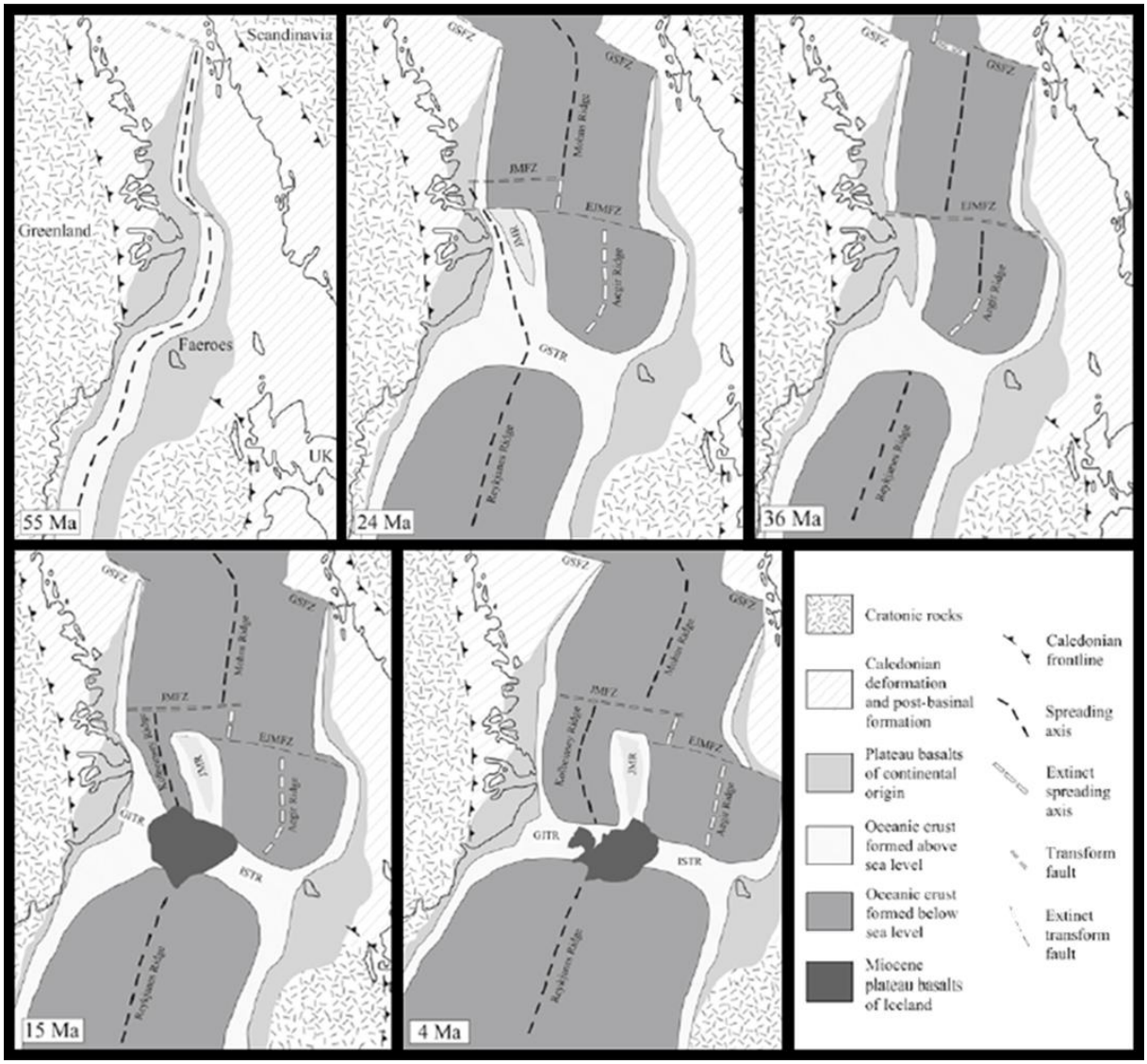

Appendix 3.2. Evolution of the North-Atlantic Ridge location since the beginning of the North-Atlantic opening. From Denk et al., 2011.

A3.3.

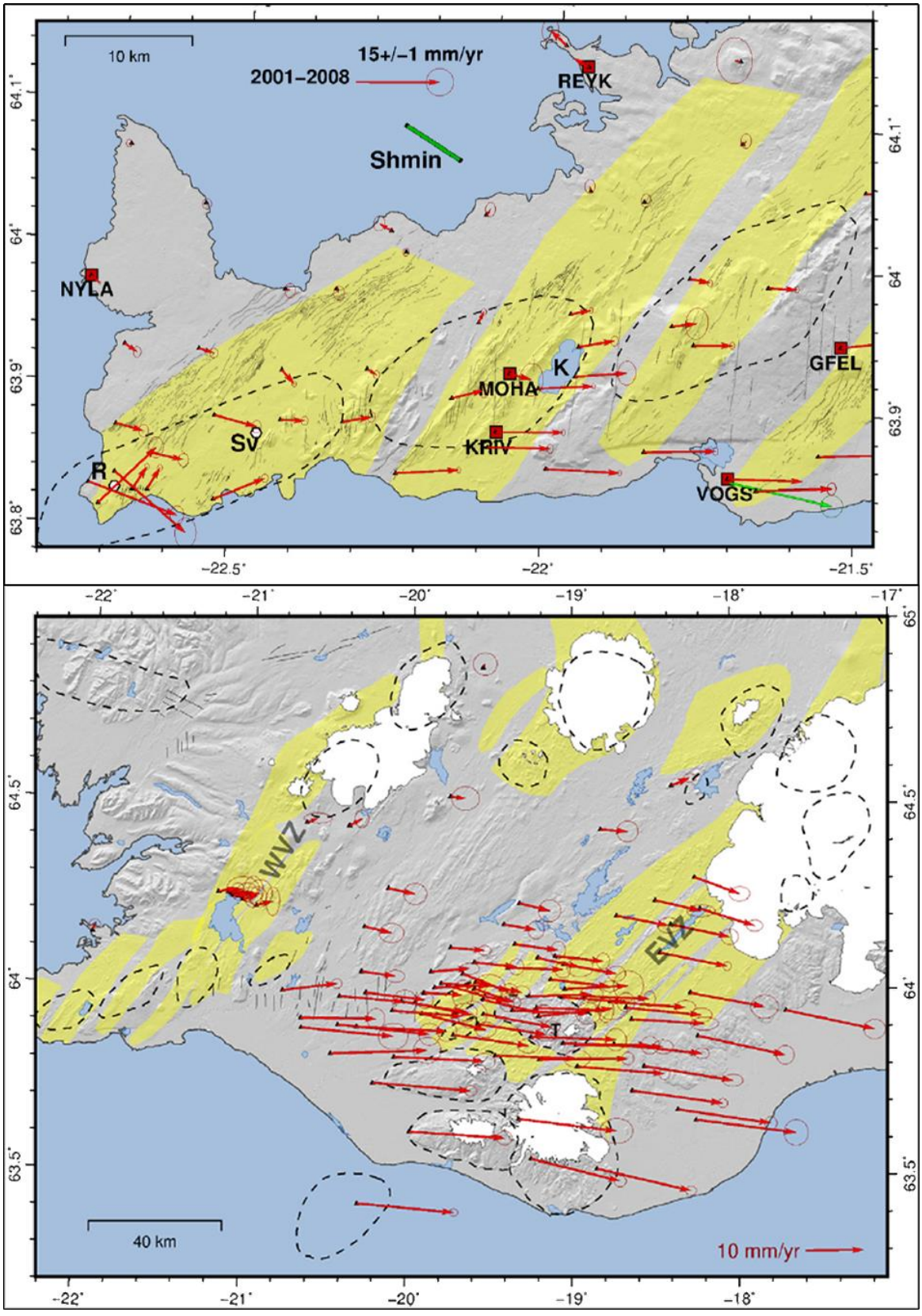

Appendix 3.3. Southwest Iceland plate spreading vector seen by GPS. From Sigmundsson et al., 2020b.

A3.4.

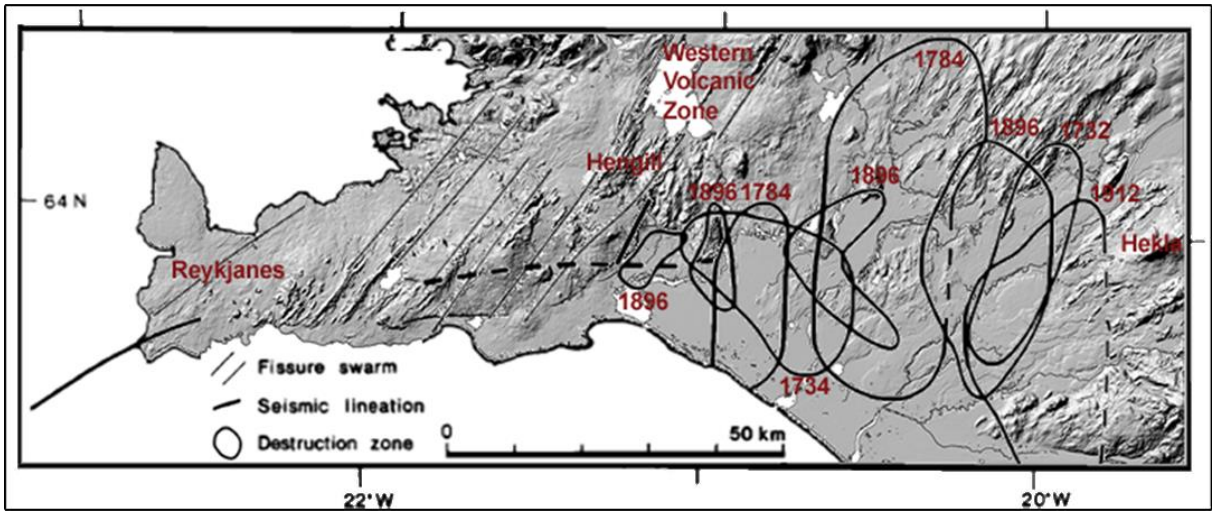

Appendix 3.4. Historic large earthquake destruction zone map via old registers in SISZ. Modified from Einarsson et al., 1981.

A3.5.

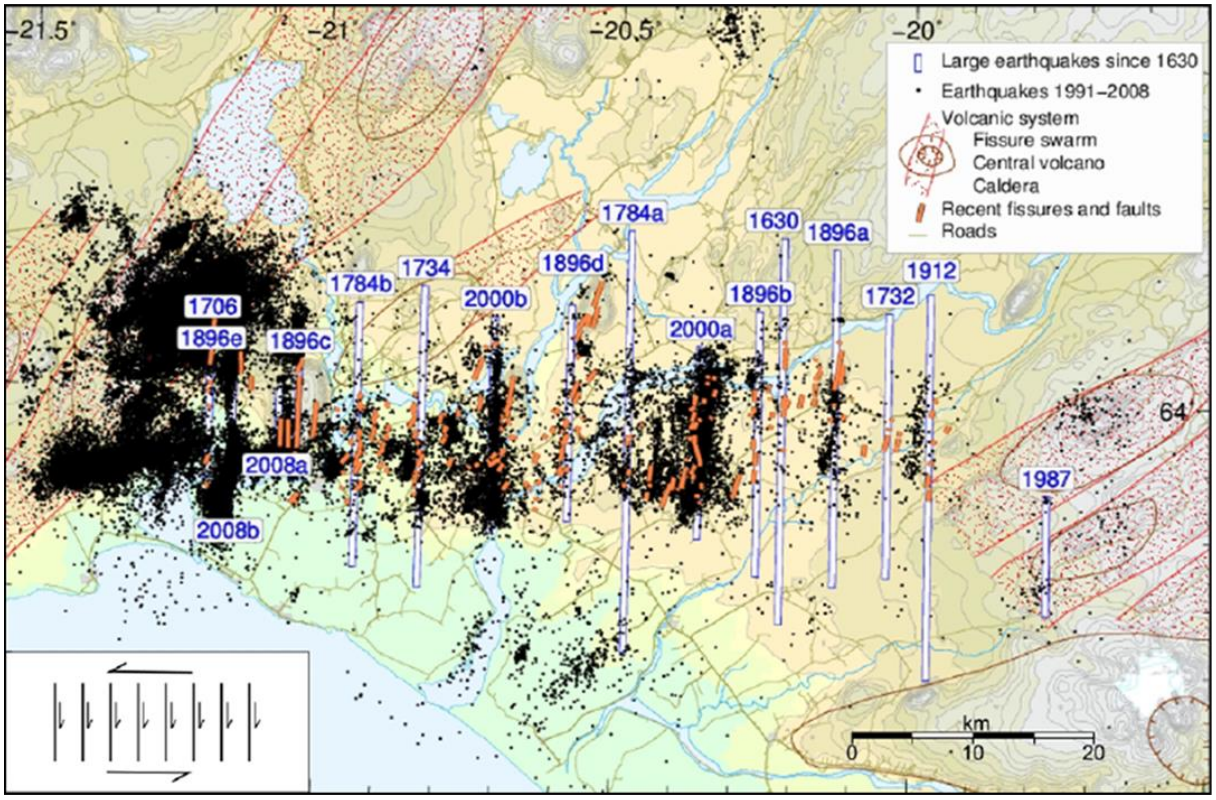

Appendix 3.5. Main NS faults in SISZ link to historical earthquakes. From Karson et al., 2019.

A3.6.

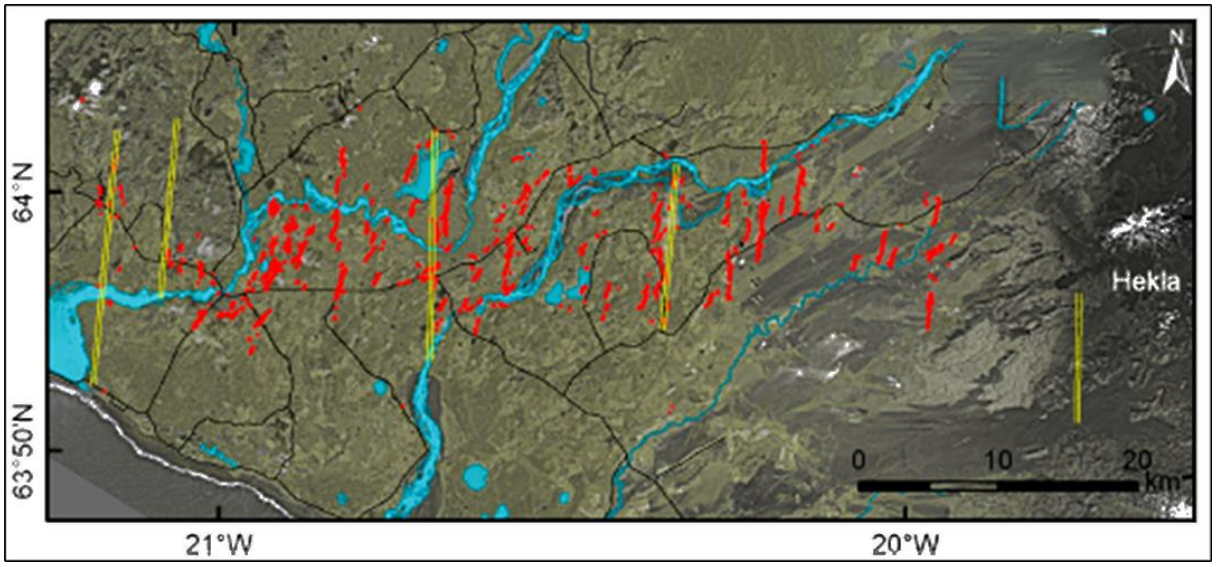

Appendix 3.6. Surface fractures map in SISZ. From Einarsson, 2010.

A3.7.

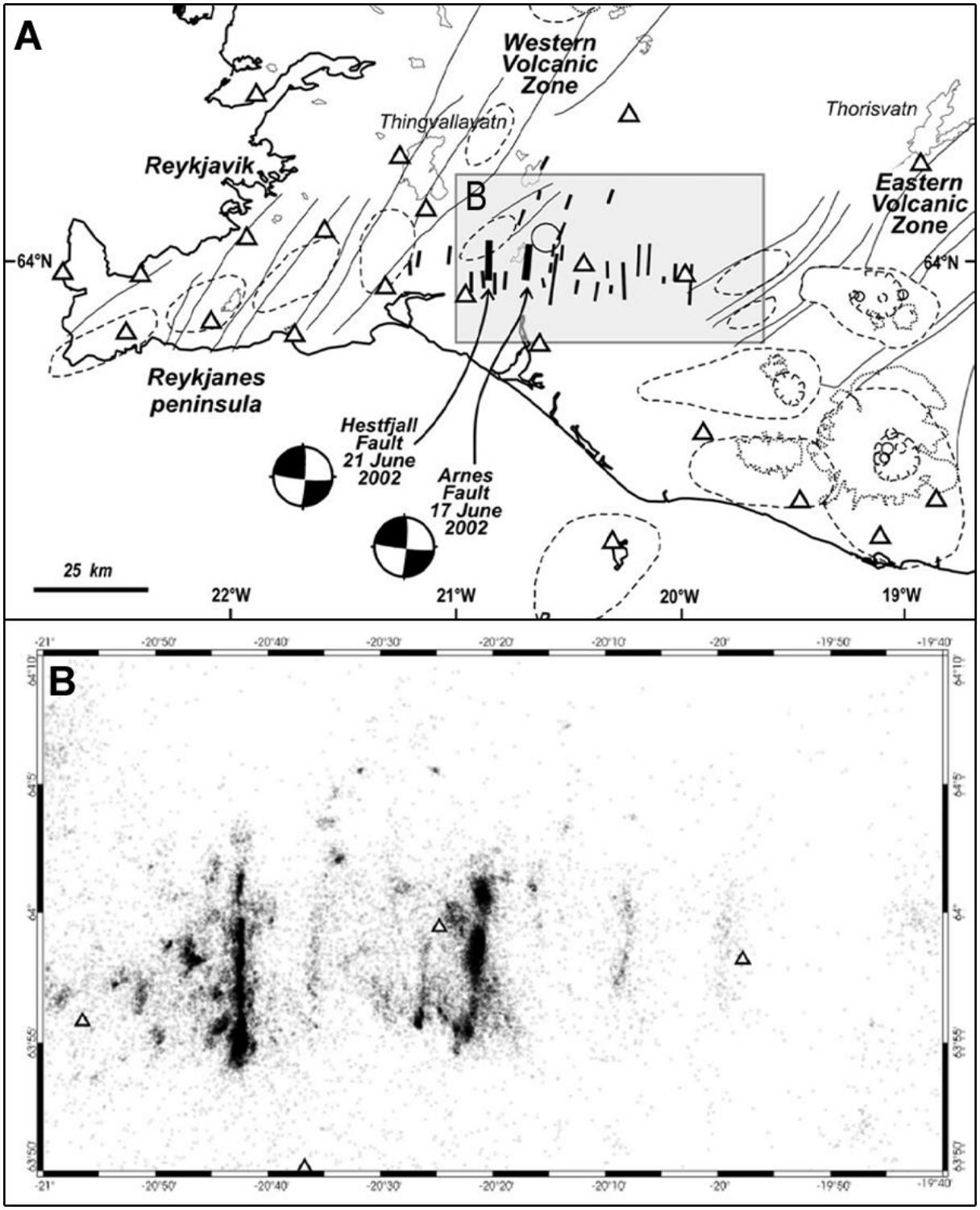

Appendix 3.7. Earthquake between 1991 and 2004 location in SISZ map. From Angelier et al., 2008.

A3.8.

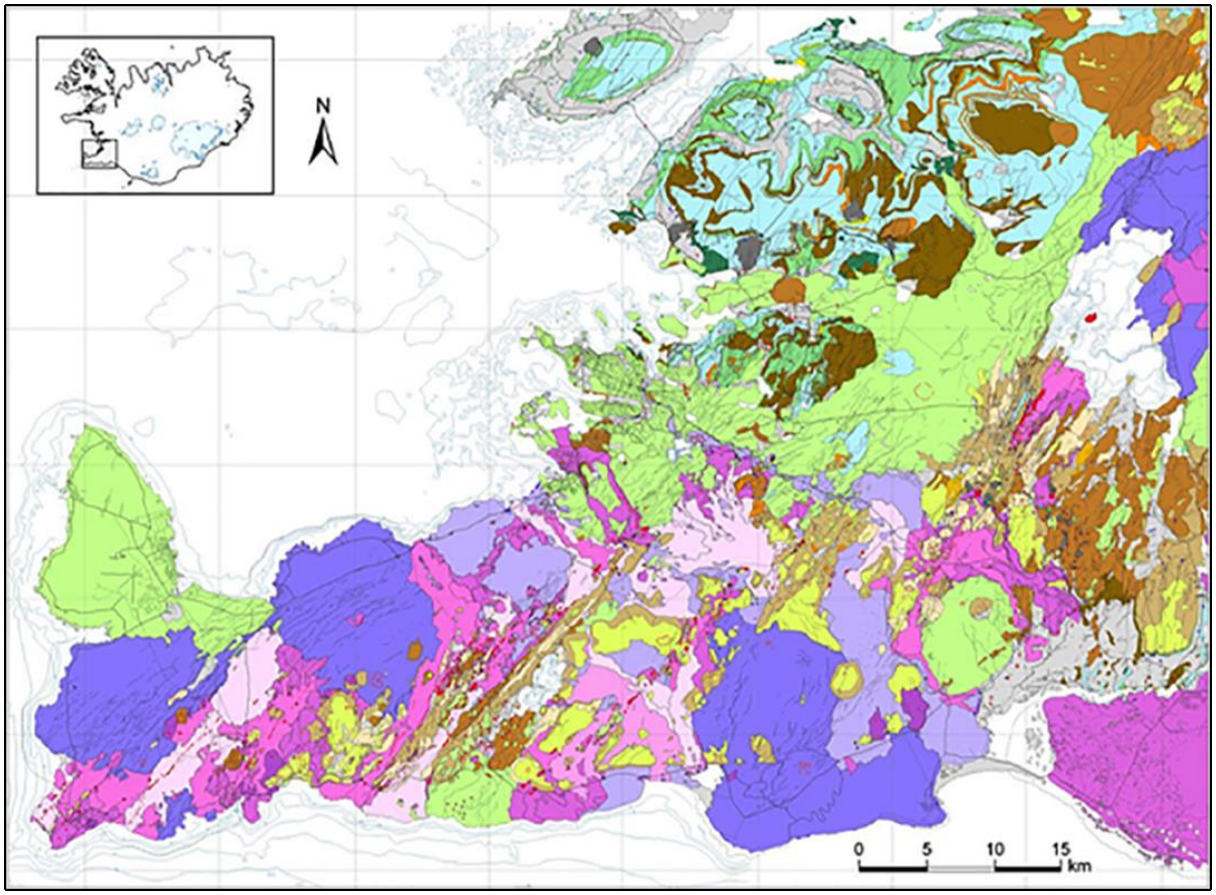

Appendix 3.8. Reykjanes geological map by Saemundsson. From Sæmundsson et al., 2020.

A3.9.

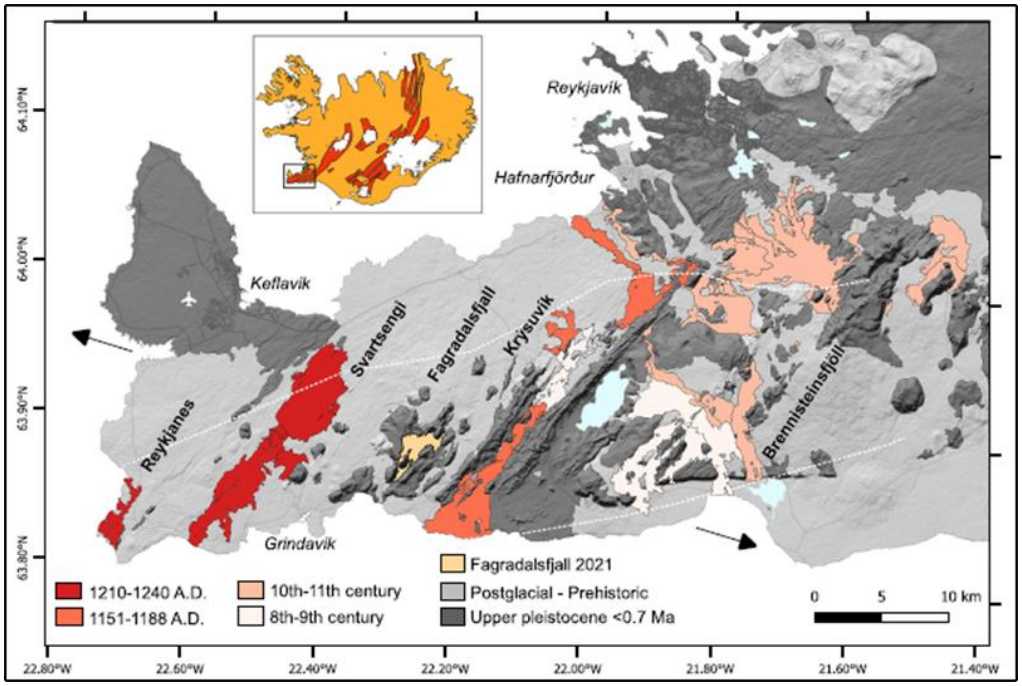

Appendix 3.9. Recent lava field in Reykjanes. From Caracciolo et al., 2023.

A3.10.

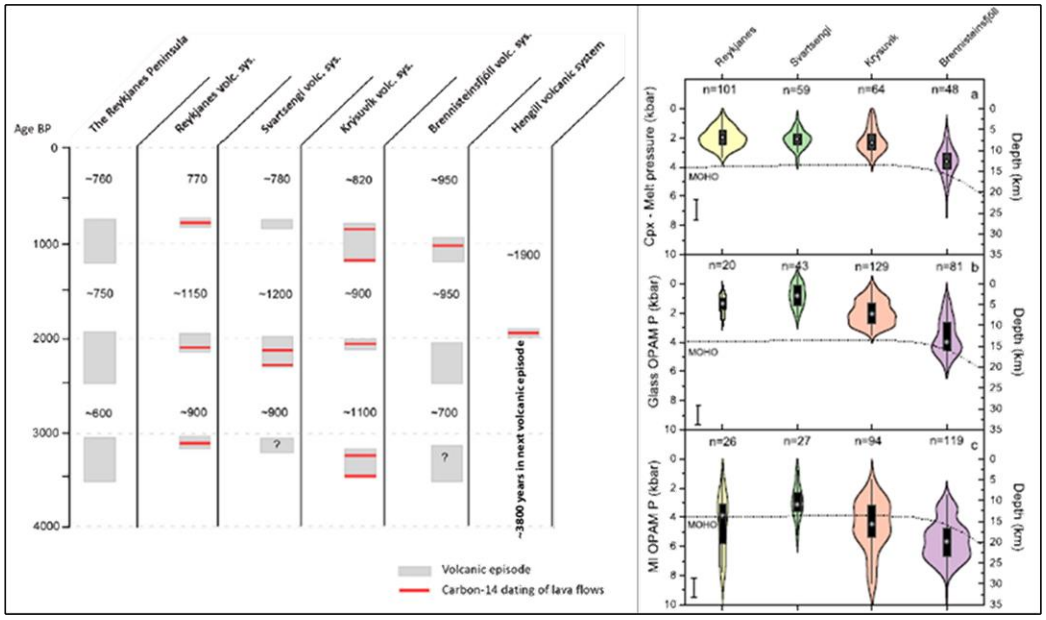

Appendix 3.10. Last eruption episode and their plumbing in Reykjanes in function of the volcanic system. From Caracciolo et al., 2023 and Sæmundsson et al., 2020.

A3.11

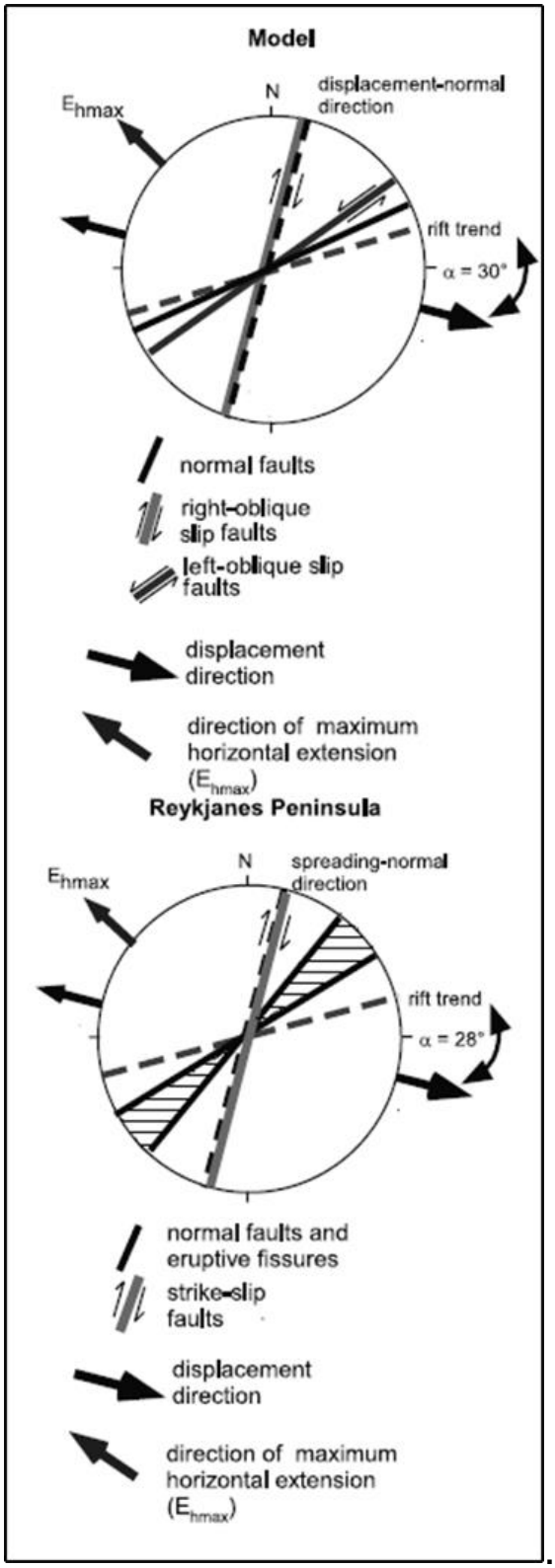

Appendix 3.11. Reykjanes oblique rift measurments vs analogue model structures, further informotion for Figure 3.8. From A. Clifton & Schlische, 2003.

A3.12.

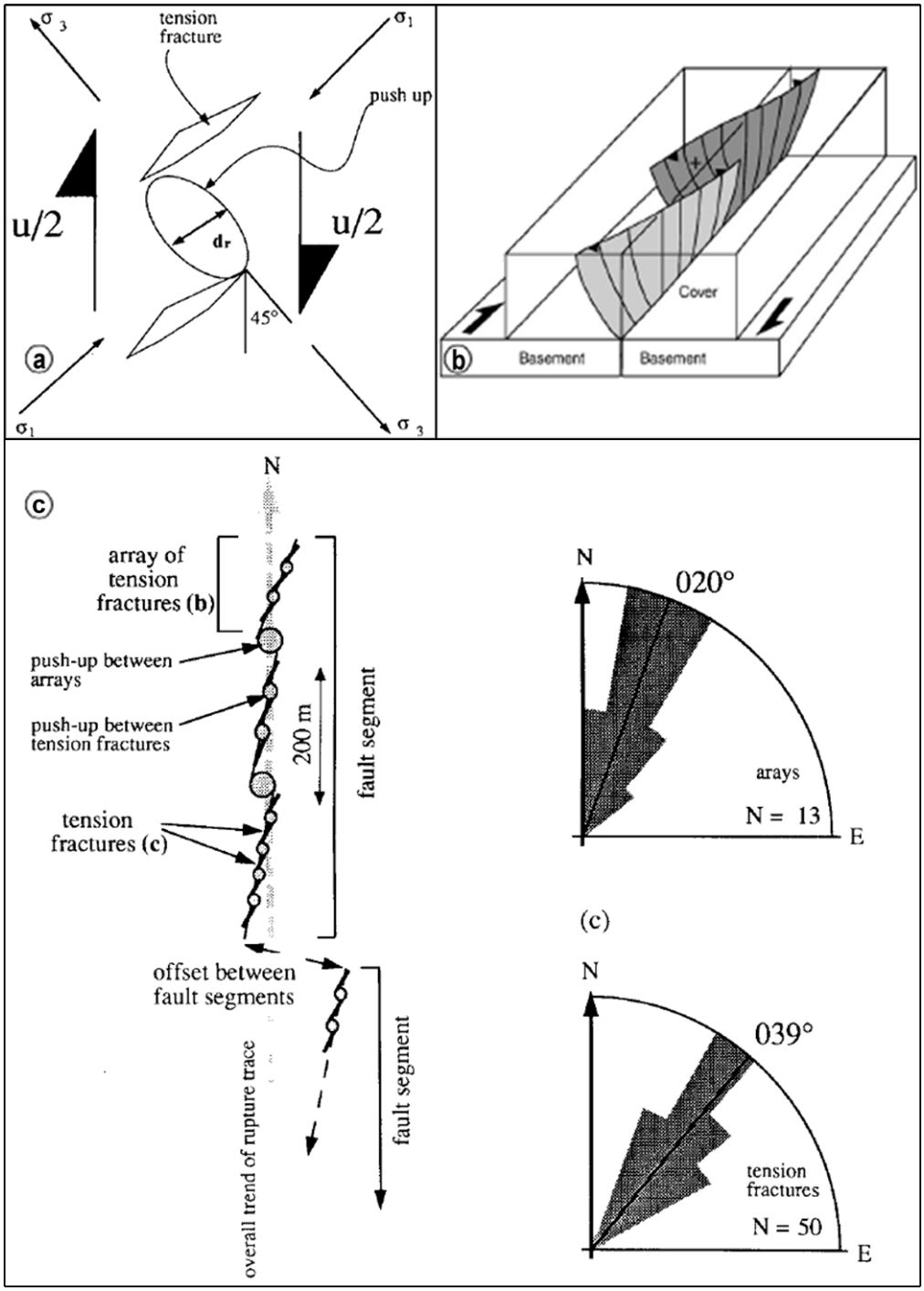

Appendix 3.12. a. Stress system in en-echelon system to create a push-up. **b.** En-echelon depth propagation and connection. **a** and **b** from (Dooley & Schreurs, 2012). **c.** En-echelon old mapping of Selsund with different en-echelon scales identified, with their measured strike. From Bjarnason et al., 1993.

B

Bibliography

Ahlgren, S. G. (2001). The nucleation and evolution of Riedel shear zones as deformation bands in porous sandstone. *Journal of Structural Geology*, *23*(8), 1203–1214. https://doi.org/10.1016/S0191-8141(00)00183-8

Allen, R. M., Nolet, G., Morgan, W. J., Vogfjörd, K., Bergsson, B. H., Erlendsson, P., Foulger, G. R., Jakobsdóttir, S., Julian, B. R., Pritchard, M., Ragnarsson, S., & Stefánsson, R. (2002). Imaging the mantle beneath Iceland using integrated seismological techniques. *Journal of Geophysical Research: Solid Earth*, *107*(B12), ESE 3-1-ESE 3-16. https://doi.org/10.1029/2001JB000595

Angelier, J., Bergerat, F., Stefansson, R., & Bellou, M. (2008). Seismotectonics of a newly formed transform zone near a hotspot: Earthquake mechanisms and regional stress in the South Iceland Seismic Zone. *Tectonophysics*, *447*(1), 95–116. https://doi.org/10.1016/j.tecto.2006.07.016

Árnadóttir, T., Jiang, W., Feigl, K. L., Geirsson, H., & Sturkell, E. (2006). Kinematic models of plate boundary deformation in southwest Iceland derived from GPS observations.

Journal of Geophysical Research: Solid Earth, *111*(B7). https://doi.org/10.1029/2005JB003907

Árnadóttir, T., Jónsson, S., Pedersen, R., & Gudmundsson, G. B. (2003). Coulomb stress changes in the South Iceland Seismic Zone due to two large earthquakes in June 2000. *Geophysical Research Letters*, *30*(5). https://doi.org/10.1029/2002GL016495

Atmaoui, N. (2005). *Development of pull-apart basins and associated structures by the riedel shear mechanism: Insight from scaled clay analogue models*.

Barsotti, S., Parks, M. M., Pfeffer, M. A., Óladóttir, B. A., Barnie, T., Titos, M. M., Jónsdóttir, K., Pedersen, G. B. M., Hjartardóttir, Á. R., Stefansdóttir, G., Johannsson, T., Arason, Þ., Gudmundsson, M. T., Oddsson, B., Þrastarson, R. H., Ófeigsson, B. G., Vogfjörd, K., Geirsson, H., Hjörvar, T., … Sigurðsson, E. M. (2023). The eruption in Fagradalsfjall (2021, Iceland): How the operational monitoring and the volcanic hazard assessment contributed to its safe access. *Natural Hazards*, *116*(3), 3063–3092. https://doi.org/10.1007/s11069-022-05798-7

Bergerat, F., & Angelier, J. (2000). The South Iceland Seismic Zone: Tectonic and sismotectonic analyses revealing the evolution from rifting to transform motion. *Journal of Geodynamics*, *29*(3), 211–231. https://doi.org/10.1016/S0264-3707(99)00046-0

Bergerat, F., & Angelier, J. (2003). Mechanical behaviour of the Árnes and Hestfjall Faults of the June 2000 earthquakes in Southern Iceland: Inferences from surface traces and tectonic model. *Journal of Structural Geology*, *25*(9), 1507–1523. https://doi.org/10.1016/S0191-8141(02)00168-2

Bergerat, F., & Angelier, J. (2008). Immature and mature transform zones near a hot spot: The South Iceland Seismic Zone and the Tjörnes Fracture Zone (Iceland). *Tectonophysics*, *447*(1), Article 1. https://doi.org/10.1016/j.tecto.2006.05.046

Bergerat, F., Angelier, J., Gudmundsson, A., & Torfason, H. (2003). Push-ups, fracture patterns, and palaeoseismology of the Leirubakki Fault, South Iceland. *Journal of Structural Geology*, *25*(4), Article 4. https://doi.org/10.1016/S0191-8141(02)00051-2

Bjarnason, I., Cowie, P., Anders, M., Seeber, L., & Scholz, C. (1993). The 1912 Iceland Earthquake Rupture, Growth and Development of a Nascent Transform System. *Bulletin of the Seismological Society of America*, *83*, 416–435.

Bjarnason, I., & Einarsson, P. (1991). Source Mechanism of the 1987 Vatnafj511 Earthquake in South Iceland. *JOURNAL OF GEOPHYSICAL RESEARCH*, *96*(B3), 4313–4324.

Bramham, E. K., Wright, T. J., Paton, D. A., & Hodgson, D. M. (2021a). A new model for the growth of normal faults developed above pre-existing structures. *Geology*, *49*(5), 587–591. https://doi.org/10.1130/G48290.1

Bufféral, S., Panza, E., Mannini, S., Hjartardóttir, Á. R., Nobile, A., Gies, N., Óskarsson, B. V., & Ruch, J. (2023). Surface fractures generated during the 2021 Reykjanes oblique rifting event (SW Iceland). *Bulletin of Volcanology*, *85*(11), 64. https://doi.org/10.1007/s00445-023-01666-9

Caracciolo, A., Bali, E., Halldórsson, S. A., Guðfinnsson, G. H., Kahl, M., Þórðardóttir, I., Pálmadóttir, G. L., & Silvestri, V. (2023). Magma plumbing architectures and timescales of magmatic processes during historical magmatism on the Reykjanes Peninsula, Iceland. *Earth and Planetary Science Letters*, *621*, 118378. https://doi.org/10.1016/j.epsl.2023.118378

Clifton, A. E., & Kattenhorn, S. A. (2006a). Structural architecture of a highly oblique divergent plate boundary segment. *Tectonophysics*, *419*(1), 27–40. https://doi.org/10.1016/j.tecto.2006.03.016

Clifton, A. E., Pagli, C., Jónsdóttir, J. F., Eythorsdóttir, K., & Vogfjörð, K. (2003). Surface effects of triggered fault slip on Reykjanes Peninsula, SW Iceland. *Tectonophysics*, *369*(3), 145–154. https://doi.org/10.1016/S0040-1951(03)00201-4

Clifton, A. E., Schlische, R. W., Withjack, M. O., & Ackermann, R. V. (2000). Influence of rift obliquity on fault-population systematics: Results of experimental clay models. *Journal of Structural Geology*, *22*(10), 1491–1509. https://doi.org/10.1016/S0191-8141(00)00043-2

Clifton, A., & Einarsson, P. (2005). Styles of surface rupture accompanying the June 17 and 21, 2000 earthquakes in the South Iceland Seismic Zone. *Tectonophysics*, *396*(3), 141–159. https://doi.org/10.1016/j.tecto.2004.11.007

Clifton, A., & Schlische, R. (2003). Fracture populations on the Reykjanes Peninsula, Iceland: Comparison with experimental clay models of oblique rifting. *Journal of Geophysical Research*, *108*. https://doi.org/10.1029/2001JB000635

Corti, N., Bonali, F. L., Pasquaré Mariotto, F., Tibaldi, A., Russo, E., Hjartardóttir, Á. R., Einarsson, P., Rigoni, V., & Bressan, S. (2021). Fracture Kinematics and Holocene Stress Field at the Krafla Rift, Northern Iceland. *Geosciences*, *11*(2), Article 2. https://doi.org/10.3390/geosciences11020101

Cubuk-Sabuncu, Y., Jónsdóttir, K., Caudron, C., Lecocq, T., Parks, M. M., Geirsson, H., & Mordret, A. (2021). Temporal Seismic Velocity Changes During the 2020 Rapid Inflation at Mt. Þorbjörn-Svartsengi, Iceland, Using Seismic Ambient Noise. *Geophysical Research Letters*, *48*(11), e2020GL092265. https://doi.org/10.1029/2020GL092265

Decriem, J., & Árnadóttir, T. (2012). Transient crustal deformation in the South Iceland Seismic Zone observed by GPS and InSAR during 2000–2008. *Tectonophysics*, *581*, 6–18. https://doi.org/10.1016/j.tecto.2011.09.028

Decriem, J., Árnadóttir, T., Hooper, A., Geirsson, H., Sigmundsson, F., Keiding, M., Ófeigsson, B. G., Hreinsdóttir, S., Einarsson, P., LaFemina, P., & Bennett, R. A. (2010). The 2008 May 29 earthquake doublet in SW Iceland. *Geophysical Journal International*, *181*(2), Article 2. https://doi.org/10.1111/j.1365-246X.2010.04565.x

Denk, T., Grímsson, F., Zetter, R., & Símonarson, L. A. (2011). Introduction to the Nature and Geology of Iceland. In T. Denk, F. Grimsson, R. Zetter, & L. A. Símonarson (Eds.), *Late Cainozoic Floras of Iceland: 15 Million Years of Vegetation and Climate History in the Northern North Atlantic* (pp. 1–29). Springer Netherlands. https://doi.org/10.1007/978-94-007-0372-8_1

Dooley, T. P., & Schreurs, G. (2012). Analogue modelling of intraplate strike-slip tectonics: A review and new experimental results. *Tectonophysics*, *574–575*, 1–71. https://doi.org/10.1016/j.tecto.2012.05.030

Einarsson, P. (2008). Plate boundaries, rifts and transforms in Iceland. *Jökull*, *58*, 35–58.

Einarsson, P. (2010). Mapping of Holocene surface ruptures in the South Iceland Seismic Zone. *Jökull*, *60*, 121–138.

Einarsson, P., Björnsson, S., Foulger, G., Stefánsson, R., & Skaftadóttir, T. (1981). *Seismicity Pattern in the South Iceland Seismic Zone*. 141–151. https://doi.org/10.1029/ME004p0141

Einarsson, P., & Brandsdóttir, B. (2021). Seismicity of the Northern Volcanic Zone of Iceland. *Frontiers in Earth Science*, *9*. https://www.frontiersin.org/articles/10.3389/feart.2021.628967

Einarsson, P., Eyjólfsson, V., & Hjartardóttir, Á. R. (2023). Tectonic framework and fault structures in the Fagradalsfjall segment of the Reykjanes Peninsula Oblique Rift, Iceland. *Bulletin of Volcanology*, *85*(2), 9. https://doi.org/10.1007/s00445-022-01624-x

Einarsson, P., Hjartardóttir, Á. R., Hreinsdóttir, S., & Imsland, P. (2020). The structure of seismogenic strike-slip faults in the eastern part of the Reykjanes Peninsula Oblique Rift, SW Iceland. *Journal of Volcanology and Geothermal Research*, *391*, 106372. https://doi.org/10.1016/j.jvolgeores.2018.04.029

Flóvenz, Ágústsson, K., & Flóvenz, Ó. (2015). *Ágústsson and The Thickness of the Seismogenic Crust in Iceland and its Implications for Geothermal Systems*.

Galindo, I., & Gudmundsson, A. (2012). Basaltic feeder dykes in rift zones: Geometry, emplacement, and effusion rates. *Natural Hazards and Earth System Sciences*, *12*(12), 3683–3700. https://doi.org/10.5194/nhess-12-3683-2012

Geirsson, H. (2003). *Continuous GPS measurements in Iceland 1999—2002*. Vedurstofa Islands.

Greenfield, T., White, R. S., Winder, T., & Ágústsdóttir, T. (2020). Seismicity of the Askja and Bárðarbunga volcanic systems of Iceland, 2009–2015. *Journal of Volcanology and Geothermal Research*, *391*, 106432. https://doi.org/10.1016/j.jvolgeores.2018.08.010

Grigoli, F., Clinton, J. F., Diehl, T., Kaestli, P., Scarabello, L., Agustsdottir, T., Kristjansdottir, S., Magnusson, R., Bean, C. J., Broccardo, M., Cesca, S., Dahm, T., Hjorleifsdottir, V., Cabrera, B. M., Milkereit, C., Nooshiri, N., Obermann, A., Racine, R., Rinaldi, A. P., … Wiemer, S. (2022). Monitoring microseismicity of the Hengill Geothermal Field in Iceland. *Scientific Data*, *9*(1), Article 1. https://doi.org/10.1038/s41597-022-01339-w

Hardarson, B. S., Fitton, J. G., Ellam, R. M., & Pringle, M. S. (1997). Rift relocation—A geochemical and geochronological investigation of a palaeo-rift in northwest Iceland. *Earth and Planetary Science Letters*, *153*(3), 181–196. https://doi.org/10.1016/S0012-821X(97)00145-3

Healy, D., Rizzo, R. E., Cornwell, D. G., Farrell, N. J. C., Watkins, H., Timms, N. E., Gomez-Rivas, E., & Smith, M. (2017). FracPaQ: A MATLAB^{TM} toolbox for the quantification of fracture patterns. *Journal of Structural Geology*, *95*, 1–16. https://doi.org/10.1016/j.jsg.2016.12.003

Hensch, M., Lund, B., Árnadóttir, T., & Brandsdóttir, B. (2016). Temporal stress changes associated with the 2008 May 29 MW 6 earthquake doublet in the western South Iceland Seismic Zone. *Geophysical Journal International*, *204*(1), 544–554. https://doi.org/10.1093/gji/ggv465

Hjartardóttir, Á. R., Dürig, T., Parks, M., Drouin, V., Eyjólfsson, V., Reynolds, H., Einarsson, P., Jensen, E. H., Óskarsson, B. V., Belart, J. M. C., Ruch, J., Gies, N. B., & Pedersen, G. B. M. (2023). Pre-existing fractures and eruptive vent openings during the 2021 Fagradalsfjall eruption, Iceland. *Bulletin of Volcanology*, *85*(10), 56. https://doi.org/10.1007/s00445-023-01670-z

Höskuldsson, Á., Hey, R., Kjartansson, E., & Guðmundsson, G. B. (2007a). The Reykjanes Ridge between 63°10′N and Iceland. *Journal of Geodynamics*, *43*(1), 73–86.

Jónsson, S., Segall, P., Pedersen, R., & Björnsson, G. (2003). Post-earthquake ground movements correlated to pore-pressure transients. *Nature*, *424*(6945), Article 6945. https://doi.org/10.1038/nature01776

Kaban, M. K., Flóvenz, Ó. G., & Pálmason, G. (2002). Nature of the crust-mantle transition zone and the thermal state of the upper mantle beneath Iceland from gravity modelling. *Geophysical Journal International*, *149*(2), 281–299. https://doi.org/10.1046/j.1365-246X.2002.01622.x

Karson, J. A., Brandsdóttir, B., Einarsson, P., Sæmundsson, K., Farrell, J. A., & Horst, A. J. (2019). Evolution of migrating transform faults in anisotropic oceanic crust: Examples

from Iceland. *Canadian Journal of Earth Sciences*, *56*(12), Article 12. https://doi.org/10.1139/cjes-2018-0260

Khodayar, M., Björnsson, S., Guðnason, E. Á., Níelsson, S., Axelsson, G., & Hickson, C. (2018). Tectonic Control of the Reykjanes Geothermal Field in the Oblique Rift of SW Iceland: From Regional to Reservoir Scales. *Open Journal of Geology*, *8*(3), Article 3. https://doi.org/10.4236/ojg.2018.83021

Kowsari, M., Halldorsson, B., Kijko, A., Bessason, B., & Jónasson, K. (2020). *COMPARISON OF SEISMICITY PARAMETERS FROM VARIOUS EARTHQUAKE CATALOGUES FOR ICELAND*.

LaFemina, P. C., Dixon, T. H., Malservisi, R., Árnadóttir, T., Sturkell, E., Sigmundsson, F., & Einarsson, P. (2005). Geodetic GPS measurements in south Iceland: Strain accumulation and partitioning in a propagating ridge system. *Journal of Geophysical Research: Solid Earth*, *110*(B11). https://doi.org/10.1029/2005JB003675

Landmaelingar Íslands Atlas. (n.d.). *Artic DEM*. https://atlas.lmi.is/mapview/?application=DEM

Luxey, P., Blondel, P., & Parson, L. M. (1997). Tectonic significance of the South Iceland Seismic Transform Zone. *Journal of Geophysical Research: Solid Earth*, *102*(B8), 17967–17980. https://doi.org/10.1029/97JB00727

Lýsigagnagátt. (n.d.). *Icelandic coastline and river shapefile*. https://gatt.lmi.is/geonetwork/srv/eng/catalog.search#/metadata/FE3E66F8-7749-409A-8795-02207CE27613

Michalczewska, K., Hreinsdottir, S., Arnadottir, T., Hjaltadottir, S., Agustsdottir, T., Gudmundsson, M. T., Geirsson, H., Sigmundsson, F., & Gudmundsson, G. (2012). *Inflation and deflation episodes in the Krisuvik volcanic system*. *2012*, V33A-2843.

Pedersen, G. B. M., Belart, J. M. C., Óskarsson, B. V., Gudmundsson, M. T., Gies, N., Högnadóttir, T., Hjartardóttir, Á. R., Pinel, V., Berthier, E., Dürig, T., Reynolds, H. I., Hamilton, C. W., Valsson, G., Einarsson, P., Ben-Yehosua, D., Gunnarsson, A., & Oddsson, B. (2022). Volume, Effusion Rate, and Lava Transport During the 2021 Fagradalsfjall Eruption: Results From Near Real-Time Photogrammetric Monitoring. *Geophysical Research Letters*, *49*(13), e2021GL097125. https://doi.org/10.1029/2021GL097125

Rut Hjartardóttir, Á., Einarsson, P., & Björgvinsdóttir, S. (2015). *Fracture systems of the Western Volcanic Zone, Iceland*. 5658.

Sæmundsson, K., Sigurgeirsson, M. Á., & Friðleifsson, G. Ó. (2020). Geology and structure of the Reykjanes volcanic system, Iceland. *Journal of Volcanology and Geothermal Research*, *391*, 106501. https://doi.org/10.1016/j.jvolgeores.2018.11.022

Sigmundsson, F. (2006). *Iceland Geodynamics: Crustal Deformation and Divergent Plate Tectonics*.

Sigmundsson, F., Einarsson, P., Hjartardóttir, Á. R., Drouin, V., Jónsdóttir, K., Árnadóttir, T., Geirsson, H., Hreinsdóttir, S., Li, S., & Ófeigsson, B. G. (2020b). Geodynamics of Iceland and the signatures of plate spreading. *Journal of Volcanology and Geothermal Research*, *391*, 106436. https://doi.org/10.1016/j.jvolgeores.2018.08.014

Sigmundsson, F., Parks, M., Hooper, A., Geirsson, H., Vogfjörd, K. S., Drouin, V., Ófeigsson, B. G., Hreinsdóttir, S., Hjaltadóttir, S., Jónsdóttir, K., Einarsson, P., Barsotti, S., Horálek, J., & Ágústsdóttir, T. (2022). Deformation and seismicity decline before the 2021 Fagradalsfjall eruption. *Nature*, *609*(7927), Article 7927. https://doi.org/10.1038/s41586-022-05083-4

Skjálfta-Lísa. (n.d.). *Earthquake online catalogue of SIL picking*. https://skjalftalisa.vedur.is/#/page/map

Steigerwald, L., Einarsson, P., & Hjartardóttir, Á. (2018). Fault kinematics at the Hengill Triple Junction, SW-Iceland, derived from surface fracture pattern. *Journal of Volcanology and Geothermal Research*, *391*. https://doi.org/10.1016/j.jvolgeores.2018.08.017

Tchalenko, J. S. (1967). *The influence of shear and consolidation on the microscopic structure of some clays*. Diploma of Imperial College, Faculty of Engineering, University of London.

Tchalenko, J. S. (1970). Similarities between Shear Zones of Different Magnitudes. *Geological Society of America Bulletin*, *1970;81*(6), 1625–1640.

Tentler, T., & Mazzoli, S. (2005). Architecture of normal faults in the rift zone of central north Iceland. *Journal of Structural Geology*, *27*(9), 1721–1739. https://doi.org/10.1016/j.jsg.2005.05.018

Thordarson, T., & Larsen, G. (2007). Volcanism in Iceland in historical time: Volcano types, eruption styles and eruptive history. *Journal of Geodynamics*, *43*(1), Article 1. https://doi.org/10.1016/j.jog.2006.09.005

Vogfjörd, K. S., & Hjaltadóttir, S. (2006). *Kortlagning sprungna í Fagradalsfjalli á Reykjanesskaga með smáskjálftum*. Vedurstofa Islands.

Voight, B., Clifton, A., Hjartarson, Á., Steingrímsson, B., Brandsdóttir, B., Rodríguez, C., McGarvie, D., Sigmundsson, F., Ívarsson, G., Friðleifsson, G. Ó., Larsen, G., Jónsdóttir, G. S., Noll, H., McDougall, I., Kaldal, I., Friðleifsson, I. B., Aronson, J. L., Karson, J. A., Grönvold, K., … Friedrich, W. (2020). A half-century of geologic and geothermic investigations in Iceland: The legacy of Kristján Sæmundsson. *Journal of Volcanology and Geothermal Research*, *391*, 106434. https://doi.org/10.1016/j.jvolgeores.2018.08.012

Weir, N. R. W., White, R. S., Brandsdóttir, B., Einarsson, P., Shimamura, H., & Shiobara, H. (2001). Crustal structure of the northern Reykjanes Ridge and Reykjanes Peninsula, southwest Iceland. *Journal of Geophysical Research: Solid Earth*, *106*(B4), 6347–6368. https://doi.org/10.1029/2000JB900358

Weismüller, C., Urai, J., Kettermann, M., Hagke, C., & Reicherter, K. (2019). Structure of massively dilatant faults in Iceland: Lessons learned from high-resolution unmanned aerial vehicle data. *Solid Earth*, *10*, 1757–1784. https://doi.org/10.5194/se-10-1757-2019

Woodcock, N. H., Daly, M. C., Watson, J. V., Reading, H. G., Watterson, J., White, S. J., Reading, H. G., Watterson, J., & White, S. H. (1986a). The role of strike-slip fault systems at plate boundaries. *Philosophical Transactions of the Royal Society of London. Series A, Mathematical and Physical Sciences*, *317*(1539), Article 1539. https://doi.org/10.1098/rsta.1986.0021